COO-4319-6

TWO-DIMENSIONAL VIRTUAL IMPACTORS

Final Report

L. J. Forney
Schools of Chemical and Civil Engineering
Georgia Institute of Technology
Atlanta, Georgia 30332

and

D. G. Ravenhall
Department of Physics
University of Illinois at Urbana-Champaign
Urbana, Illinois 61801

Prepared for
DEPARTMENT OF ENERGY
Under Contract No. EE-77-S-02-4319

University of Illinois at Urbana-Champaign
Urbana, Illinois 61801

December 1980

DISCLAIMER

ABSTRACT

Theoretical predictions using both potential flow analyses and solutions to Navier-Stokes equations are made for the operating characteristics of a two-dimensional virtual impactor. Experiments were performed with 2.5 μm DOP droplets for a wide range of prototype geometries to measure the magnitude of internal losses and to fully characterize the instrument response. The influence of geometry including the throat angle ($38^{o} \leq \beta_{o} \leq 58.2^{o}$) and normalized void width ($0.7 \leq h/w \leq 1.5$) on the particle cutoff diameter, efficiency curve steepness and properties of the internal particle loss factor are presented for fixed instrument Reynolds numbers Re = 1540 and bleed flow f = 0.1. The theory, supported by trends in the empirical data, predicts that internal particle losses reduce to zero as the normalized void width increases to $h/w = 1.4 \pm .1$ while the data show a minimum at $h/w = 1.6 \pm .1$. Increasing the void width, however, is shown to substantially reduce the steepness of the particle efficiency curves.

Visual observations of the onset of fluid separation for two-dimensional jets impinging upon a void were conducted with a scaled-up water model and correlated with theory. It was found that the limiting void width h_{lim}/w marking the onset of fluid instabilities peaked for a intermediate value of the fluid deflecting plate angle $\beta \simeq 80^{o}$ with larger values of h_{lim}/w corresponding to smaller throat angles β_{o}. The limiting void width h_{lim}/w also increased with larger bleed flows into the void. These instabilities may make it difficult to correlate experimental virtual impactor data with theory.

Forney, L. J.
Ravenhall, D. G.

TWO-DIMENSIONAL VIRTUAL IMPACTORS

Final report to Department of Energy under contract No. EE-77-S-02-4319.
December 1980

KEYWORDS: Aerosols/particle size classifier/particle impactor/air pollution.

COO-4319-6

TWO-DIMENSIONAL VIRTUAL IMPACTORS

FINAL REPORT

L. J. Forney
Schools of Chemical and Civil Engineering
Georgia Institute of Technology
Atlanta, Georgia 30332

and

D. G. Ravenhall
Department of Physics
University of Illinois
Urbana, Illinois 61801

December 1980

Prepared for

DEPARTMENT OF ENERGY
UNDER CONTRACT NO. EE-77-S-02-4319

TABLE OF CONTENTS

LIST OF FIGURES

Figure-Section II

I. EXPERIMENTS

1. SUMMARY

Experimental results are presented on the operating characteristics of a versatile two-dimensional virtual impactor. The influence of geometry including the throat angle ($38^{o} \leq \theta \leq 58.2^{o}$) and normalized void width ($0.7 \leq h/w \leq 2.0$) on the particle cutoff diameter, efficiency curve steepness and properties of the internal particle loss factor are presented. Theoretical solutions to Navier-Stokes equations are used to correlate the data for fixed instrument Reynolds number (Re = 1540) and bleed flow ($Q/Qo = 0.1$). The theory, supported by trends in the empirical data, predicts that internal particle losses reduce to zero as the normalized void width increases to $h/w = 1.4 \pm .1$ while the data show a minimum at $h/w = 1.6 \pm .1$. Increasing the void width, however, is shown to substantially reduce the steepness of the particle efficiency curves.

2. INTRODUCTION

The potential health hazard represented by micron-sized suspended particles in the ambient air has focused attention on aerosol sizing instruments. One of the simplest devices capable of size-classifying aerosols (e.g. respirable vs. nonrespirable) are inertial impactors. Traditional particle-surface interaction problems associated with inertial impactors such as particle bounce, reentrainment and collection surface overload have been largely eliminated recently by the replacement of the solid impaction surface with a slowly pumped stagnate air void. Progress has been rapid on these new designs called virtual impactors in recent years (Hounam and Sherwood, 1965; Conner, 1966; Loo, et al., 1975; Dzubay and Stevens, 1975; Forney, 1976; McFarland et al., 1978; Loo et al., 1979) and several instruments which utilize the virtual impaction concept are now available commercially.

Most of the research and development on virtual impactors has focused on axisymmetric geometries (round jets) and these designs have been incorporated into commercial instruments with excellent results. However, there are a number of operational difficulties associated with the use of axisymetric jets. Because these devices are of fixed geometry, it is necessary to use a number of test aerosols of varying particle diameter to calibrate the devices. In addition, constant air flow rates restrict the sizing capabilities of the device to a single particle cutoff diameter. Moreover, it is necessary to limit the volume flow rate through a round jet in order to prohibit jet instabilities. Nevertheless, experimental data taken with single stage axisymmetric virtual impactors demonstrate the attractive features of steep particle efficiency curves

and small internal particles losses (McFarland et al., 1978; Loo et al., 1979).

Recent attempts to theoretically predict axisymmetric virtual impactor performance have had only limited success (Marple, 1980). While it has been shown that one can adequately predict the total efficiency curves for these devices (fraction of particles projected into the void and lost on internal surfaces), attempts to predict internal particle losses have been unsuccessful. Earlier theoretical work with two-dimensional virtual impactors by Forney et al. (1978) and Ravenhall et al. (1978) has provided fundamental information on general flow field properties and sizing capabilities of virtual impactors, such as the fluid flow patterns, onset of instabilities, steepness of the efficiency curves and properties of the internal particle loss spectrum.

In the present paper, extensive experimental results with a prototype two-dimensional virtual impactor are presented and correlated with theoretical predictions. The impactor, which represents a modification of an earlier device by Forney (1976), incorporates a number of useful features. For example, it has a variable-slit width similar to that developed by Cooper and Spielman (1974) and Delany and Dolan (1975) which allows one to conveniently calibrate the instrument with a single test aerosol. The variable-slit feature would also provide a cumulative particle size distribution on a real-time basis with the integration of optical or electrical sensors attached to the primary air flow. In addition, the present geometry minimizes the number of dimensionless groups which are necessary to characterize instrument performance.

3. INSTRUMENT DESIGN

The basic design of the prototype device used in this study and shown in Fig. 1 is identical to the geometry presented earlier by Forney (1976). Modifications have been included, however, to eliminate unnecessary internal particle losses. These modifications consist of the addition of filter holders to the exhausts as indicated in Fig. 2 and the addition of an excess clean air inlet to reduce particle losses on the inside front wall of the device.

As described in the earlier work of Forney, the instrument is constructed of brass and aluminum stock and is designed to operate at fixed total volume flow rate Qo and throat angle θ. The two movable plates shown in Figs. 1 and 2 are constructed such that both intersect at a common point on the left throat wall. This feature minimizes the number of geometric ratios in the problem and allows one to preserve geometric and dynamic similarity as the slit dimensions h and w are changed with two micrometers indicated in Fig. 2.

It can be shown for the geometry of Fig. 1 that the total particle collection efficiency E of the device, defined as the percentage of particles which project into the void volume or impact with the horizontal fluid deflecting plate (movable), must be a function of five dimensionless groups or

$$E = E\ (\psi,\ s/w,\ h/w,\ Re,\ Q/Qo). \qquad (1)$$

Here, ψ is the dimensionless Stokes number: $\psi = (\rho_p Qo/18\mu L(d/w)^2$, where ρ_p is the particle density (g/cm^3), Qo is the total volume flow rate (cm^3/sec), μ the air viscosity (g/cm-sec), L the impactor dimension perpendicular to the flow (cm), and d is the particle diameter (cm). Also, besides the device dimensions w, s and h as shown in Fig. 1, Q is the bleed flow or secondary

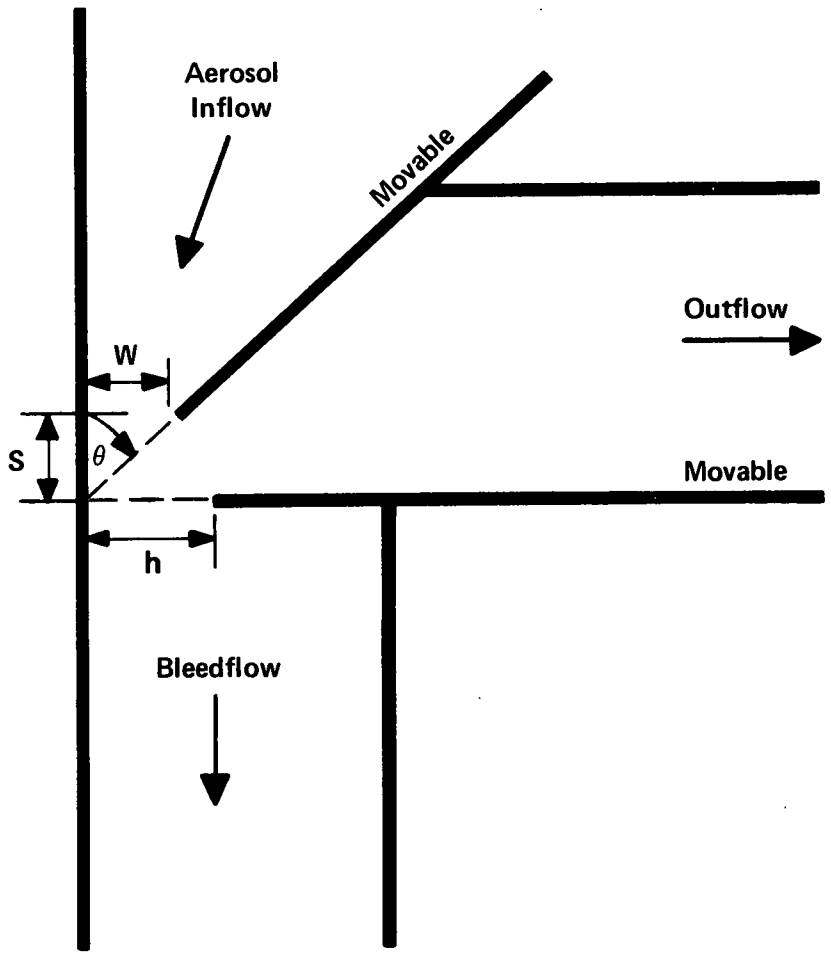

Fig. 1 Schematic of Two-Dimensional Virtual Impactor

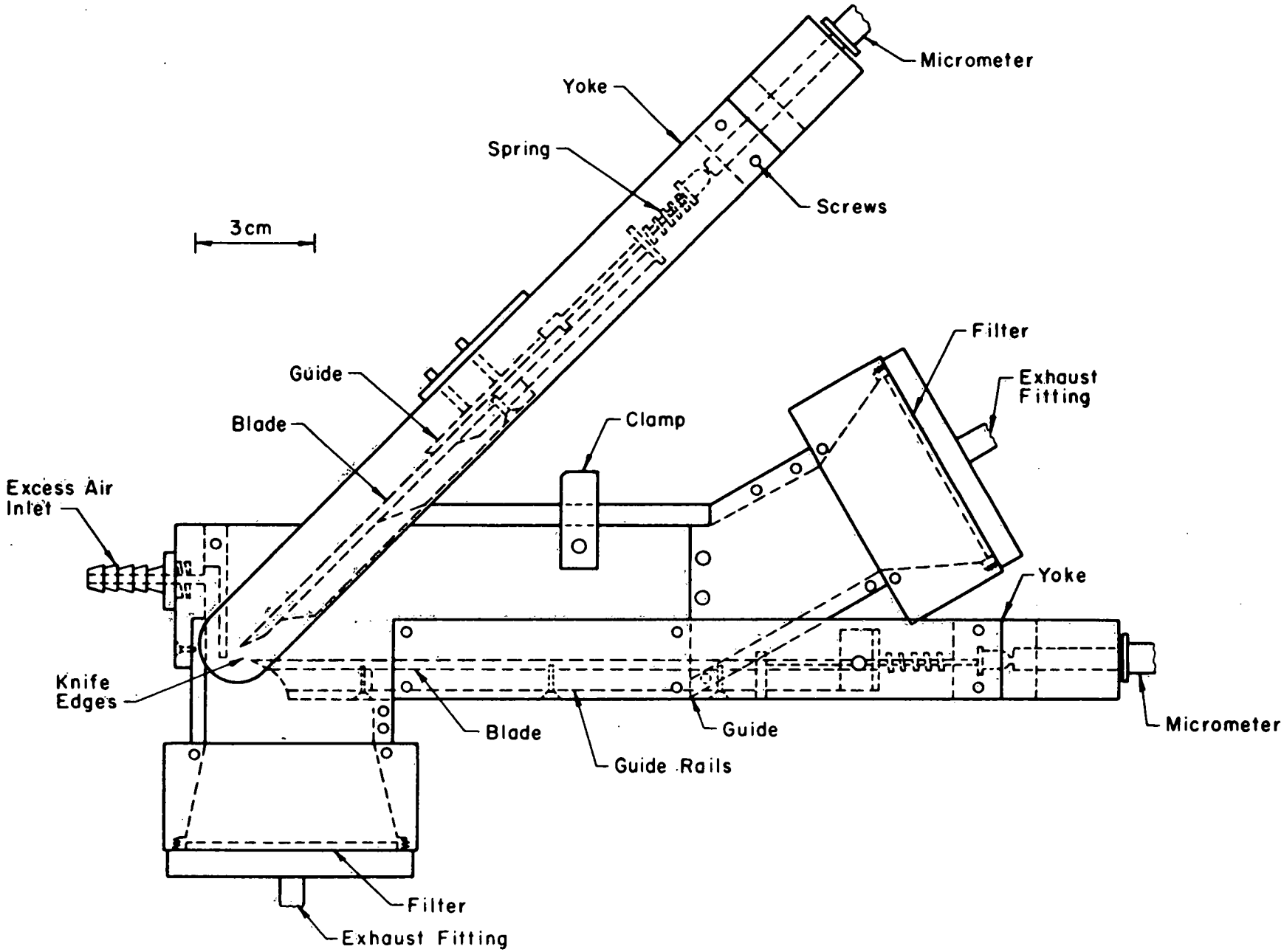

Fig. 2 Side View of Virtual Impactor

flow (cm^3/sec) and Re = $\rho Qo/L\mu$ is the Reynolds number. Moreover, since $s/w = \cot \theta$ and one can fix the geometric ratio h/w for any jet width w by proper adjustment of the micrometers, the particle efficiency reduces to $E = E(\psi)$ for constant throat angle θ and instrument flow rate Qo in which case $\psi \alpha (d/w)^2$. It is therefore possible to calibrate the instrument with a single test aerosol and to determine a cumulative size distribution of a polydispersed aerosol by proper adjustment of the slit widths w and h while preserving both dynamic similarity (constant Re) and geometric similarity (constant s/w and h/w).

4. MODEL STUDIES

A scaled-up water model of the impactor was constructed of plexiglas. Dye injection flow visualization techniques were used to determine general properties of the flow field. Results of similar studies for moderate Reynolds numbers and device geometries are extensively documented in the earlier work of Forney, et al. (1978). In the present study, however, limitations are suggested for the usable range of device Reynolds number Re, and mechanisms are discussed which can lead to a total breakdown of the fluid flow field.

Because excessive fluid flux into the void volume prohibits effective particle sizing with a virtual impactor, a systematic study was conducted on the causes of intermittent fluid loss to the void. Two problem areas were identified and their effects were observed with the water model. The first is the existence of a fluid boundary layer along the throat wall on the left of Fig. 1 while the second is the onset of fluid instabilities in the jet core at sufficient distance from the throat. To measure the effects of both problems, visual observations were made of the percentage loss of an ink tracer positioned at a distance of 0.2 w from the left wall of the impactor throat (see Fig. 1) and the results of these measurements are shown in Fig. 3.

For small jet Reynolds number in the range Re < 700 (large boundary layers) a large loss of tracer fluid to the void was observed as can be seen in Fig. 3. This is a result of the fact that fluid in the boundary layer does not have sufficient momentum to oversome the adverse pressure gradient along the wall. However, at large Re (> 1600) or large geometric ratios, jet-core instabilities developed as shown in Fig. 4 which also lead to excessive fluid flux into the void. The results of measurements which indicate both effects are shown in Fig. 3.

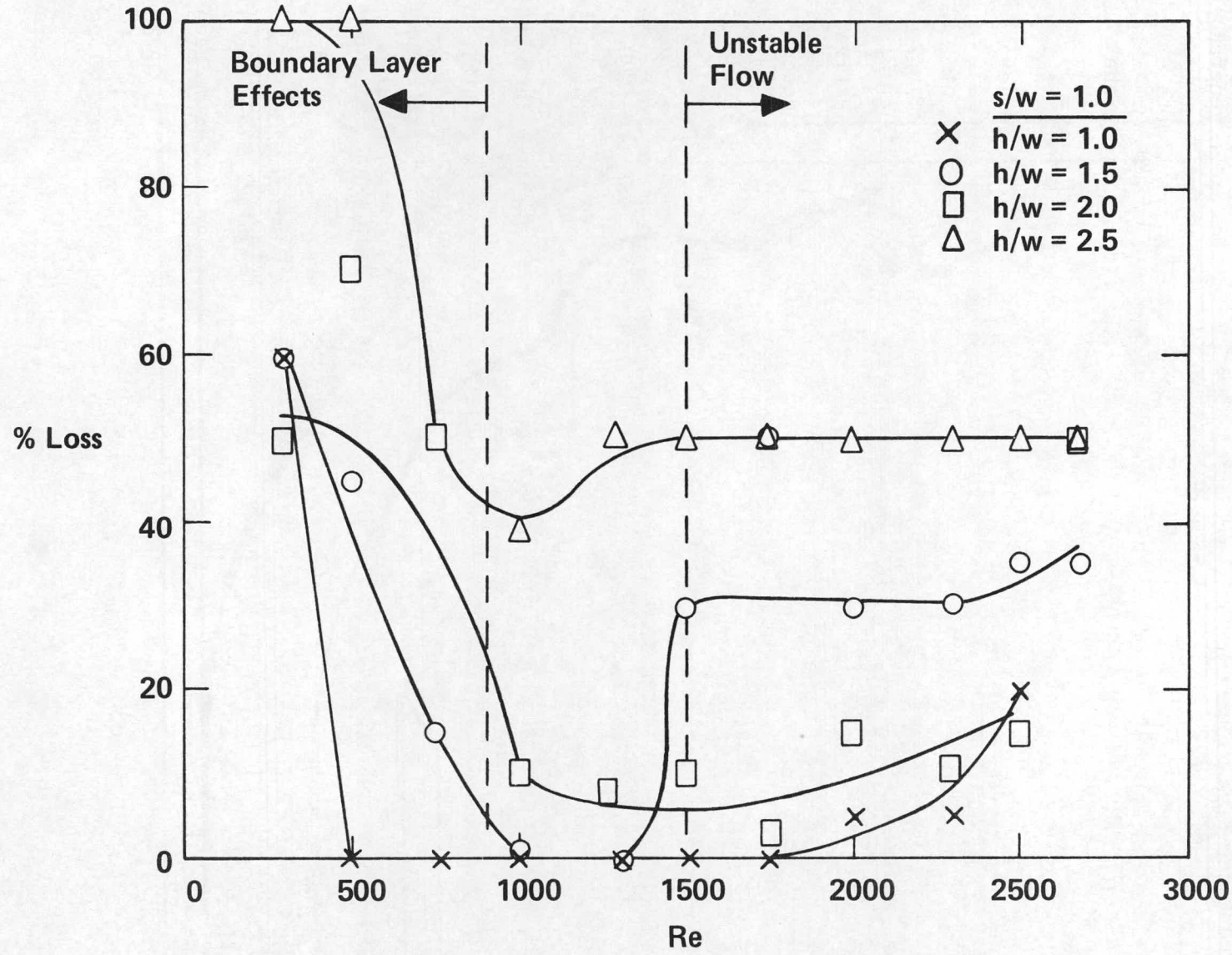

Fig. 3 Percent of Ink Tracer Lost to Void vs Jet Reynolds Number. Initial Tracer Position is w/5 from Impactor Wall

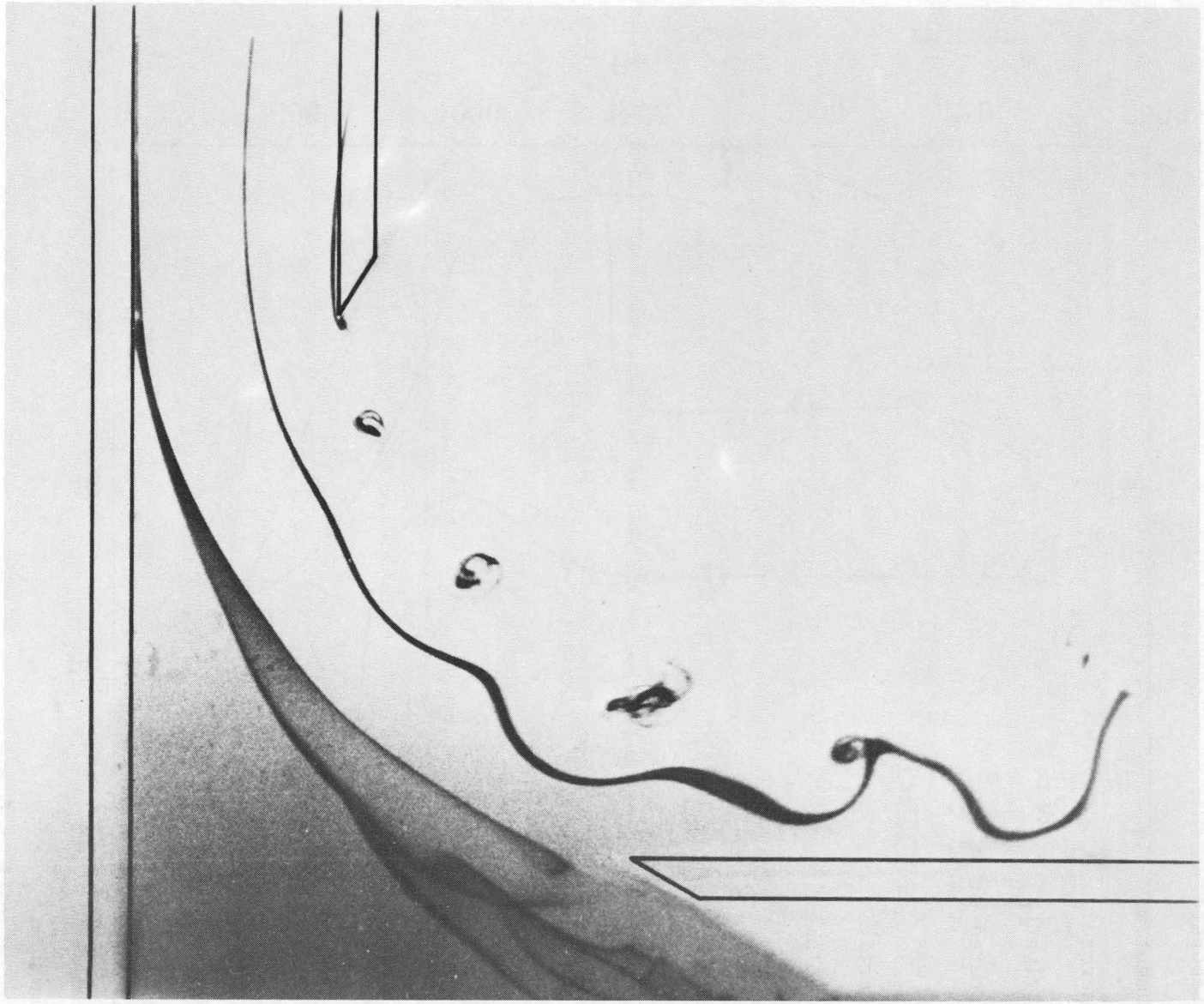

Fig. 4 Photograph of Flow Field Illustrating Jet-Core Instabilities for s/w = 3.0, h/w = 2.8 and Re = 1500

5. PROTOTYPE TESTS

Laboratory tests were conducted with the prototype device. The instrument was suspended in a 600 liter aerosol holding chamber. The test aerosol was a monodispersed 2.5 μm diameter, uranine tagged, di-octylphthalate (DOP) oil droplet. The aerosol was generated in prefiltered air using a vibrating orifice generator and the droplet charge was neutralized with a Thermo-Systems model 2054 ^{85}Kr source.

Particle efficiency and internal losses were determined at a total volume flow rate of Qo = 30 l/min (Re = 1540). The aerosol was collected on 0.8 μm pore Millipore filters at the primary and secondary (bleed flow) exhausts of the instrument as indicated in Fig. 2. The particulate was washed from the filter, analyzed fluorimetrically, and the results were compared with that collected from a third filter mounted near the device whose total volume flow rate matched that of the impactor. A typical experimental procedure was to sample the aerosol for a period of 30 min at each of several values of the particle Stokes number ψ while holding the geometric ratios s/w and h/w, the total volume flow rate Qo, and the ratio of flow rates Q/Qo constant. Thus, collection efficiency E of the prototype sampler was easily determined over a range of Stokes numbers ψ with the same test aerosol of fixed diameter by simply adjusting the slit widths w and h.

Earlier experimental work (Forney, 1976) demonstrated that the present instrument was subject to internal particle losses on the left front wall shown in Fig. 1. Section 3 describes modifications to reduce the magnitude of these losses. The effect of the addition of clean excess

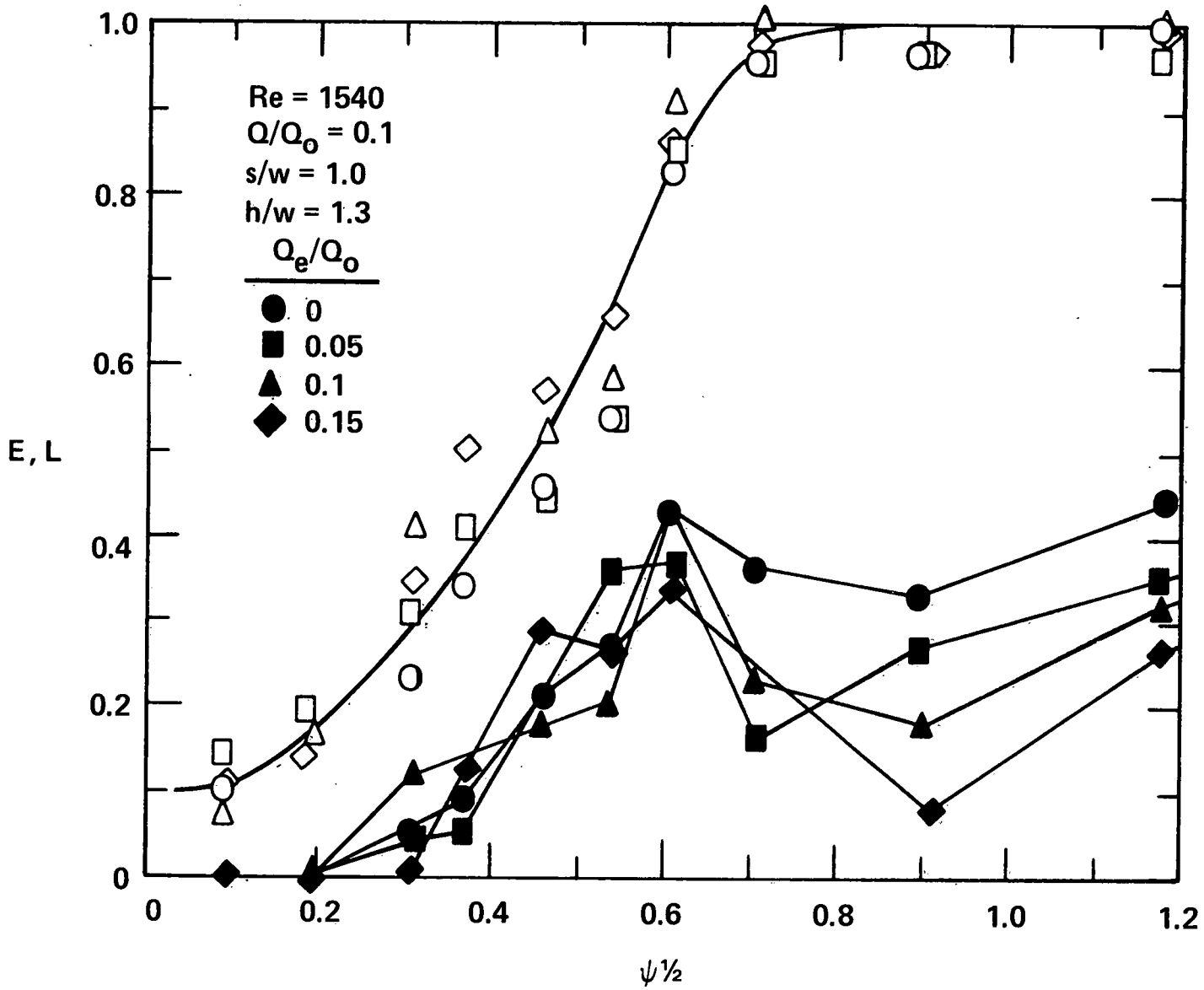

Fig. 5 Efficiency Curves for Varying Clean Excess Air Ratios, Qe/Qo

air into the void space on the magnitude of internal particle losses is demonstrated in Fig. 5. It is clear from these data that the magnitude of Qe/Qo affects internal losses only at large $\psi^{\frac{1}{2}}$ and that all internal particle losses for values of $\psi^{\frac{1}{2}}$ smaller than the minimum in the efficiency near $\psi^{\frac{1}{2}} \simeq 0.9$ of Fig. 5 are a result of particles impacting on the top of the horizontal fluid deflecting plate (shown in Figs. 1 and 2). From the data of Fig. 5 the excess blood flow was fixed at Qe/Qo = 0.15 for all subsequent experiments. Moreover, it was concluded that the complete elimination of all internal losses at large $\psi^{\frac{1}{2}}$ would require some redesign of the void space and this was outside the scope of the present work.

The effect of the magnitude of secondary flow into the void was investigated and these results are shown in Fig. 6. Clearly, increasing Q/Qo decreases internal particle losses and a value of f = 0.1 equal to that used on most commercial axisymmetric devices was chosen for all subsequent experiments.

In conclusion, all experimental data with the prototype device were taken with typical fixed values of secondary Q/Qo = 0.10, Reynolds number Re = 1540 (Q = 30 l/min) and excess air flow Qe/Qo = 0.15. One typical set of experimental data is shown in Fig. 7.

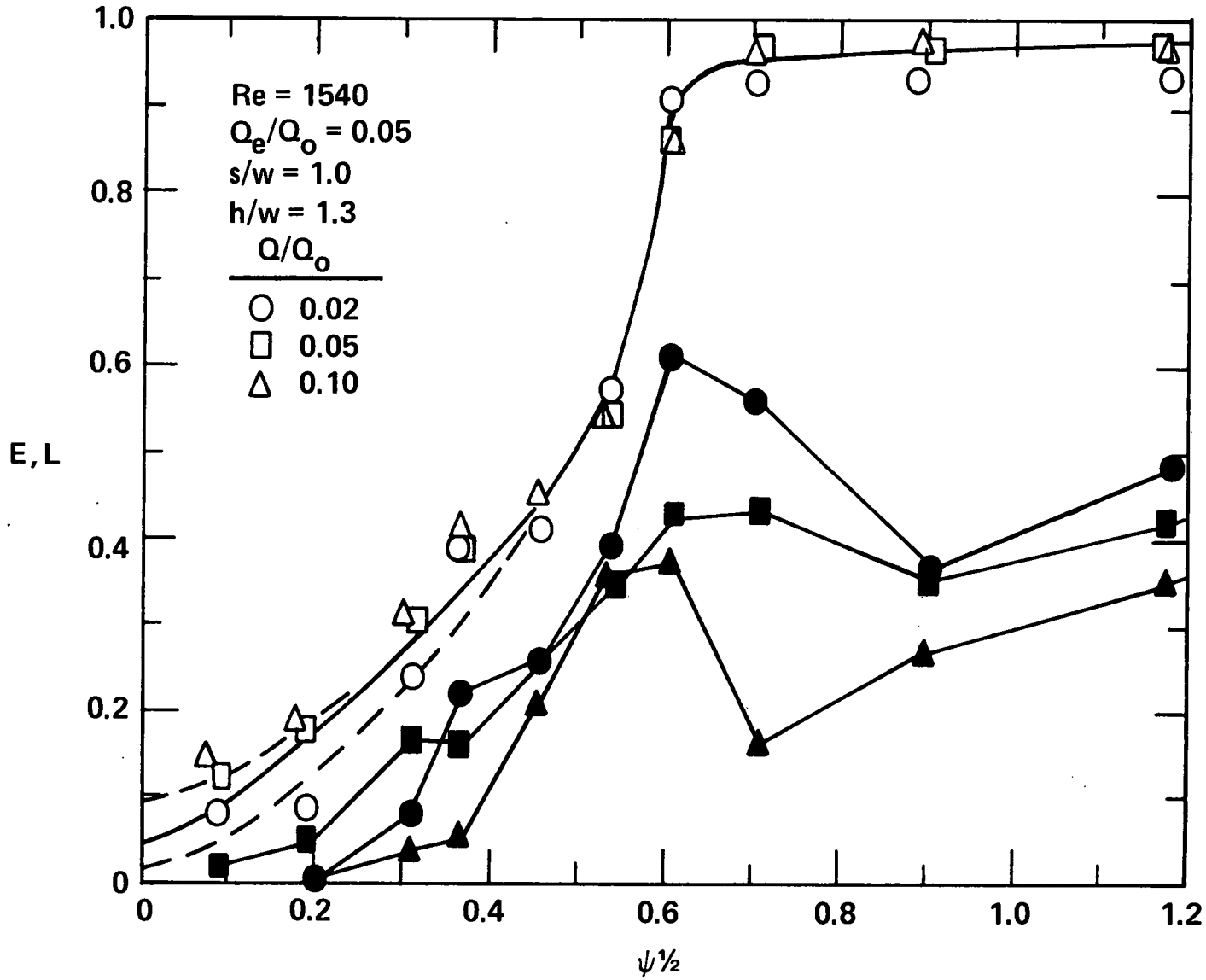

Fig. 6 Efficiency Curves for Varying Secondary Flows, Q/Qo

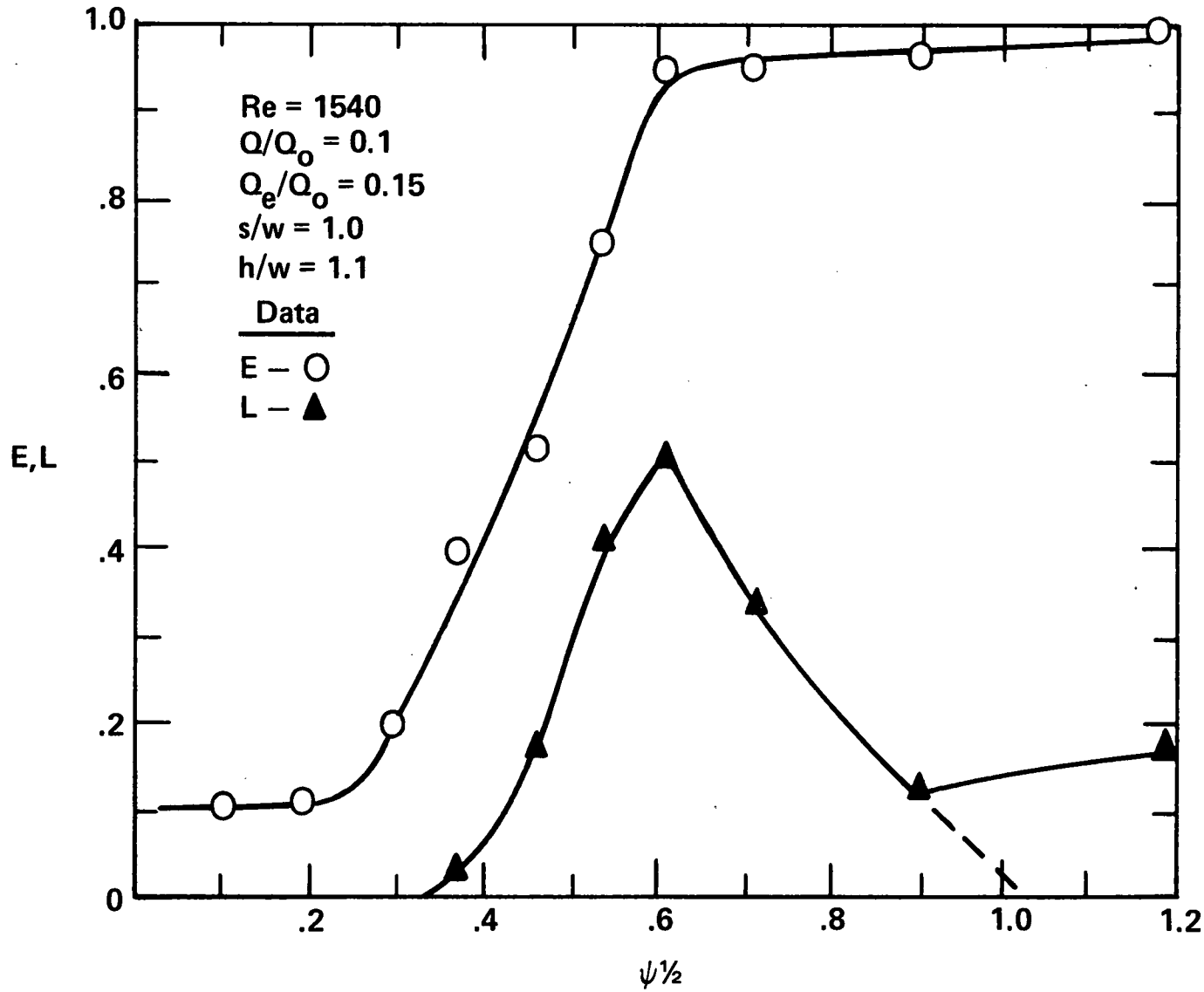

Fig. 7 Typical Experimental Data for Total Efficiency Curve and Loss Factor

6. DATA CORRELATION

In order to fully characterize the influence of geometry on impactor performance, important operating parameters are introduced similar to those defined earlier by Ravenhall et al. (1978) to correlate experimental and theoretical results. These parameters have been modified here where appropriate to account for the secondary or bleed flow into the impactor void. The first parameter is the value of $\psi^{\frac{1}{2}}$ for which the total efficiency is

$$E = \frac{1 + f}{2} \tag{1}$$

where $f = Q/Qo$ is the fraction of total air flow passing into the void. Thus for $f = .1$ we define a parameter $\psi^{\frac{1}{2}}(E = \frac{1 + f}{2}) = \psi^{\frac{1}{2}}_{55}$ proportional to the particle cutoff diameter. This characterizes the cutoff diameter for the primary flow. Also of interest is a second parameter S which we call the relative dispersion. This represents a measure of the spread of the particle efficiency curve E about the particle cutoff diameter. Formally, S is an estimate of the slope of the efficiency curve $d(\ell n\psi^{\frac{1}{2}})/dE$ evaluated at $E = .55$. Since it is desirable to maximize the normalized slope of the efficiency curve for an impactor, one seeks to minimize S. Here, we define S in the segment of the efficiency curve away from the influence of the secondary flow as

$$S = \frac{\psi^{\frac{1}{2}}(E = .84 + .16f) - \psi^{\frac{1}{2}}(E = .16 + .84f)}{(.68)(1-f)\psi^{\frac{1}{2}}(E = .5 + .5f)} \tag{2}$$

where, in this study,

$$S(f = 0.1) = \frac{\psi^{\frac{1}{2}}_{856} - \psi^{\frac{1}{2}}_{244}}{(0.612)\psi^{\frac{1}{2}}_{55}} \tag{3}$$

Additional parameters defined are the peak value and area under the loss factor L. The loss factor L represents the fraction of particles of a given $\psi^{\frac{1}{2}}$ which make contact with internal surfaces of the device and do not appear at either the primary or secondary instrument exhaust. Thus, with either experimental of theoretical data, we define a normalized area under the loss factor as

$$A = \int_{o}^{oo} L(\psi^{\frac{1}{2}}) d\ \psi^{\frac{1}{2}} \tag{4}$$

Theoretical efficiency and loss factors were determined numerically using relaxation techniques similar to those described elsewhere (Marple, 1980). The details of the computations for the present application are described by Ravenhall et al. (1980). Variation of the operating characteristics $\psi^{\frac{1}{2}}_{55}$, A, L_m, S with changes in the jet-to-plate spacing s/w, and the normalized void width h/w were determined from the experimental data. These results were compared with data derived from the numerical computations and are discussed in the next section.

7. RESULTS AND DISCUSSION

Experiments with a scaled-up water model operating within a normal range of geometries indicate that the flow field in the present two-dimensional device is subject to irregularities for both small (<700) and large (>1600) Reynolds numbers. However, the lower limit in Re would not inhibit the operation of axisymmetric devices while more research is necessary to clarify the potential problem of jet-core instabilities in round jets at large Re. Normally, it would not be necessary to operate rectangular slit impactors at large Re since greater flow rates can be achieved in devices of this type with longer slits at fixed Reynolds numbers.

Experimental and theoretical data in Fig. 8 indicate that the particle cutoff diameter $\psi_{55}^{\frac{1}{2}}$ is independent of the normalized void width h/w. Theory demonstrates a 25% increase in $\psi_{55}^{\frac{1}{2}}$ as the jet-to-plate spacing s/w increases from 0.62 to 1.28. While the latter trend was not evident from the experimental results, theory correlates empirical results to within the scatter of the data of 12%.

The dispersion S of the total particle efficiency about the particle cutoff diameter is plotted in Fig. 9. Theory accurately predicts the trend of increasing S vs. the normalized void width h/w in the data. However, the theoretical predictions are roughly 50% lower than experimental results. As in Fig. 8, differences in experimental results for the dispersion S due to changes in jet-to-plate spacing over the range $0.62 \leq s/w \leq 1.28$ were not demonstrated.

Theoretical and experimental predictions of properties of the particle loss factor L are shown in Figs. 10 and 11. Theory and experiment for both the peak in the loss factor L and the area under the loss factor A show a

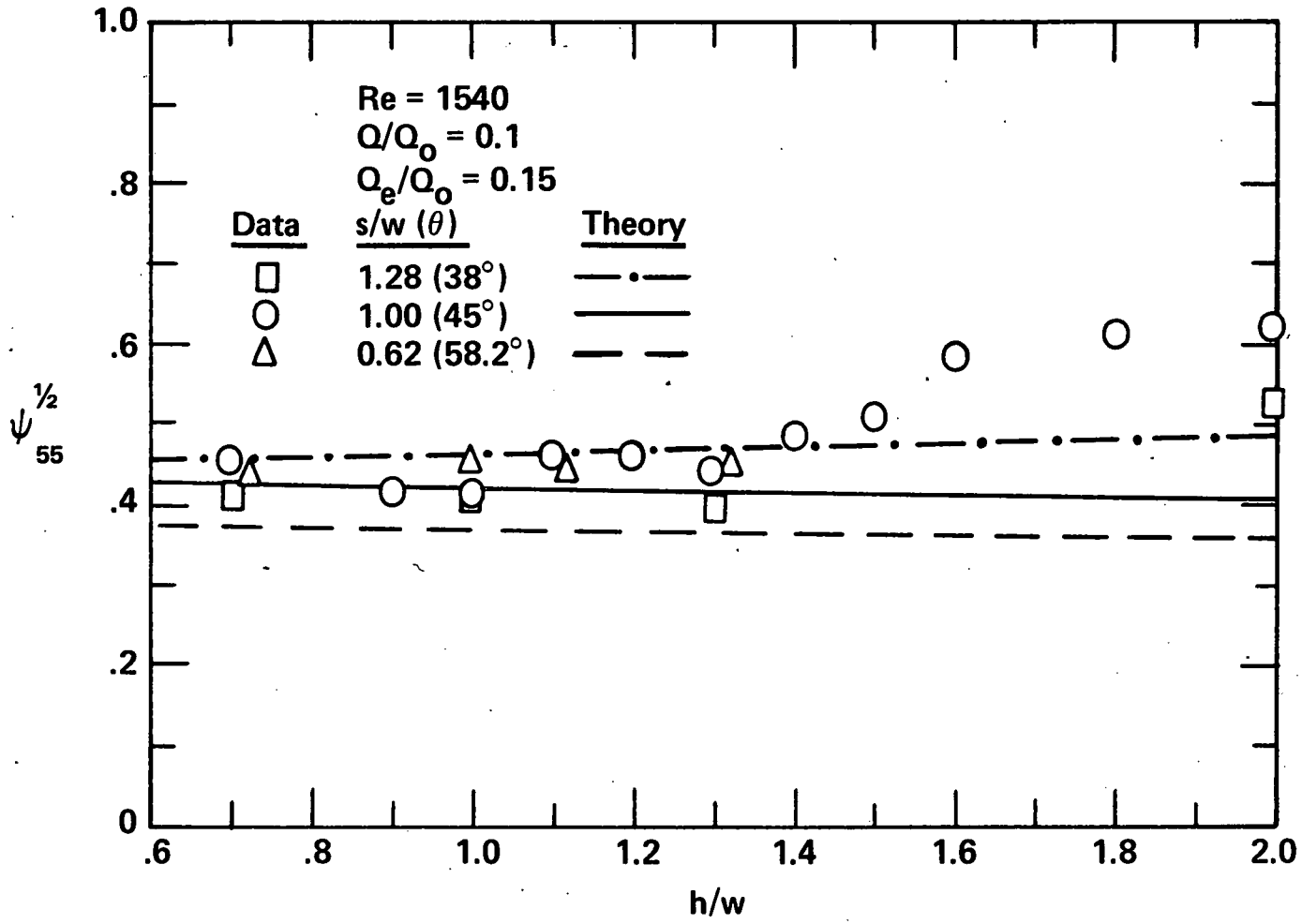

Fig. 8 Particle Cutoff Parameter vs Normalized Void Width

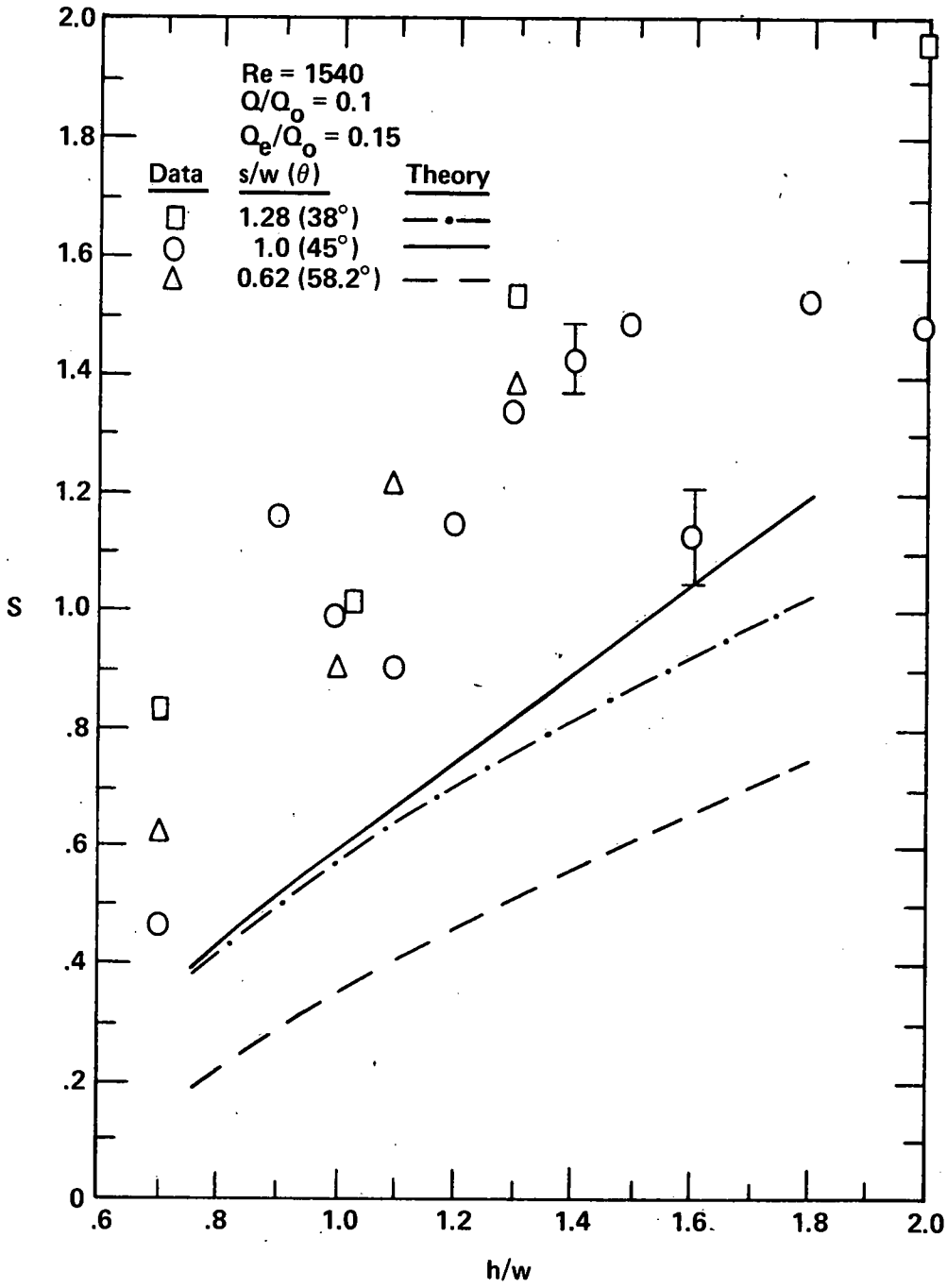

Fig. 9 Relative Dispersion vs Normalized Void Width

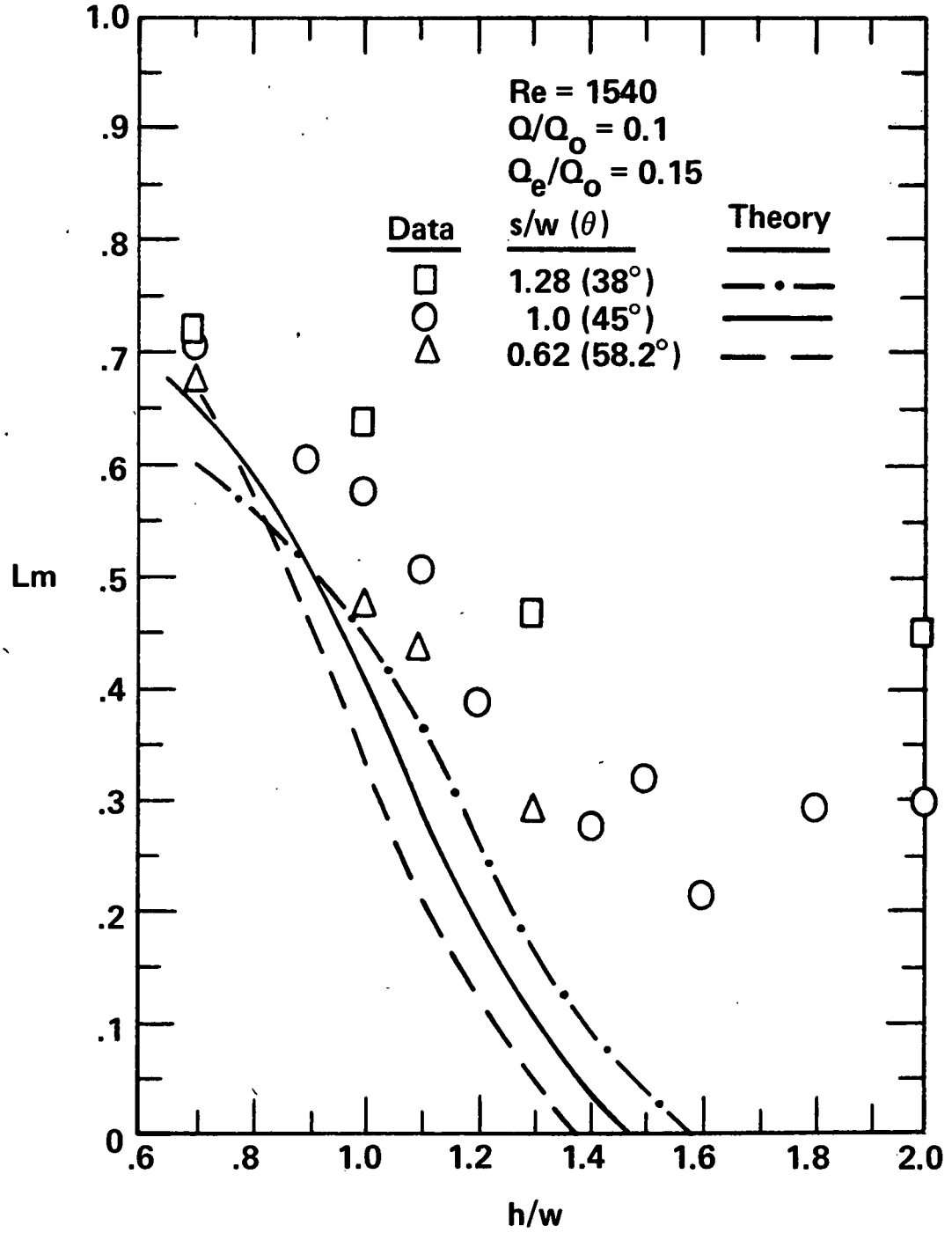

Fig. 10 Peak in Loss Factor vs Normalized Void Width

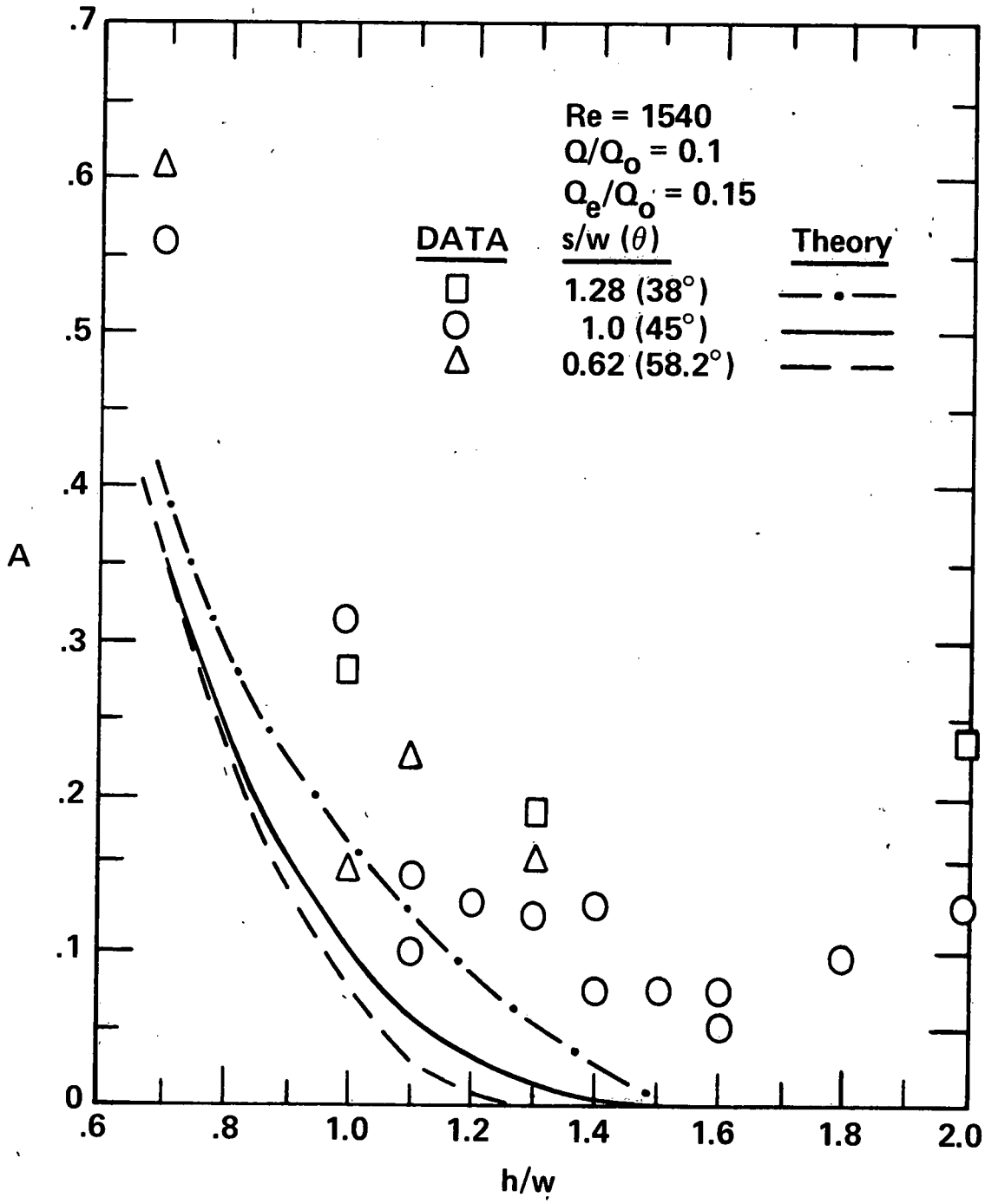

Fig. 11 Area Under Loss Factor vs Normalized Void Width

marked decrease with increasing void width h/w. Theory indicates that L_m and A should become negligible for large h/w $\gtrsim$ 1.4, while experimental data demonstrates a minimum at a similar value of h/w $\simeq$ 1.6. Theoretical predictions of L_m and A in Figs. 10 and 11 are lower than the empirical results by as much as 50%. However, theoretical trends of decreasing L_m and A with decreasing jet-to-plate spacing s/w are roughly correlated with the experimental data.

8. REFERENCES

1. Hounam, R. F., and Sherwood, R. J., Amer. Ind. Hyg. Assoc. J. 26, 122 (1965).

2. Conner, W. D., J. Air Pollut. Contr. Assoc., 16, 35 (1966).

3. Loo, B. W., Jaklevic, J. M., and Goulding, F. S., Lawrence Berkeley Laboratory Pub. LBL-3854, Berkeley, California, 1975.

4. Dzubay, T. B., and Stevens, R. K., Environ. Sci. Technol. 9, 663 (1975).

5. Forney, L. J., Rev. Sci. Instrum. 10, 1264 (1976).

6. McFarland, A. R., Ortiz, C. A., and Bertch, R. W., Jr., Environ. Sci. Technol. 12, 679 (1978).

7. Loo, B. W., Adachi, R. S. Cork, C. P., Goulding, F. S., Jaklevic, J. M., Landis, D. A., and Searles, W. L., Lawrence Berkeley Laboratory Pub. LBL-8725, Berkeley, Calif., 1979.

8. Marple, V. A. and Chien, C. M., Environ. Sci. Technol. 14, 976 (1980).

9. Forney, L. J., Ravenhall, D. G., and Winn, D. S., J. Appl. Phys. 49, 2339 (1978).

10. Ravenhall, D. G., Forney, L. J., and Jazayeri, M., J. Colloid Interface Sci. 65, 108 (1978).

11. Cooper, D. W. and Spielman, L. A., Atmos. Environ. 8, 221 (1974).

12. Delany, A. C., and Dolan, G. J., Rev. Sci. Instrum. 46, 1650 (1975).

13. Ravenhall, D. G., Forney, L. J., and Hubbard, A. J., J. Colloid and Interface Sci. (submitted 1980).

II. THEORY

1. SUMMARY

Theoretical predictions using both potential flow analyses and solutions to Navier-Stokes equations are made for the operating characteristics of a two-dimensional virtual impactor. The influence of geometry including the throat angle ($38^{\circ} \leq \beta_o \leq 58.2^{\circ}$) and normalized void width ($0.7 \leq h/w \leq 1.5$) on the particle cutoff diameter, efficiency curve steepness and properties of the internal particle loss factor are presented for fixed instrument Reynolds numbers Re = 1540 and bleed flow f = 0.1. The theory predicts that internal particle losses reduce to zero as the normalized void width increases to $h/w = 1.4 \pm .1$. Increasing the void width, however, is shown to substantially reduce the steepness of the particle efficiency curves.

Visual observations of the onset of fluid separation for two-dimensional jets impinging upon a void were conducted with a scaled-up water model and correlated with theory. It was found that the limiting void width h_{lim}/w marking the onset of fluid instabilities peaked for a intermediate value of the fluid deflecting plate angle $\beta \simeq 80^{\circ}$ with larger values of h_{lim}/w corresponding to smaller throat angles β_o. The limiting void width h_{lim}/w also increased with larger bleed flows into the void. These instabilities may impede the correlation of experimental virtual impactor data with theory.

2. INTRODUCTION

Routine methods of sampling airborne particulate matter, until recently, involved either the use of a Hi-Volume Sampler over a 24 hour period for compliance with ambient air quality standards or multistage cascade impactor in specific studies to determine the particulate mass-size distribution and chemical composition. While the Hi-Volume sampler yields the total particulate mass concentration on a filter and with further analysis the total chemical composition, it fails to distinguish between particles of different sizes, i.e. respirable versus nonrespirable. Likewise, use of the cascade impactor provides the necessary mass-size distribution but involves the following problems: particles bounce off both treated and untreated collection surfaces resulting in erroneous mass loading, multiple heavy stages yield lower particulate mass loadings per stage resulting in reduced sensitivity, and gaseous pollutants and vapors react and absorb on the surface while volatile particulate evaporate. In addition, the fixed geometry of the cascade impactor makes it difficult to calibrate.

Recently, attempts have been made to size-classify or at least to fractionate suspended particles into respirable and nonrespirable sizes with what are called virtual impactors (Dzubay and Stevens, 1975; Loo et al., 1975). The axisymmetric virtual impactors direct particle laden air at a round collection probe where particles either impact into a slowly pumped air void or escape, depending on the size of their aerodyamic diameters. These virtual impactors have replaced the solid collection surface of cascade devices with a virtual surface or air void and have eliminated the particle-surface-interaction problems.

Previous theoretical studies of two-dimensional virtual impactors using a potential flow analysis are those of Forney et al. (1978) who correlated observations with fluid flow characteristics taken from a scaled-up water model, and Ravenhall et al. (1978) who characterized the particle sizing capabilities such as efficiency curve steepness and properties of the internal loss spectrum. The geometry analyzed in both of these works was a simple, parallel throat jet impinging on a void with no bleed flow. A theoretical study of the fluid flow patterns and particle sizing characteristics of an axisymmetric jet impinging on a collection probe has been conducted by Marple (1980), who numerically solved the Navier-Stokes equations. Previous experimental work on two-dimensional virtual impactors are those of Forney (1976) and Forney et al. (1980) who provide extensive experimental data on a self-similar prototype device.

In the present study theoretical predictions are made of the fluid flow properties and the particle sizing characteristics of a two-dimensional converging throat virtual impactor. The geometry analyzed has been consrained to minimize the number of dimensionless groups needed to characterize instrument performance, as in the previous work of Forney (1976, 1980). Properties of solutions assuming ideal fluid flow, which represent an extension of the earlier work of Ravenhall et al. (1978), and new solutions that account for viscous effects are compared and discussed.

3. POTENTIAL FLOW

3.1 Ideal Fluid Transformations

The cross-section of the device is shown in Fig. 1A, together with some features of the desired flow pattern. Compared with our previous analyses, two new characteristics complicate the problem: the converging throat, and the bleed flow. While the basic methods used are the same as in our previous work, all aspects are modified considerably. It is necessary, therefore, to document the transformations and analysis.

The physical device, represented in the z-plane, consists of an axial wall GO, and a wall AB inclined at an angle β_o to it, to form a converging entrance jet. The width of the throat is w. The plate ED which guides the emerging jet at an angle β to the axial wall, and which has a perpendicular opening h, is to be placed so that its continuation intersects the axis at O, coincident with the continuation of AB. This self-similar geometry, a constructionally simplifying property, imposes a constraint which the subsequent transformations must allow for.

A fraction f of the incident flow Q is to be bled off into the void space. For simplicity it is assumed that the free streamline bounding the flow, which leaves the axial wall at the bifurcation point F, continues into the void, ultimately, at K, parallel to the plate EF. The plate is assumed to be infinitesimally thin at E, so that the streamline which arrives there divides into two parts, going to J in the bleed flow and to D in the emerging jet. The free streamline BC bounds the other side of this jet. At the point H on the axial wall the fluid velocity, zero at G and constant in magnitude from F to K, achieves its maximum value. It is evident that for the device properties to be consistent with ideal fluid flow, H must lie upstream of F, and be distinct from F. It is this requirement which will limit the value of the opening, h, of the plate. The two idealizations in the foregoing description, that the

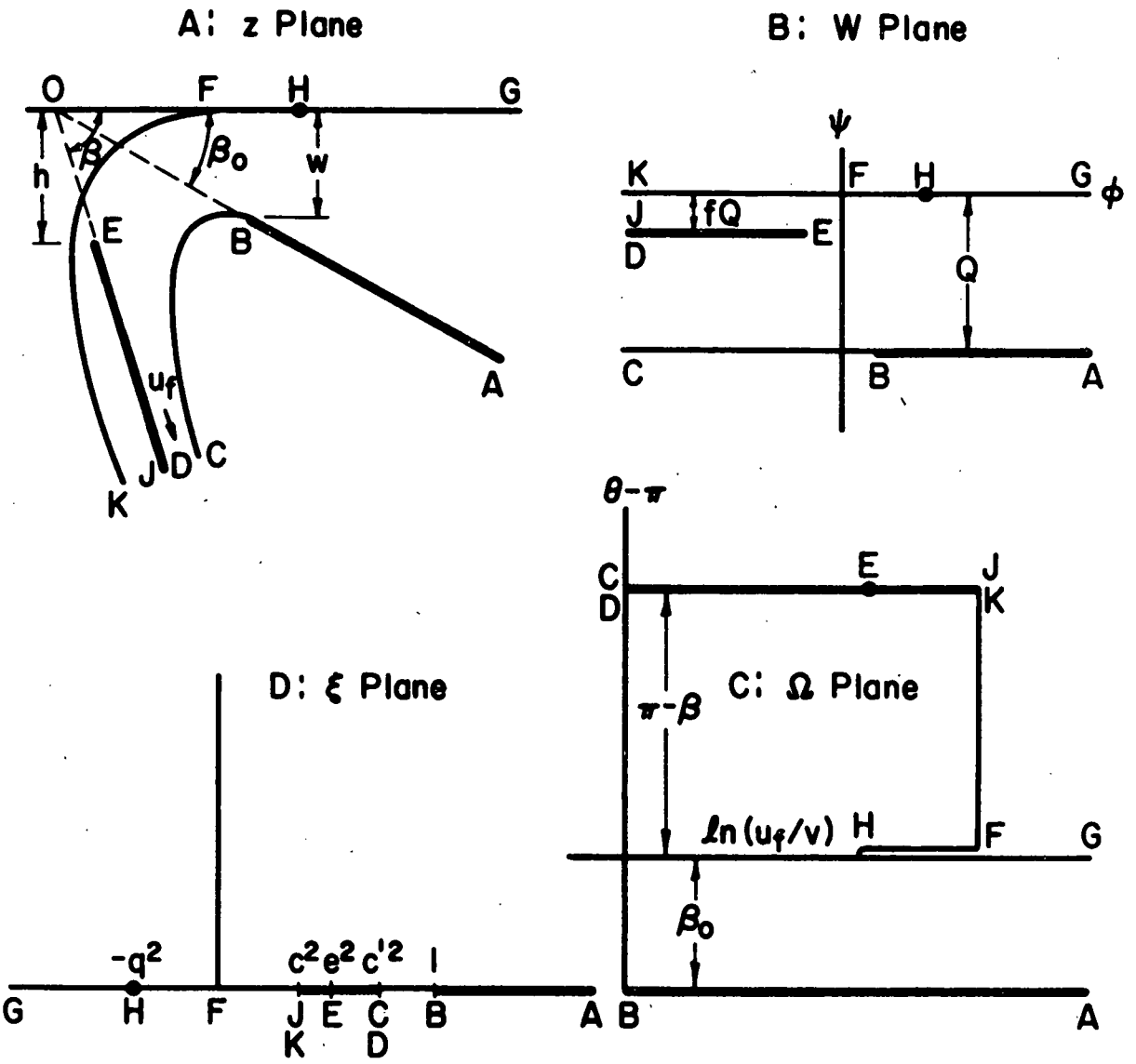

Fig. 1 Transformation Planes

bleed flow is ultimately parallel to the plate and that the plate has infinitesimal thickness at E, are not essential, and could be avoided. However, because of the small rate of bleed flow and of boundary layer effects not included here, they are not expected to affect significantly the results to be obtained.

The transformation planes which permit us to achieve the device are also shown in Fig. 1. The complex potential W of the flow (where $dW/dx = v^*$, the complex conjugate of v the fluid velocity) is confined to the infinite horizontal strip ACKG, of width equal to Q, the flow rate. The deflecting plate is horizontal in this plane, and displaced down a distance fQ corresponding to the fraction f of bleed flow into the void space. The origin is chosen to be the point F.

The straight boundaries and free streamlines of the device are all represented as straight boundaries in the plane of the Kirchhoff variable $\Omega = \log(u_f dz/dW)$, u_f being the velocity of the emerging jet. The points G and A, the outer ends of the converging jet where the fluid velocity is vanishingly small, go to infinity in this plane. The horizontal lines CD-JK and BA have vertical positions determined from the angles β and β_o. The positions of the vertical line JK-F and the point H, related to the velocity of the free streamline FK and the maximum axial fluid velocity, are not prescribable, however, but must be determined by the mutual consistency of the mapping procedure.

To connect the variables W and Ω, they are both mapped onto the upper half-plane of a subsidiary variable ξ. The point F is taken as the origin in ξ, and B the point $\xi = 1$. The other characteristic points of the W and Ω planes, CD, E, JK, and H, then occur at the ξ values c'^2, e^2, c^2 and $-q^2$ respectively. These four quantities are parameters whose values must be chosen so as to reproduce if possible the desired dimensions of the z-plane device. (The variable ξ corresponds to the square of the variable ζ introduced in earlier work, and it is for consistency of present formulae with that work that the four

quantities are introduced as the squares of real quantities.) It is evident from the ξ-plane topology that $-q^2<0<c^2<e^2<c'^2<1$.

The Schwartz-Christophel transformation which maps the horizontal strip of the W-plane onto the upper half-plane of ξ leads to the differential relationship

$$\frac{dW}{d\xi} \propto (\xi-c'^2)^{-1}(\xi-e^2)(\xi-c^2)^{-1}. \tag{1}$$

Integration of this equation, with constants determined by the position of F and the width Q of the strip, yields

$$W = \frac{Q}{\pi}\left[\frac{c'^2-e^2}{c'^2-c^2}\log\frac{c'^2-\xi}{c'^2} + \frac{e^2-c^2}{c'^2-c^2}\log\frac{c^2-\xi}{c^2}\right] . \tag{2}$$

The condition that the fraction of the bleed flow is f then determines the parameter e^2, in the form

$$e^2 = fc'^2 + (1-f)\ c^2 \quad . \tag{3}$$

Thus W is simply related to ξ by

$$\frac{\pi W}{Q} = f\log\frac{c'^2-\xi}{c'^2} + (1-f)\log\frac{c^2-\xi}{c^2} \quad . \tag{4}$$

In ξ, the flow pattern is that of two sinks at JK and CD, of relative strengths f and 1-f, with E as the stagnation point between them. For any useful value of f not equal to zero, the relationship between W and ξ may be inverted only numerically.

The interior of the "dipper" shaped object of the Ω plane and the upper half of the ξ plane are linked by the Schwartz-Christophel relationship

$$\frac{d\Omega}{d\xi} \propto (\xi-1)^{-\frac{1}{2}}(\xi-c'^2)^{-\frac{1}{2}}(\xi-c^2)^{-\frac{1}{2}}\xi^{-\frac{1}{2}}(\xi+q^2) \quad . \tag{5}$$

Its integral, in the form

$$\Omega = C\left\{(q^2+c'^2)F(\phi\backslash\alpha) + (1-c'^2)\Pi(1/c'^2;\phi\backslash\alpha)\right\} + D, \tag{6}$$

involves elliptic integrals of the first kind, $F(\phi\backslash\alpha)$, and of the third kind, $\Pi(n;\phi\backslash\alpha)$ as well as constants C and D to be related to the dimensions in the Ω plane. The argument ϕ of the elliptic integrals is

$$\phi = \tan^{-1}\left[\frac{\xi-1}{\xi}\,\frac{c'^2}{1-c'^2}\right]^{\frac{1}{2}} , \tag{7}$$

and the modular angle α is

$$\alpha = \cos^{-1}\left[\frac{1-c'^2}{c'^2}\,\frac{c^2}{1-c^2}\right]^{\frac{1}{2}} . \tag{8}$$

In the complex plane of ϕ the region of interest covers the vertical half-strip $0 \leq \mathrm{Re}\,\phi \leq \pi/2$, $\mathrm{Im}\,\phi \geq 0$. Both functions F and Π have a branch point at $\phi_c = \pi/2 + i \log \cot\alpha/2$, while Π has also a pole at $\phi_p = \sin^{-1}c'$. Fixing the constants C and D of the Ω expression requires the values of F and π at the various extremities of the ϕ region, which for F involve $K(\alpha)$, $K'(\alpha)$ the complete elliptic integrals of the first kind. For the function Π the corresponding values are denoted as follows:

$$\phi \to i\infty,\ \Pi \to i\Pi_a(1/c'\backslash\alpha) ; \tag{9a}$$

$$\phi \to \pi/2 + i \log \cot \alpha/2,\ \Pi \to \Pi_b(1/c'\backslash\alpha) + i\Pi_c(1/c'\backslash\alpha) . \tag{9b}$$

In terms of these quantities and of the known dimensions in the Ω plane, the constants C and D may be determined to be

$$C = \beta_o/\left[(1-c'^2)\Pi_c\right] , \tag{10a}$$

$$D = -i\,\beta_o . \tag{10b}$$

The ξ-plane parameter q^2 is also fixed by the consistency of the mapping to be

$$q^2 = (1-c'^2)\left[(\pi-\beta+\beta_o)\Pi_c/\beta_o - \Pi_a\right]/K'(\alpha) - c'^2 . \tag{11}$$

Thus there now remain only two undetermined ξ-plane parameters, c^2 and c'^2. The

constraints that implicitly determine them are the z-plane parameter ratio h/w and the requirement of self-similarity.

The design combination of bleed flow with a parallel incident jet is also accessible at this stage. It involves the $W(\xi)$ relationship deduced here, with the $\Omega(\xi)$ relationship obtained in our earlier work. In the present notation, that relationship takes the form

$$\Omega = \log(u_f w/Q) \{F(\phi\backslash\alpha)/F(\sin^{-1}c'\backslash\alpha) - 1\} . \qquad (12)$$

It is the limiting case, as $\beta_o \to 0$, of the more general expression used in the present work.

Another limiting case may also be noted, that of a solid plate (h=0) with a converging incident jet. This requires f=0 (no bleed flow) in the $W(\xi)$ expression, and an Ω mapping in which the vertical side JK-F goes to $\Omega = +\infty$. The parameter c^2 of the ξ plane is no longer needed, and the Schwartz-Christophel transformation may be integrated in terms of elementary functions, to yield

$$\Omega = (\beta_o/\pi) \log\left[\xi' + (\xi'^2 - s^2)^{\frac{1}{2}}\right] - i\,\beta_o - (1-\beta/\pi) \log \frac{\left[\xi' + (\xi'^2 - s^2)^{\frac{1}{2}} + \frac{1}{2}(1+c')^2\right]}{\left[\xi' + (\xi'^2 - s^2)^{\frac{1}{2}} + \frac{1}{2}(1-c')^2\right]} \qquad (13)$$

where $\xi' = \xi - \frac{1}{2}(1+c'^2)$ and $s = \frac{1}{2}(1-c'^2)$. The other ξ-plane parameter q^2 has the value

$$q^2 = c'(\pi-\beta)/\beta_o . \qquad (14)$$

The relationship of the $W(\xi)$ and $\Omega(\xi)$ transformations to the z-plane, and thus the determination of the device dimensions produced by assumed values of c^2 and c'^2, is achieved by numerical integration. In principle the integrals may be defined by a contour of any prescribable shape in either of the planes W or ξ. The definition of Ω, which on inversion gives

$$\frac{dz}{dW} = \frac{1}{u_f} e^{\Omega} \tag{15}$$

leads to the two possible integrals for the distance between two points P_1 and P_2 in the z-plane:

$$z(P_2) - z(P_1) = \frac{1}{u_f} \int_{W(P_1)}^{W(P_2)} e^{\Omega(\xi[W])} dW \tag{16a}$$

$$= \frac{1}{u_f} \int_{\xi(P_1)}^{\xi(P_2)} e^{\Omega(\xi)} \frac{dW}{d\xi} d\xi \ . \tag{16b}$$

Inversion of the $W(\xi)$ relationship is required in the first of these expressions, which suggests that the second form may be more convenient. The converging nature of the flow in the ξ plane, however, means that roughly equal distances in z correspond to quite different distances in ξ, depending on how close to the sinks at c^2 and c'^2 the points P_1 and P_2 happen to be. A numerical integral with equal intervals can thus be very wasteful of computer time. The rather intricate numerical problem of the inversion of $W(\xi)$, to be done using Newton's method of linear extrapolation in the complex ξ plane, was finally achieved by the use of four separate starting approximations, for the four regions of incident jet, outgoing jet, bleed jet and the region around the plate edge E. With this inversion available for all W and ξ, it then proves much more straightforward to do the integrals in the W plane. For most of the integrals involved, the contour is a straight line joining $W(P_1)$ and $W(P_2)$. Integrals starting at the points B, E or F have a square-root end-point singularity, however, which for a small part of the integral near the point is allowed for by a suitable change of variable.

To obtain the physical dimensions of the device for assumed values of c and c', the distances are calculated from B to E, and from B to a point P a little upstream of H, to give

$$\mathrm{Im}[z(P)-z(B)] = w, \tag{17a}$$

$$z(B) - z(E) = h-w + id. \tag{17b}$$

The first of these results determines w, and thus the physical scale of the device. (The quantity Q/u_f introduces the dimension of length into the problem, but w itself is not prescribable.) By trigonometry, the intersections of the incident jet wall AB and of the plate DE with the axial wall GO may then be calculated. These two intersections will not in general be coincident. For a given value of c, a search is made on c' by Newton's method to find the value at which the continuations of the walls intersect at one point, at which stage self-similarity of the device has been achieved. The device at this stage has known dimensions w and h. The value of h/w may now be explored as a function of the angles β_o and β.

For self-similar geometries (i.e. a determined value of c' for a given c) a search may now be made on c to obtain a prescribed value of h/w. As with an earlier study with a parallel incident jet, it is found that h/w may not take on all possible values. There is a superior limit h_{lim}/w which occurs (at varying values of c) when q^2 becomes equal to zero. In the z plane, the point H, where the axial velocity reaches its maximum value, touches F, the end of the free streamline on which the velocity is constant in magnitude. In the Ω plane the indentation HF disappears. It is evident in either plane that further motion of H is prohibited. For several values of the throat angle β_o, the value of h_{lim}/w as a function of the plate angle β is shown in Fig. 5. A typical set of fluid streamlines for a determinate geometry (i.e., $h/w \leq h_{lim}/w$) is shown in Fig. 2.

The limitation on h/w is a property of the mapping we have chosen (Fig. 1) rather than an absolute limitation on the applicability of potential flow. The appropriate mapping for $h > h_{lim}$ corresponds to detachment of the emerging jet from the fluid deflecting plate. A free streamline starts at the plate edge, and forms the lower boundary of the emerging jet. The transformations corresponding to these mappings are straightforward, but are not given here.

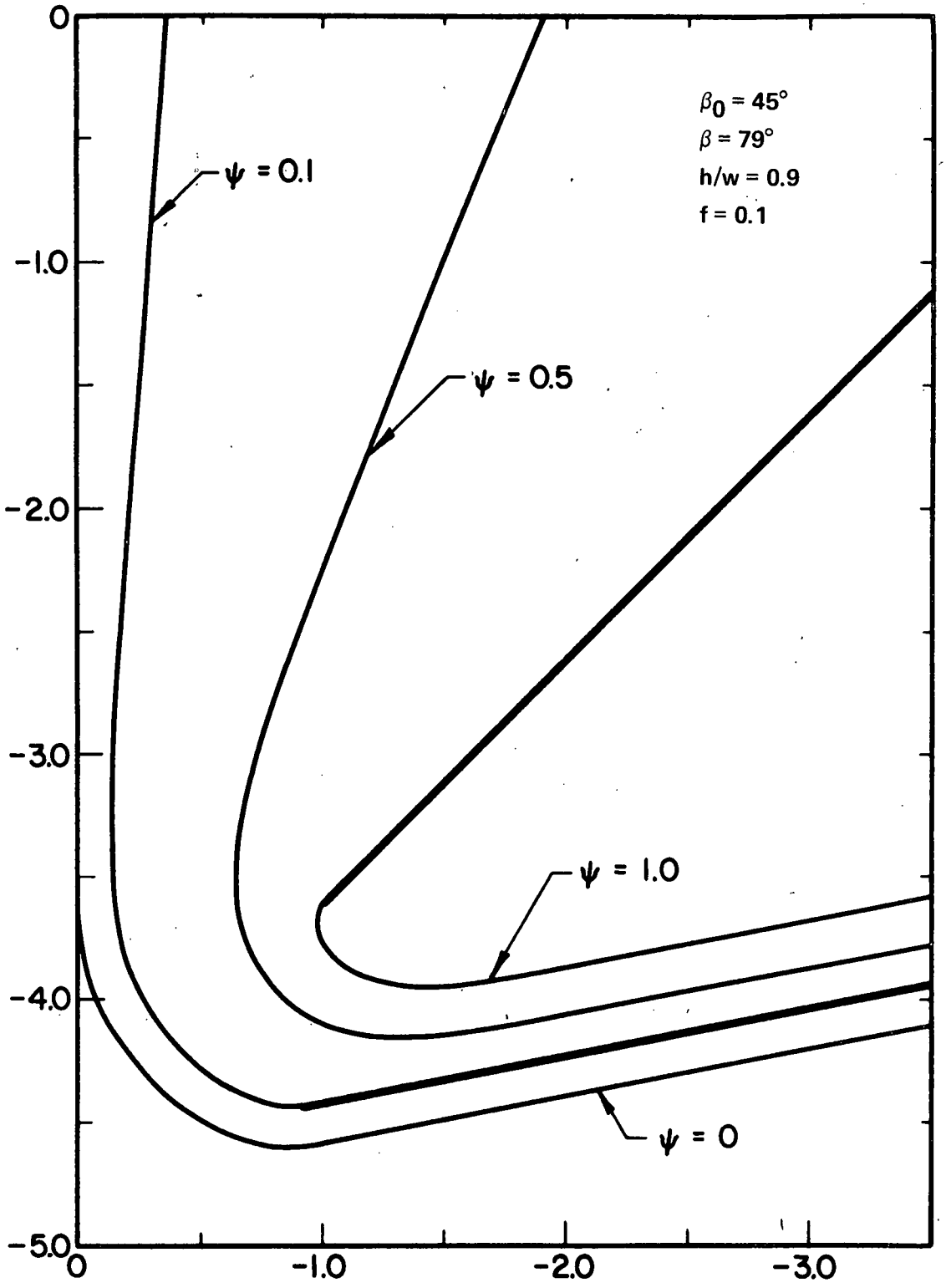

Fig. 2 Fluid Streamlines (potential flow)

3.2 Particle Trajectories

The quite standard methods used in earlier work to calculate the trajectories of injected particles were made sufficiently flexible that they work in these generalized flow patterns with no substantial changes. The equation of motion of a particle of mass m, moving with velocity $\vec{v}$ in fluid of velocity $\vec{v}_f$, is according to Stokes' Law

$$m \frac{d\vec{v}}{dt} = K(\vec{v}_f - \vec{v}) \quad . \tag{18}$$

The unit used for fluid velocities (in the definition of Ω, for example), and for $\vec{v}$ is u_f, the velocity of the outgoing jet. The unit for the device size and for the particle position $\vec{x}$ (where $\vec{v} = d\vec{x}/dt$) is w the throat opening. The dimensionless equations to be solved are thus

$$d(\vec{x}/w)/d\tau = \vec{v}/u_f \quad , \tag{19a}$$

$$d(\vec{v}/u_f)/d\tau = (\vec{v}_f/u_f - \vec{v}/u_f)/\mu \quad . \tag{19b}$$

where $\tau = u_f t/w$, and $\mu = mu_f/Kw$. With the simple assumption that $m = \frac{4}{3}\pi a^3 \rho$, where a is the particle radius and ρ its density, and that $K = 6\pi\eta a$ where η is the fluid viscosity, then $\mu = \frac{2}{9} \rho u_f a^2/w\eta$.

The convenient dimensionless quantity to quote in practice should involve not u_f but $\bar{u}_o = Q/w$, the average fluid velocity at the throat. The ratio $u_f/\bar{u}_o = R$ is obtained during the calculation of the flow pattern. The customary dimensionless variable ψ is thus given by $\psi = \mu/R$ and it is the quantity

$$\psi^{\frac{1}{2}} = a(\frac{2}{9} \rho \bar{u}_o/w\eta)^{\frac{1}{2}} , \tag{20}$$

directly proportional to the particle radius, that is used to characterize the particle-sizing properties of the device.

For a given device configuration a file of information is calculated which contains positions in the z plane and fluid velocities on a grid of points,

rectangular in the W plane, that adequately cover the device. By third-order two-dimensional interpolation from the four closest points, the fluid velocity at any position $\vec{x}$, $\vec{v}_f(\vec{x})$, may be obtained. Particles are inserted into the incident jet, at some reasonable distance from the throat, with initial velocities equal to the local fluid velocity. The initial position is in fact specified in the W plane, as $W_s = (x_w - iy_w)Q$. The starting coordinates $\vec{x}_s$ calculated by Eq.(16a) from W_s, for y_w ranging from zero to one, lie approximately on a circle centered at 0, the wall intersection point. As a function of the Stokes parameter $\psi^{1/2}$ and of the starting position as specified by y_w, the rest of the problem is the same as it was for a straight jet. A trajectory is followed until (A) it enters the void space or the bleed flow, or (B) it collides with the plate or will asymptotically do so, or (C) it escapes with the emerging jet. Functions $y_w(\psi^{1/2})$ corresponding to the A:BC separation (from those particles which hit the edge E) and to the AB:C separation are shown in Fig. 3. It is evident from the procedure described that these are, or provide the material for (in the case that $y_w(\psi^{1/2})$ is double-valued) the separation efficiencies desired.

3.3 Scaled-up Water Model

Features of the impactor flow field were observed and recorded with a scaled-up Plexiglas water model as illustrated in Fig. 4. The model was immersed and anchored in a 25 gal water tank with the outlet connected directly to a centrifugal pump. Dye was injected into the throat of the model from tygon tubing connecting three stainless steel injector nozzles to a cylindrical reservoir suspended above the tank. Tubing clamps regulated the flow of washable water diluted, black India ink into the

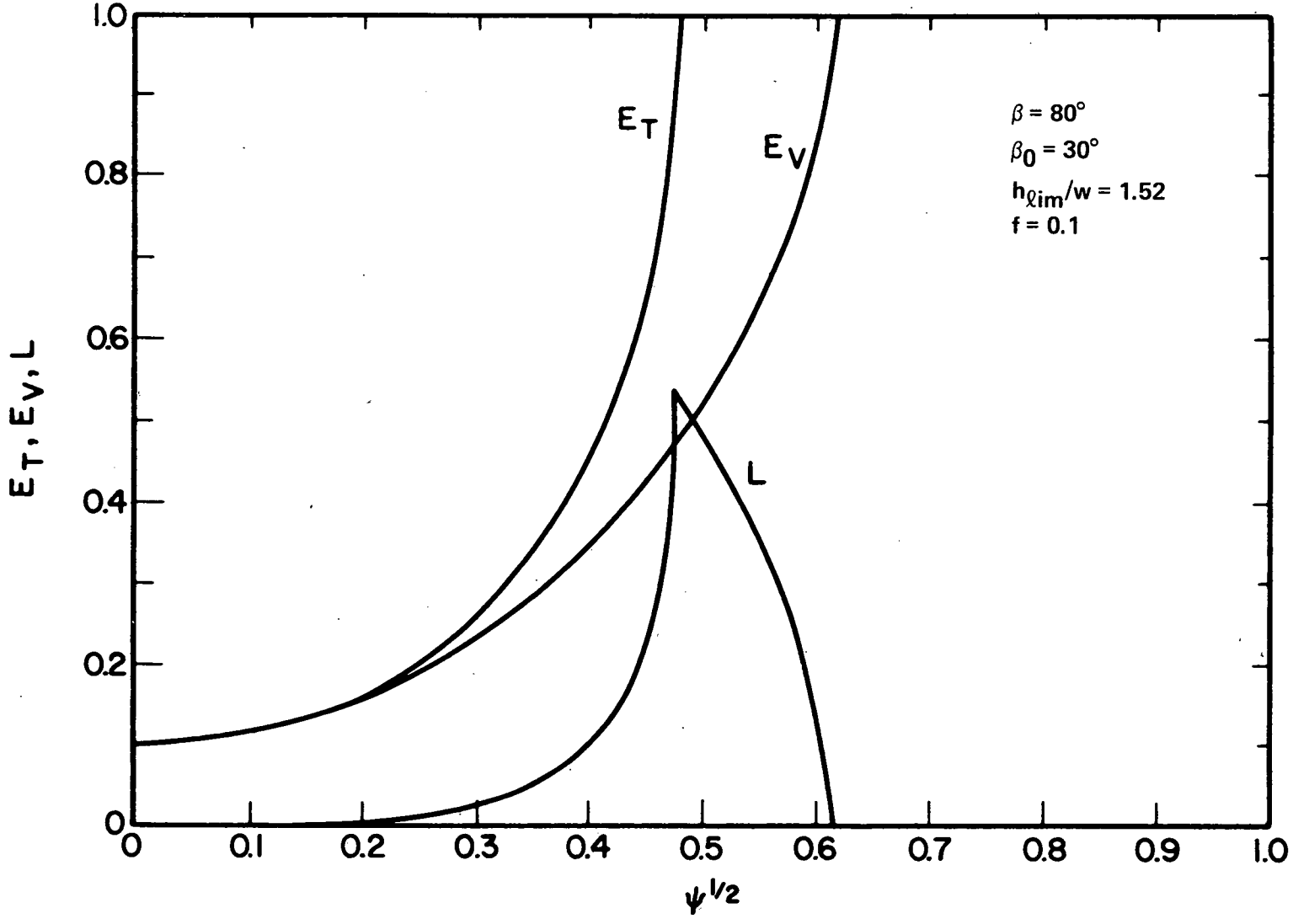

Fig. 3 Particle Efficiency Curves (potential flow)

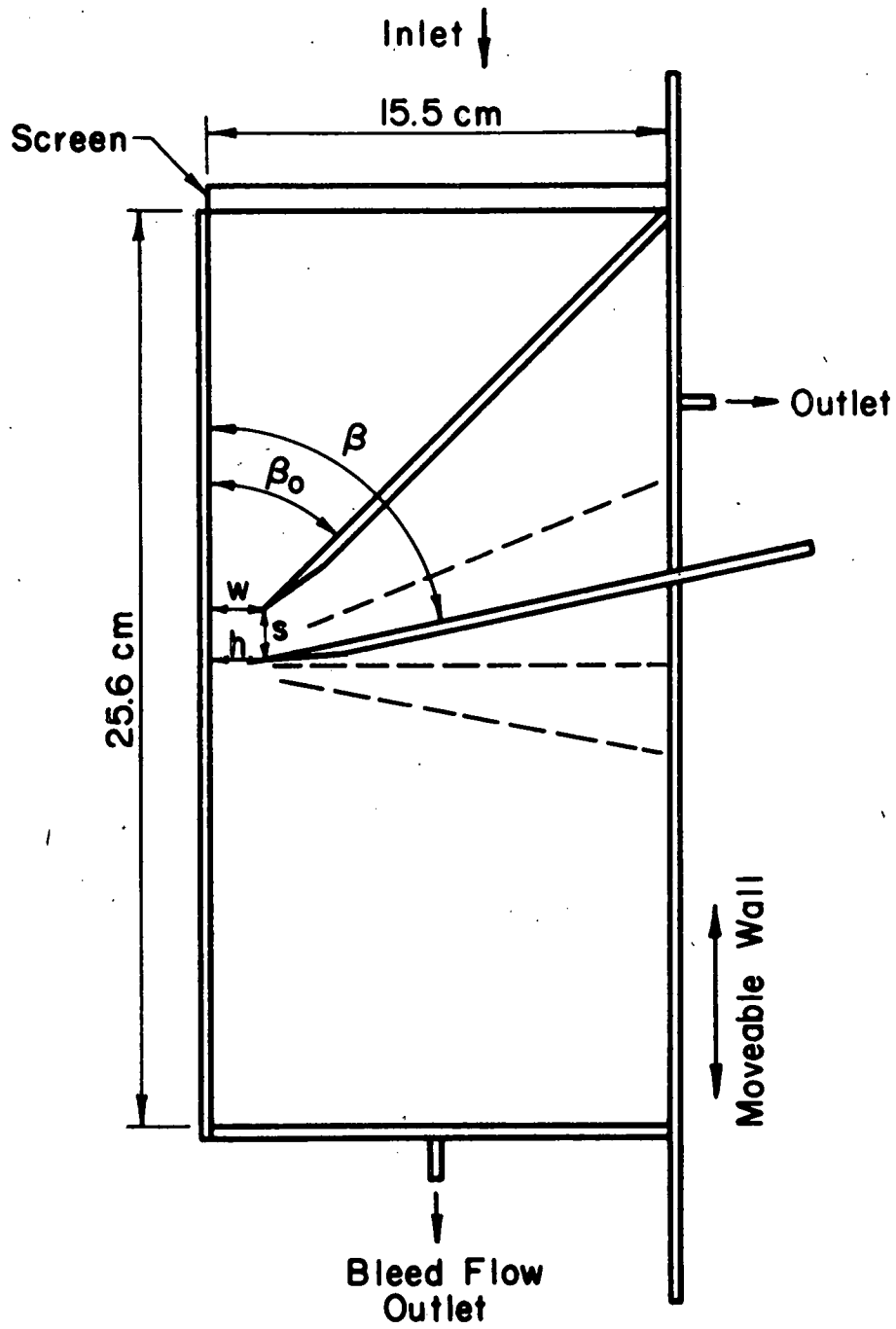

Fig. 4 Scaled-up Water Model

three injection lines positioned at the model throat in a plane midway between the top and bottom model surfaces. The model was designed with a fixed throat angle $\beta_o = 45^o$ and a variable deflecting plate angle $\beta = 101^o$, 90^o, 79^o, and 68^o.

3.4 Onset of Instabilities

The potential flow solution for virtual impactor geometries becomes indeterminate for large normalized void widths h/w (Forney, et al., 1978; Ravenhall, et al. 1978). The value of $h/w = h_{lim}/w$ at the onset of theoretically indeterminate geometries marks the development of fluid instabilities near the leading edge of the fluid deflecting plate. These instabilities appear as an unsteady kink or curl on the fluid streamline intersecting the leading edge of the plate. If the void width h/w is increased further the jet begins to protrude down into the void space below the impaction region and to separate from the defecting plate (see Fig. 7, Sec. 4) and the flow field, in general, becomes less stable. These instabilities undoubtedly contribute to the disparity which currently exists between experimental virtual impactor data and theoretical predictions. Recent attempts to theoretically correlate axisymmetric virtual impactor data have been unsuccessful (Marple, 1980) with regard to the magnitude of the internal particle losses. Attempts to correlate characteristics of the internal particle losses for two-dimensional virtual impactors (Forney, et al., 1980) have been moderately successful but the disparity between theory and experiment increased with larger void widths h/w. These latter results appear to be consistent with our observations of increased levels of instability in the scaled-up water models as the void width increased.

Theoretical values of the limiting void width h_{lim}/w have been determined over a range of deflecting plate angles β for each of three throat angles $\beta_o = 30^o$, 45^o and 60^o with bleed flows of f = 0 and 0.1 where f represents the fraction of the total flow which escapes into the void space. These results are shown in Fig. 5. Visual observations of the onset of instabilities for a constant throat angle $\beta_o = 45^o$ have been recorded with the water model and these values are also indicated in Fig. 5. As can be seen, the flow fields appear to be theoretically and experimentally more stable for intermediate values of the fluid deflecting plate angle $\beta \simeq 80^o$ at all values of throat angle β_o and bleed flows f. In particular, the experimental observations suggest that for a typical bleed flow of f = 0.1, plate angle $\beta = 90^o$ and throat angle $\beta_o = 45^o$, one may expect to have increasing difficulty correlating experimental virtual impactor data as h/w increases beyond $h/w \simeq 1.1$.

The effect of the secondary flow f on the magnitude of h_{lim}/w was also determined theoretically and experimentally. Fig. 6 demonstrates that the range of determinate geometries increases with increasing secondary flow f. It is apparent from these results that larger bleed flows into the void space would tend to stabilize the fluid flow patterns of two-dimensional devices.

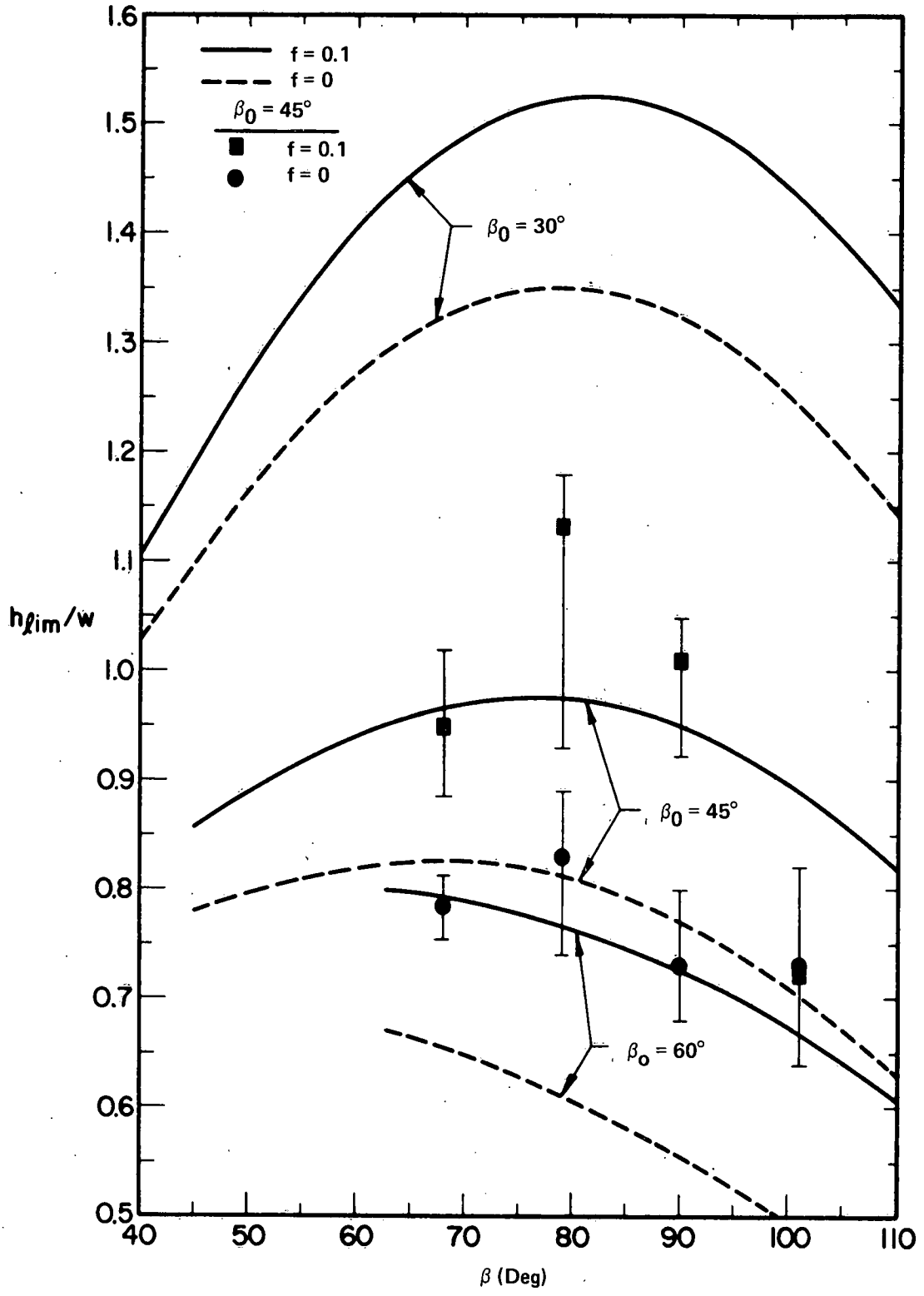

Fig. 5 Limiting Void Width versus Deflecting Place Angle β. Solid Lines Result from Potential Flow Analysis. Solid Points are Visual Observations of Onset of Fluid Separation on Top of Deflecting Plate

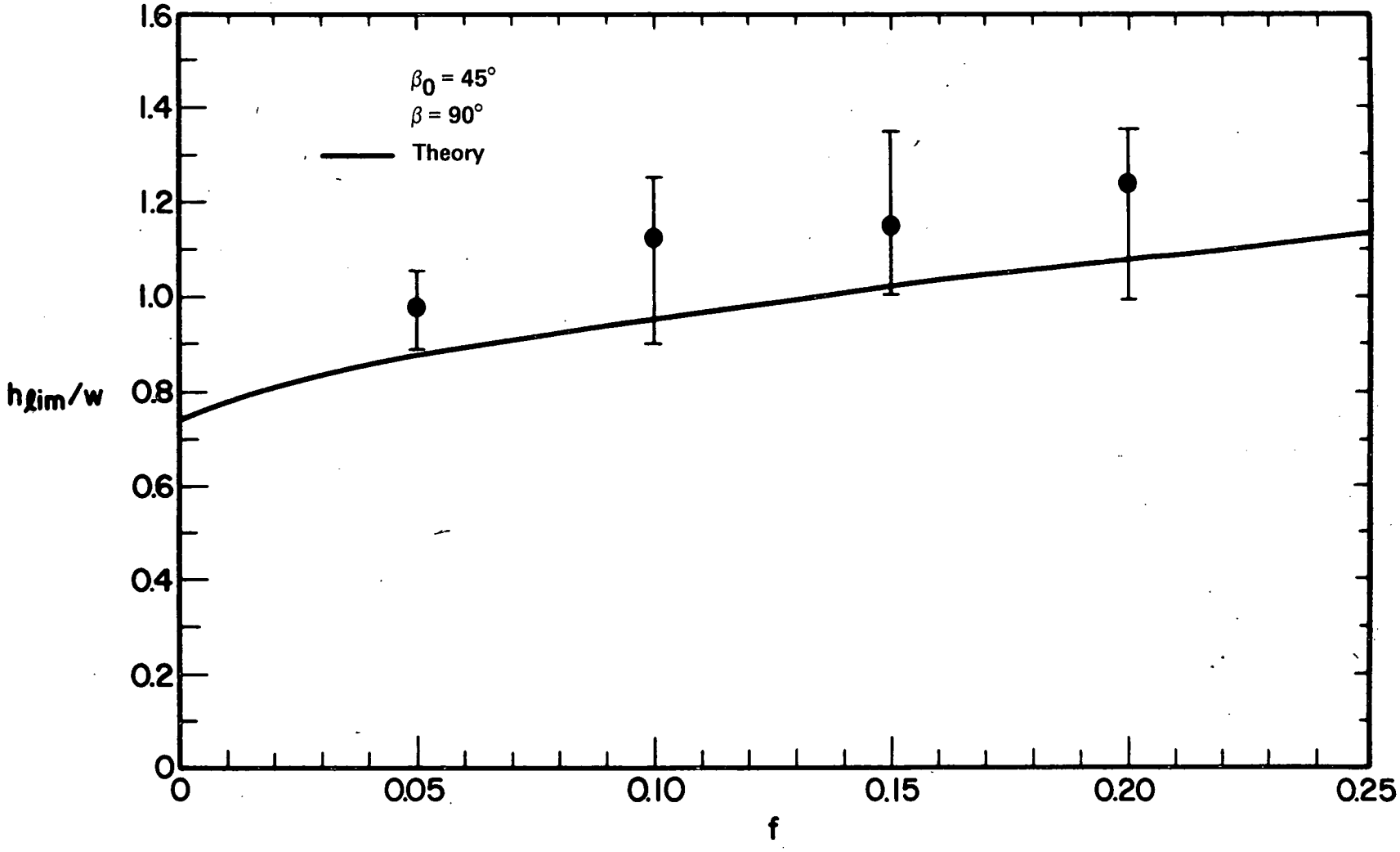

Fig. 6 Limiting Void Vidth Versus Magnitude of Bleed Flow f. Solid Lines Result from Potential Flow Analysis. Solid Points are Visual Observations of Onset of Fluid Separation on Top of Deflecting Plate

4. VISCOUS FLOW

4.1 Fluid Flow Fields

The Navier-Stokes equations were solved for flow field geometries of the type shown in Figs. 7 and 8. The equations were written in finite difference form and a relaxation technique was used to provide values of the stream function and fluid velocity at each of the node points in a rectangular grid. For the application of similar methods to axisymmetric virtual impactors the reader is referred to Marple (1980). The impactor geometries are constrained in this section, as in section 2, such that projections of the inclined throat walls of Figs. 7 and 8 and the fluid deflecting plates would intersect at a common point on the left wall of both figures. The dimensions of the device are expressed in terms of throat angle β_o, fluid deflecting plate angle β and normalized void width h/w in the same manner as illustrated in Fig. 1A.

Numerical calculations were performed for fixed $\beta = 90^o$, bleed flow $f = 0.1$ and $Re = \frac{\rho \bar{u} w}{\eta} = 1540$ for each of three throat angles $\beta_o = 38^o$, 45^o and 58.2^o, covering the range of normalized void width $0.6 \leq h/w \leq 1.5$. The value of $Re = 1540$, corresponding to some of our experimental observations, was chosen since little difference in fluid flow properties was noted for $Re > 10^3$ and it would be unusual to operate at smaller values of Re.

Fluid streamlines are shown in Figs. 7 and 8 for h/w = 1.0, 1.5. Interior streamlines representing percent of fluid flow passing to the left of each streamline within the throat are shown for values of 10%, 50% and 90%. In addition outer streamlines representing the boundary between recirculating flow and the jet are shown. As noted in Fig. 7 the 10% streamline has just begun to protrude into the void space and there is some separation on the horizontal fluid deflecting plate. This is consistent with the

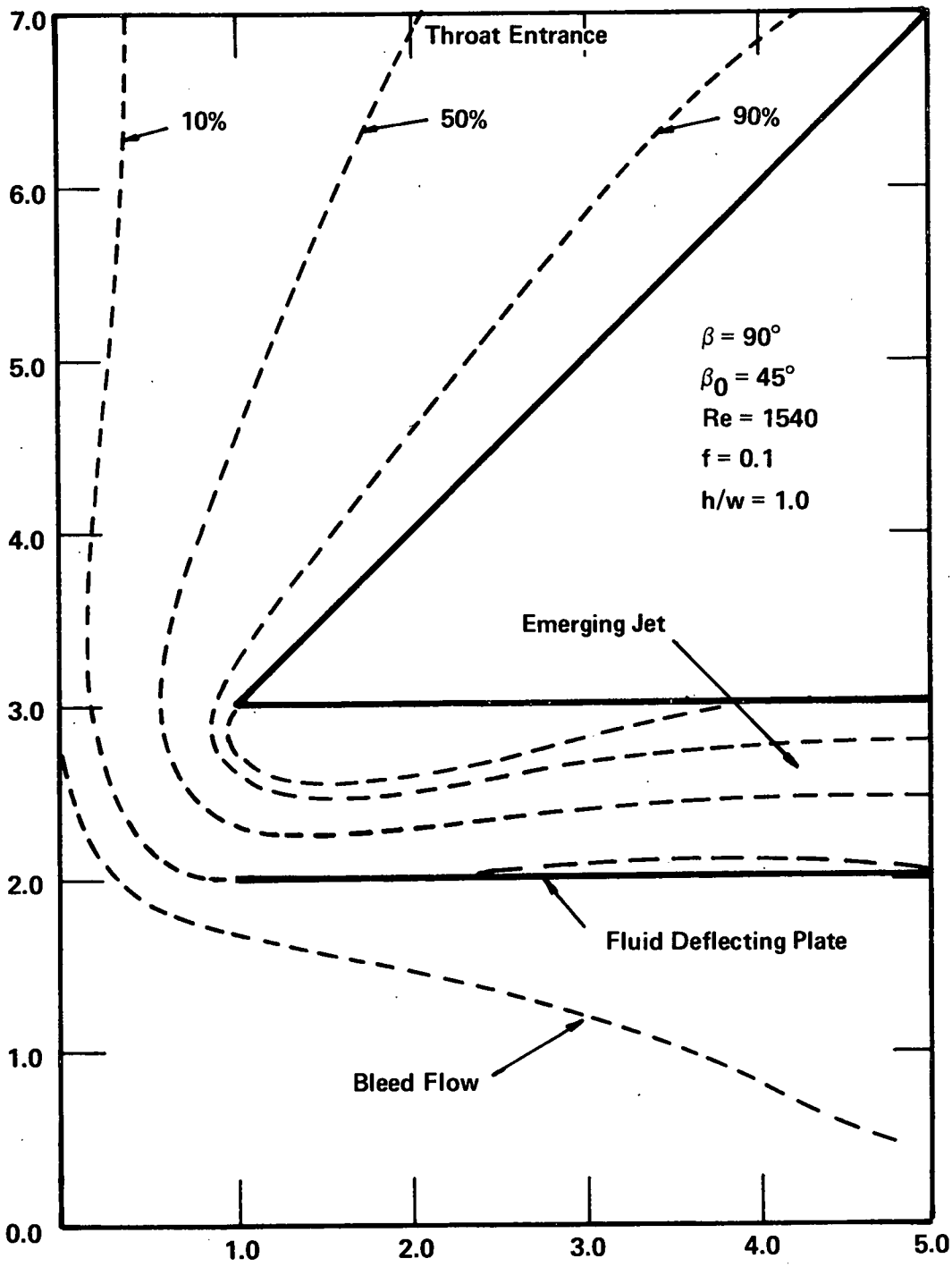

Fig. 7 Fluid Streamlines (viscous flow)

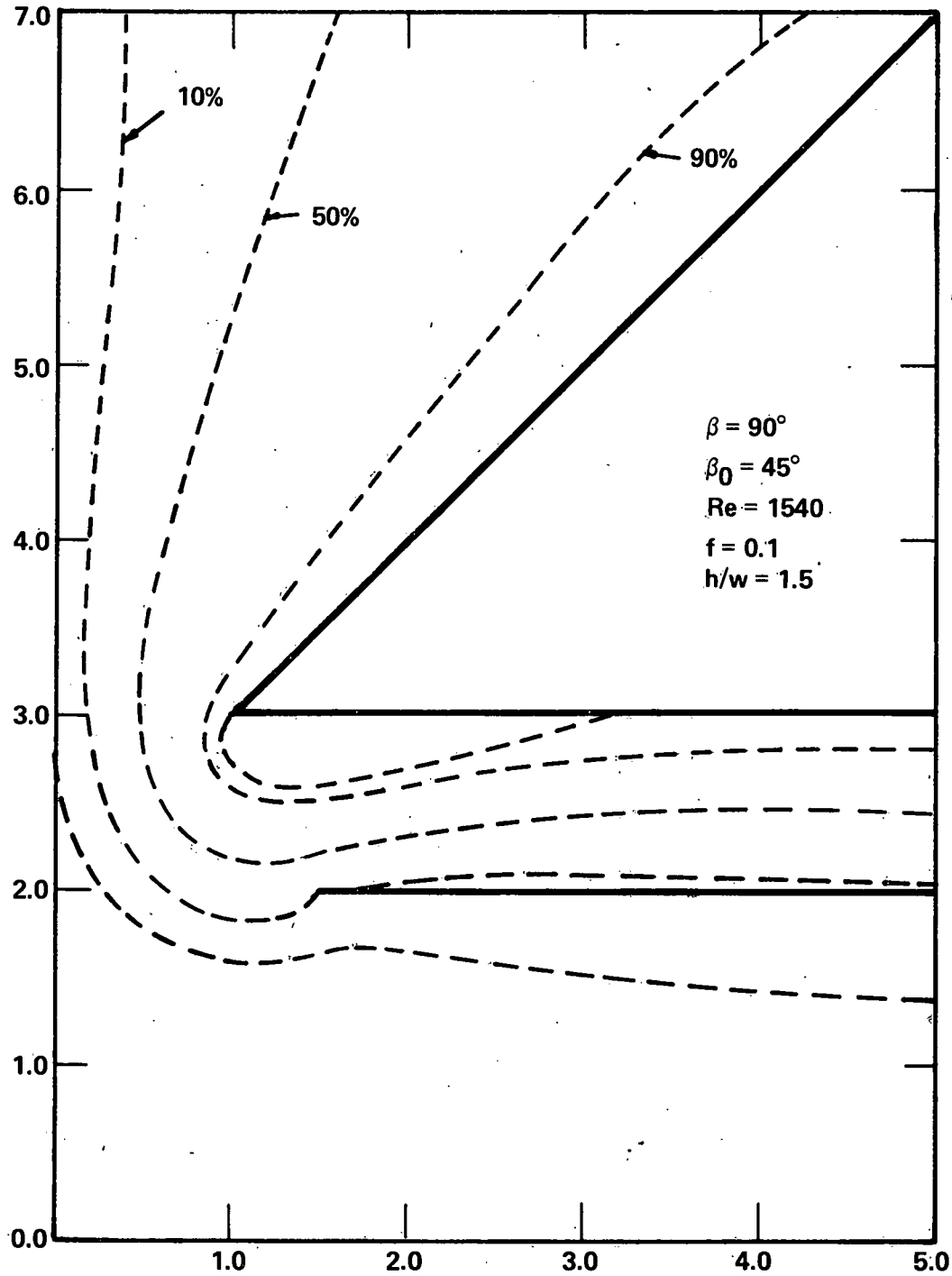

Fig. 8 Fluid Streamlines (viscous flow)

prediction of the onset of separation for this geometry at h/w ≃ .95 from the results of the potential flow analysis indicated in Fig. 5. At larger void widths the fluid protrudes further into the void space with greater separation on the deflecting plate as shown in Fig. 8.

4.2 Particle Trajectories

Fluid velocities at each of the node points in the rectangular grid system covering the device geometry are inserted into the equations of motion (Stokes' Law) for a particle. The procedure for following particle trajectories in the flow field is similar to that outlined in Section 3.2 where Stokes Law and other dimensionless quantities are defined. It is assumed here, as before, that particles are distributed uniformly across the throat entrance. Particles are inserted into the incident jet, at some reasonable distance from the throat, with initial velocities equal to the local fluid velocity.

Particles are followed in the flow field as a function of starting position and Stokes parameter $\psi^{\frac{1}{2}}$, and the remaining procedure is similar to that outlined in Section 3.2. Referring to Fig. 9, a trajectory is followed until (A) it enters the void space or the bleed flow which is designated as region v, or (B) it collides with the plate designated by region p, or (C) it escapes with the emerging jet designated by region e. In the absence of doubled valued contours with respect to $\psi^{\frac{1}{2}}$ which can occur in both potential or viscous flow fields, it is easy to construct, as shown in Fig. 9, the total efficiency E_T representing the fraction of particles entering the device which do not escape in the emerging jet. Likewise, E_V represents the fraction of particles which enter the void space or the bleed flow. The

fraction of particles which strike the fluid deflecting plate is L, the vertical distance between E_T and E_V or $L = E_T - E_V$.

For the device geometry of Fig. 9 the void width is narrow and the fraction of particles which strike the plate is large. As the void width h/w is increased the region p representing the fraction of particles striking the plate collapes until it can represent a quite irregular region as shown in Fig. 10. These contours are clearly double valued with respect to $\psi^{\frac{1}{2}}$ and care must be taken to construct the efficiencies E_T and E_V. For these device geometries, particles pass down into the void space with the jet near the leading edge of the fluid deflecting and some may be swept back up into the emerging jet and down onto the top of the fluid deflecting plate. As the void width h/w is increased the region p disappears in which case no particles strike the plate and $E_T = E_V$ as shown in Fig. 11.

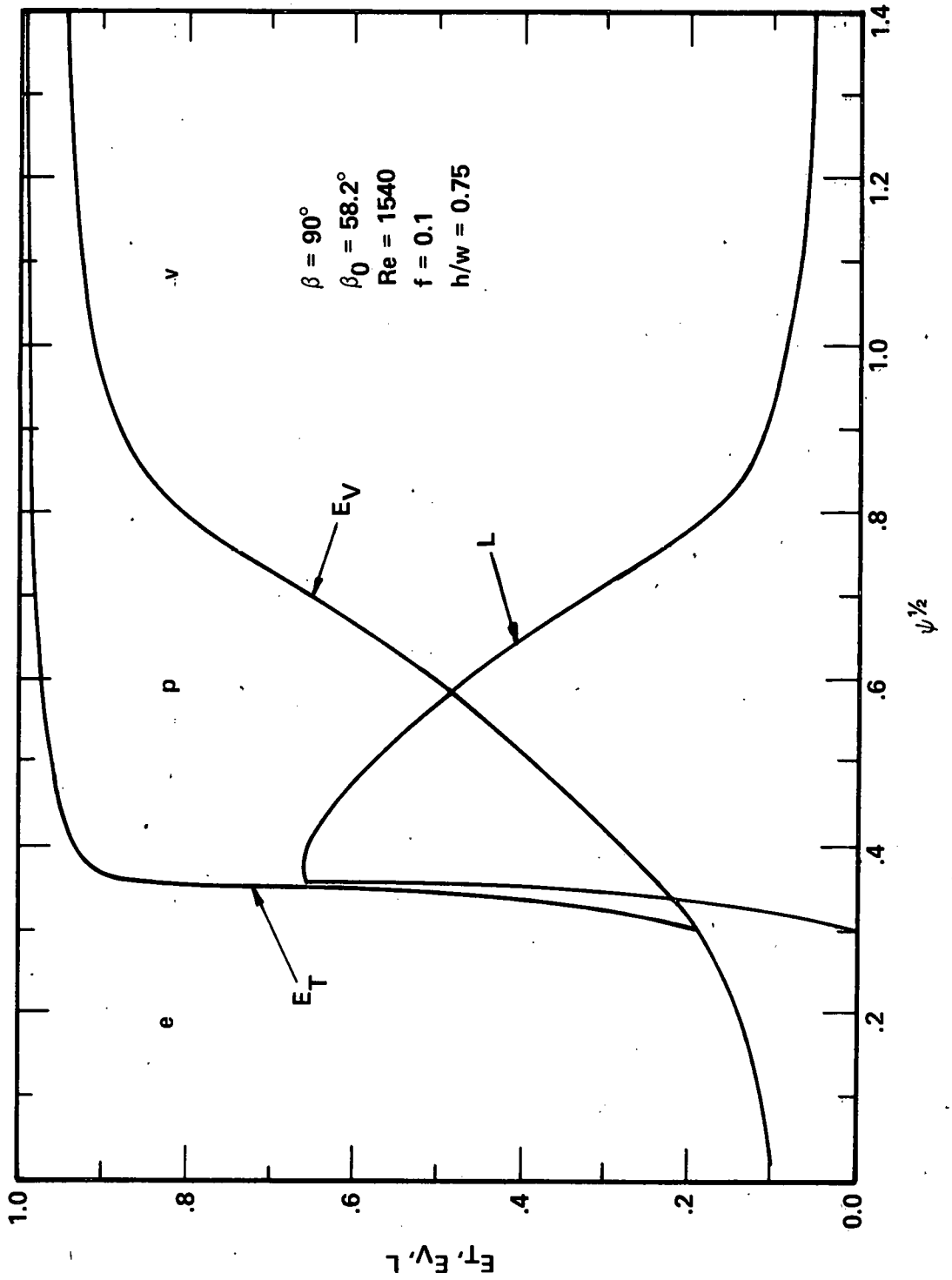

Fig. 9 Particle Efficiency Curves (viscous flow). e Represents Region where Particles are in Emerging Jet, p where Particles Strike Fluid Deflecting Plate and v where Particles Enter Bleed Flow or Void

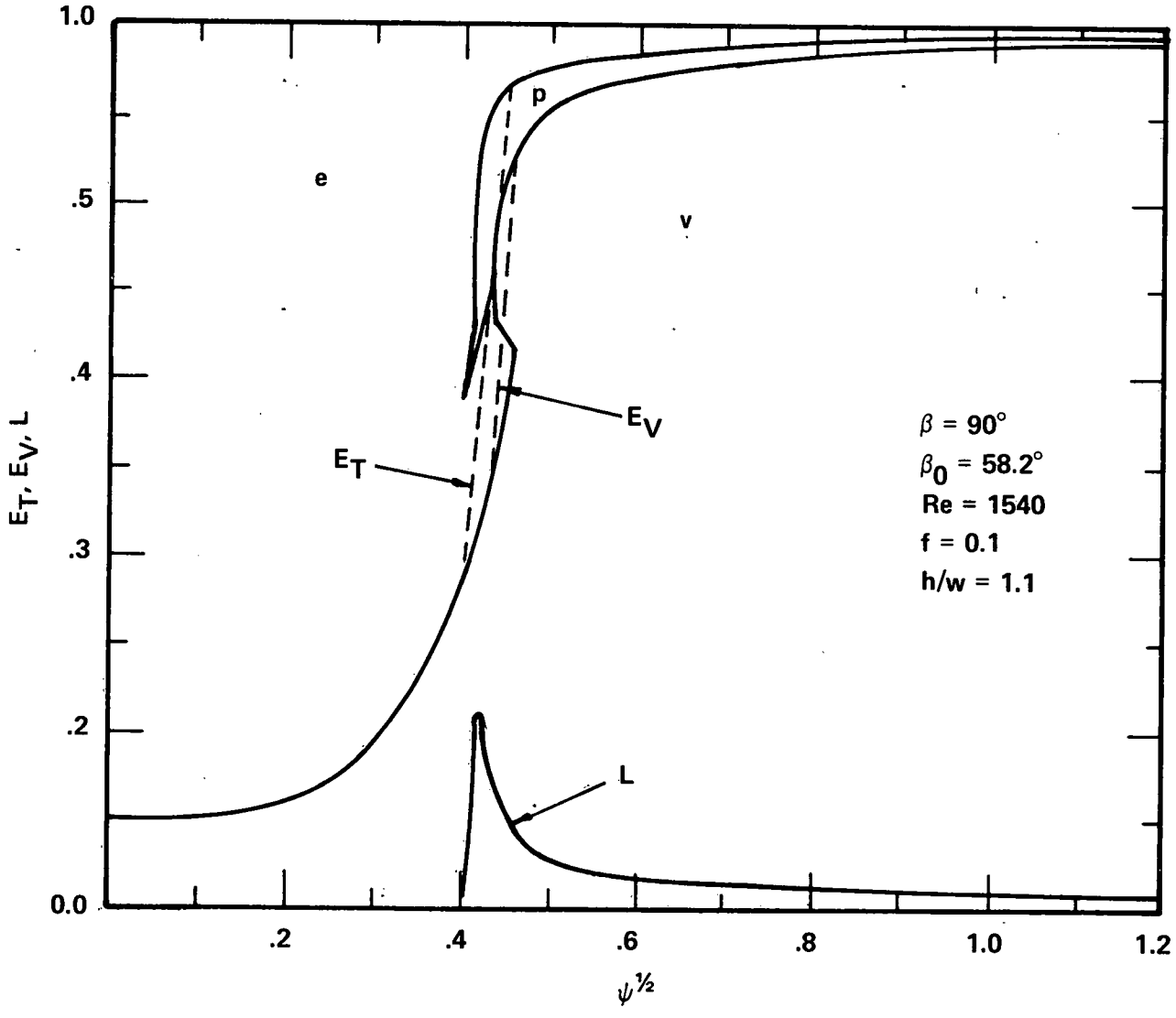

Fig. 10 Particle Efficiency Curves (viscous flow)

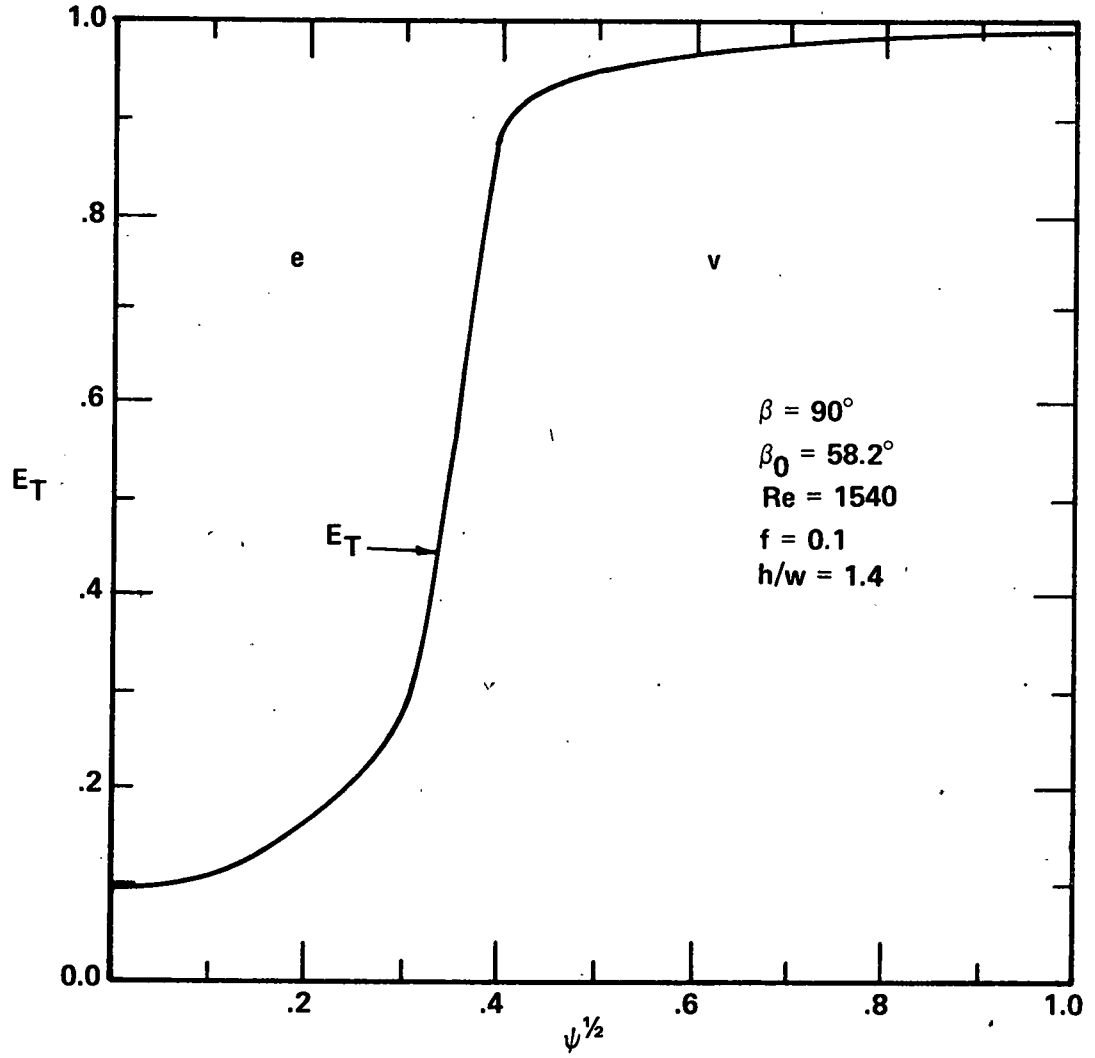

Fig. 11 Particle Efficiency Curves (viscous flow)

5. OPERATING CHARACTERISTICS

Particle efficiency curves were determined for fixed bleed flow f = 0.1 and fluid deflecting plate angle $\beta = 90^{\circ}$ for each of three throat angles $\beta_o = 38^{\circ}$, 45° and 58.2°. The potential flow calculations for the mappings assumed were constrained by a upper limit to the normalized void width $h/w = h_{lim}/w$. There were no constraints on the magnitude of h/w for viscous flow calculations and particle efficiency curves were determined for the range $0.7 \leq h/w \leq 1.5$.

To fully characterize the influence of geometry on virtual impactor performance, several important operating parameters are defined which describe salient features of the particle efficiency curves. These are identical to those defined earlier by Forney et al. (1980). The first parameter called the particle cutoff diameter is the value of $\psi^{\frac{1}{2}}$ for which the total efficiency is

$$E = \frac{1 + f}{2} \tag{21}$$

where f is the fraction of the total air flow in the bleed flow. Thus for f = 0.1, we define a parameter

$$\psi^{\frac{1}{2}} \left(E = \frac{1 + f}{2}\right) = \psi_{55}^{\frac{1}{2}} \tag{22}$$

proportional to the particle cutoff diameter. This characterizes the cutoff diameter for the primary flow. The results of the numerical computations of $\psi_{55}^{\frac{1}{2}}$ are shown in Fig. 12. The computed values of $\psi_{55}^{\frac{1}{2}}$ appear to be relatively insensitive to changes in void width.

Also of interest is a second parameter S which we call the relative dispersion. This represents a measure of the spread of the particle efficiency curve E_T about the particle cutoff diameter. Since an ideal

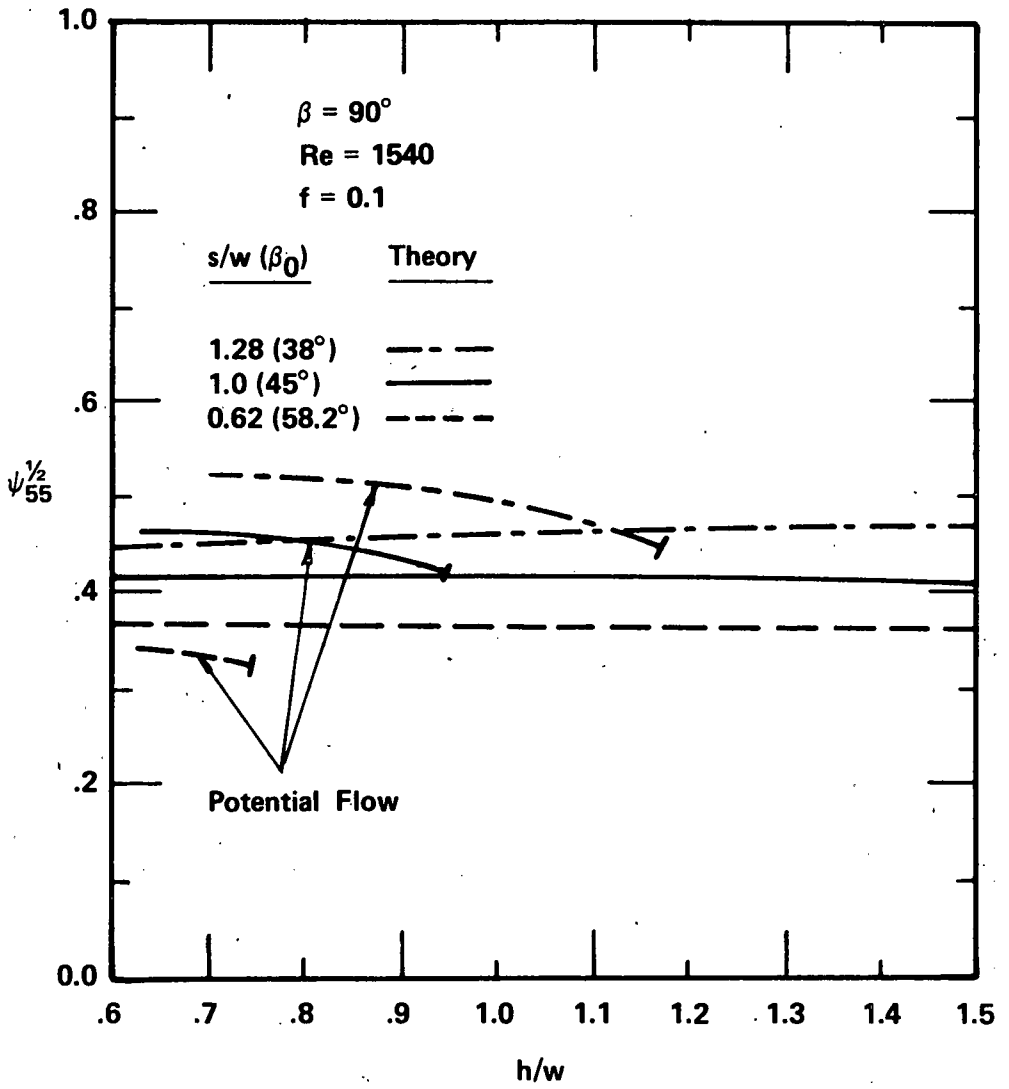

Fig. 12 Particle Cutoff Parameter versus Normalized Void Width h/w

impactor would provide values of S equal to 0, one seeks to minimize S for real devices. Formally, S is an estimate of the slope of the efficiency curve $d(\ln \psi^{\frac{1}{2}})/dE$ evaluated at $E_T = .55$ for $f = 0.1$. Here, we define S in the segment of the efficiency curve away from the influence of the secondary flow as

$$S = \frac{\psi^{\frac{1}{2}}(E = .84 + .16f) - \psi^{\frac{1}{2}}(E = .16 + .84f)}{(.68)(1-f)\ \psi^{\frac{1}{2}}(E = .5 + .5f)} \tag{23}$$

where, in this study

$$S\ (f = 0.1) = \frac{\psi^{\frac{1}{2}}_{856} - \psi^{\frac{1}{2}}_{244}}{(0.612)\ \psi^{\frac{1}{2}}_{55}}$$

The numerical computations of the relative dispersion S are shown in Fig. 13. It is clear from Fig. 13 that the relative dispersion S increases, and the device becomes less desirable as a particle size classifier, as the void width h/w increases. Improved performance is also indicated for larger throat angles β_o for both potential and viscous flow calculations.

An additional parameter defined is the peak L_m in the loss factor L which represents the fraction of particles of a given $\psi^{\frac{1}{2}}$ which make contact with the fluid defecting plate shown in Figs. 1(A) and 7. The results of the numerical calculations of L_m are shown in Fig. 14. The sharp peak values of L_m computed by potential flow calculations shown in Fig. 14 are blunted when one includes the effects of viscous boundary layers. In addition, the peak values of L_m are sharply reduced as the void width h/w increases.

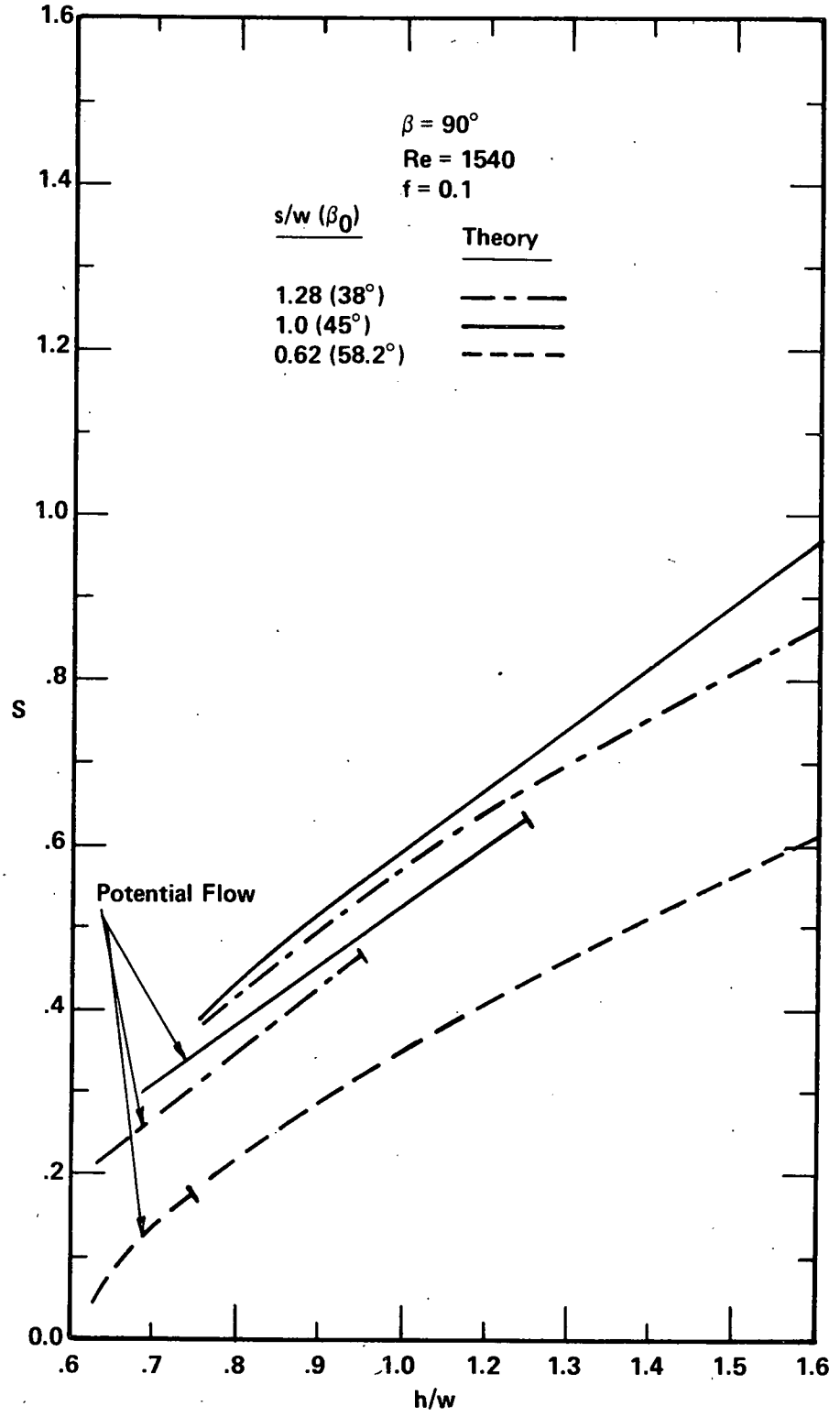

Fig. 13 Relative Dispersion S versus Normalized Void Width h/w

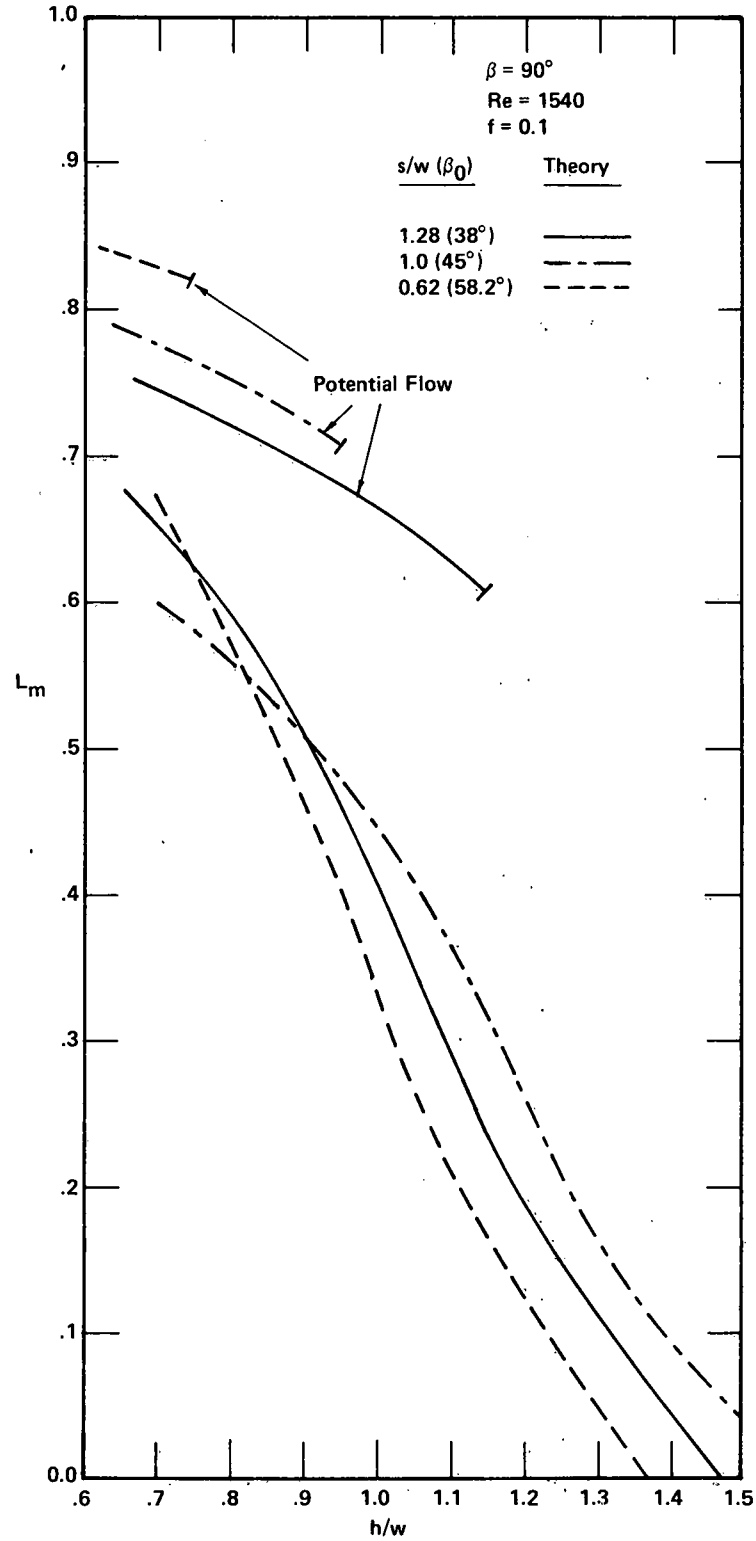

Fig. 14 Peak in Loss Factor versus Normalized Void Width

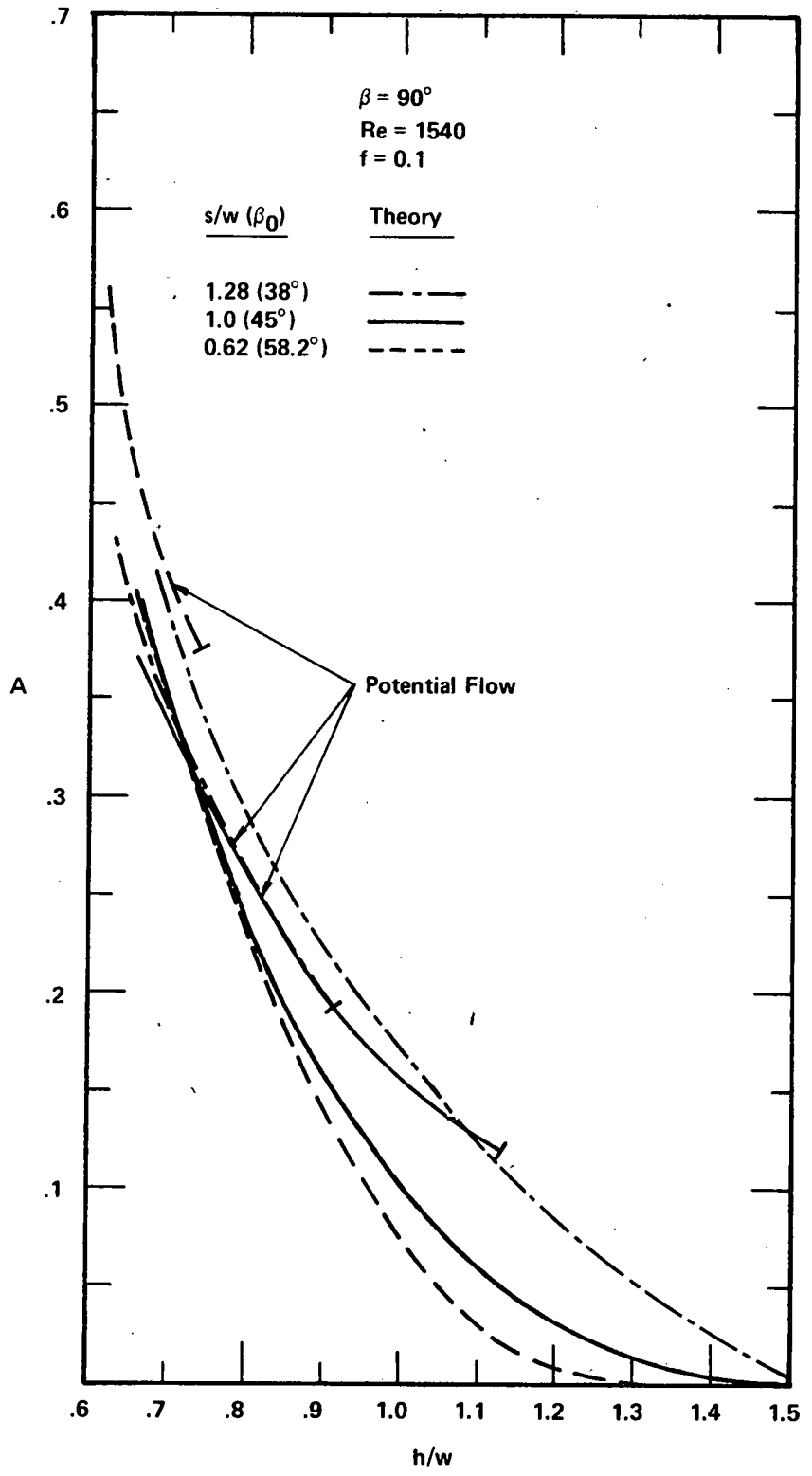

Fig. 15 Area Under Loss Factor versus Normalized Void Width

The final parameter defined is the area under the loss factor L. Thus we define a normalized area under the loss factor as

$$A = \int_0^{\infty} L(\psi^{\frac{1}{2}})\, d\, \psi^{\frac{1}{2}} \tag{25}$$

The results of numerical computation of A are shown in Fig. 15. As indicated there is a marked decrease in A as the void width increases to the value of $h/w = 1.4 \pm 0.1$ where $A \to 0$. The viscous flow calculations also indicate that some improvement would result by operating at larger throat angles β_o.

6. REFERENCES

1. Dzubay, T. B., and Stevens, R. K., Environ. Sci. Technol. 9, 663 (1975).

2. Loo, B. W., Jaklevic, J. M., and Goulding, F. S., Lawrence Berkeley Laboratory Pub. LBL-3854, Berkeley, California (1975).

3. Forney, L. J., Ravenhall, D. G., and Winn, D. S., J. Appl. Phys. 49, 2339 (1978).

4. Ravenhall, D. G., Forney, L. J., and Jazayeri, M., J. Colloid Interface Sci. 65, 108 (1978).

5. Marple, V. A., and Chien, C. M., Environ. Sci. Technol. 14, 976 (1980).

6. Forney, L. J., Rev. Sci. Instrum. 10, 1264 (1976).

7. Forney, L. J., Ravenhall, D. G., and Lee, S. S., Environ. Sci. Technol. (submitted, 1980).

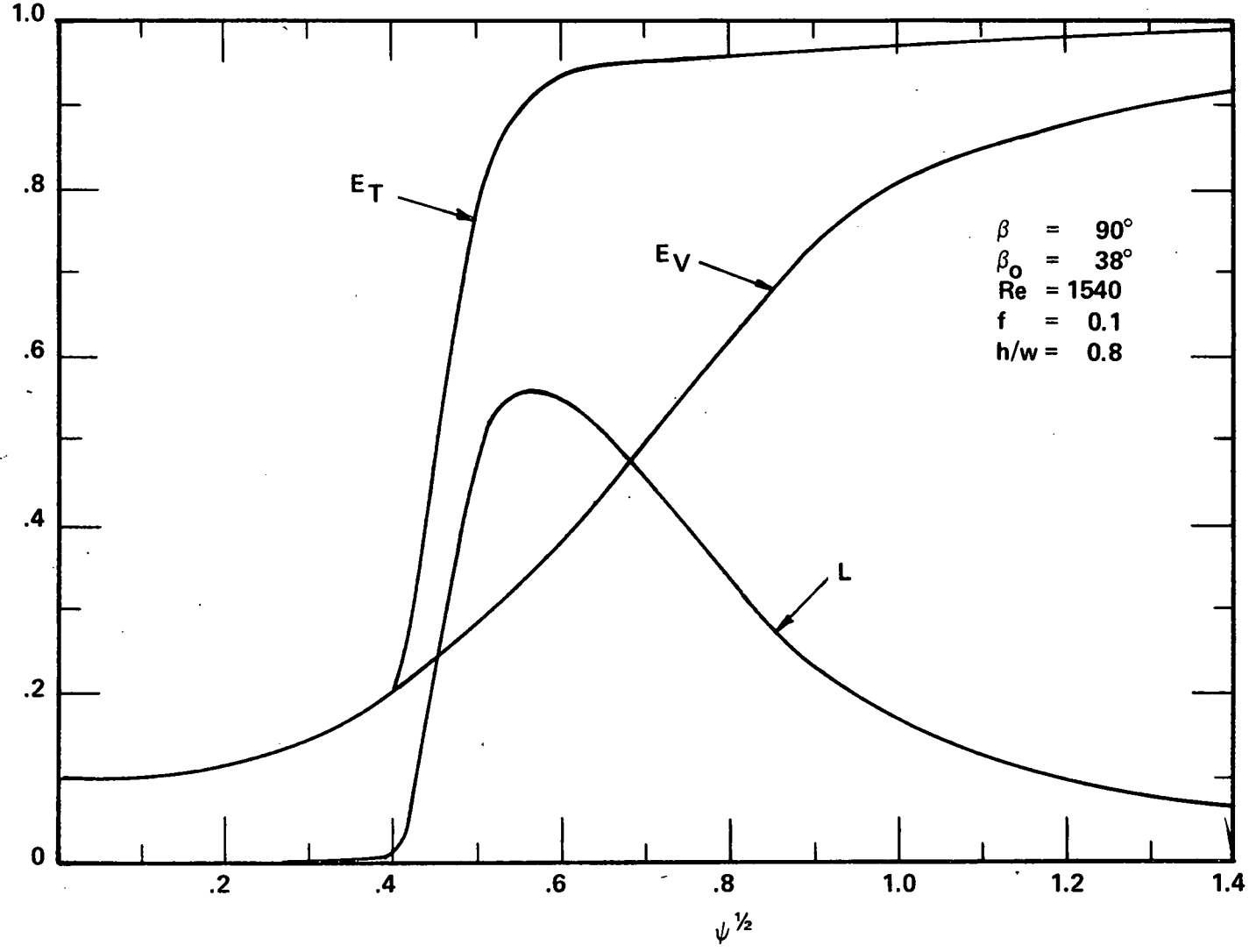

Fig. 16 Particle Efficiency Curves (viscous flow)

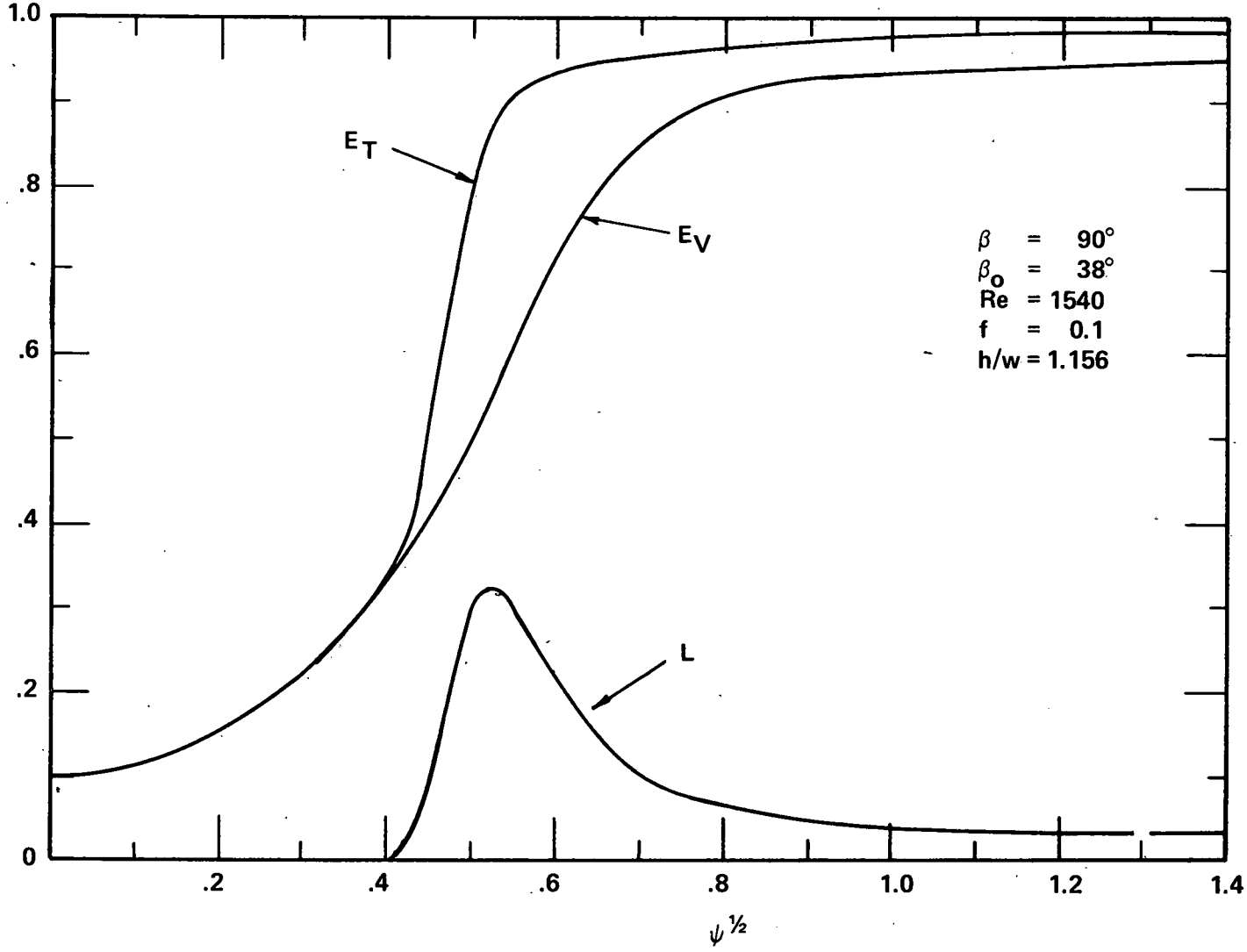

Fig. 17 Particle Efficiency Curves (viscous flow)

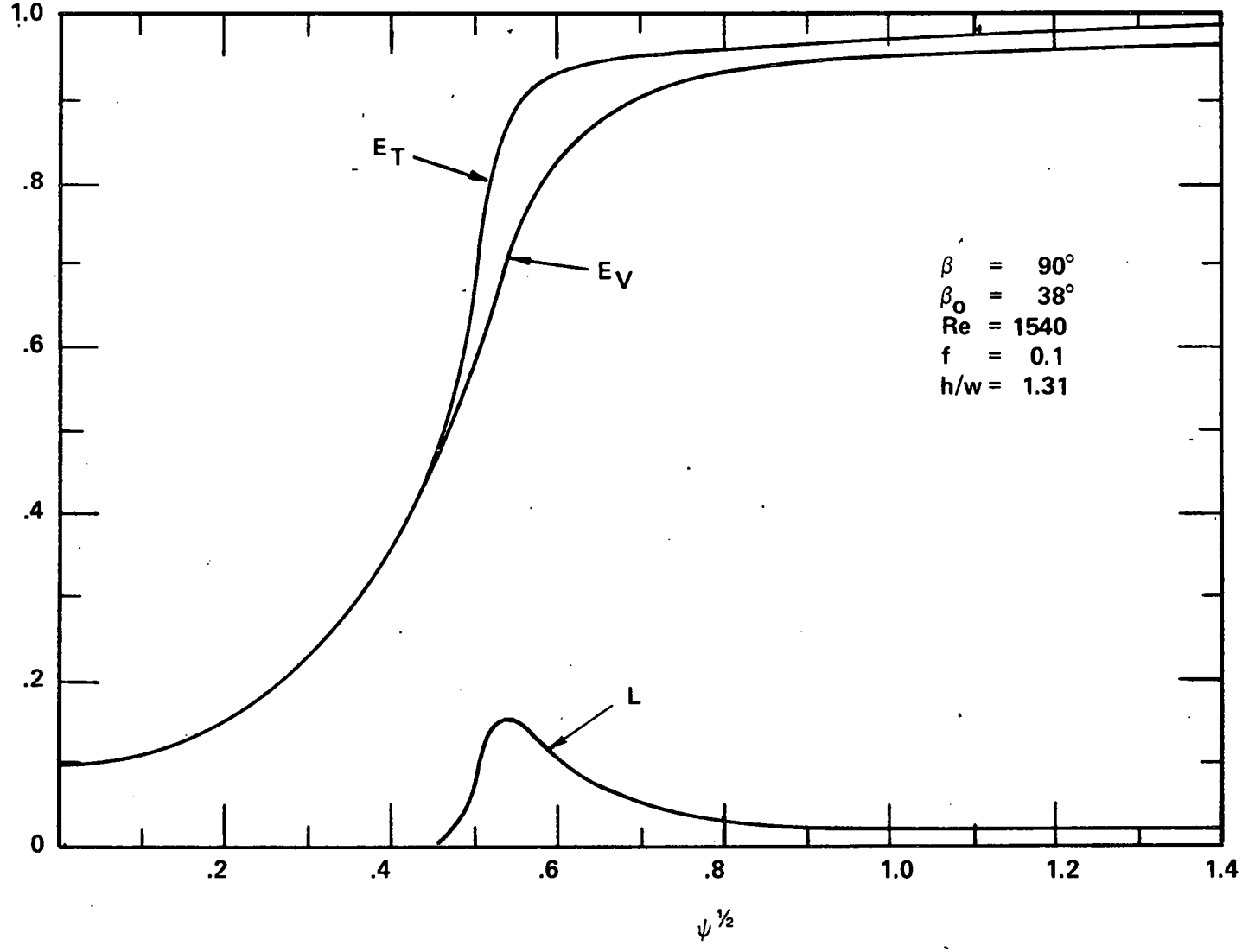

Fig. 18 Particle Efficiency Curves (viscous flow)

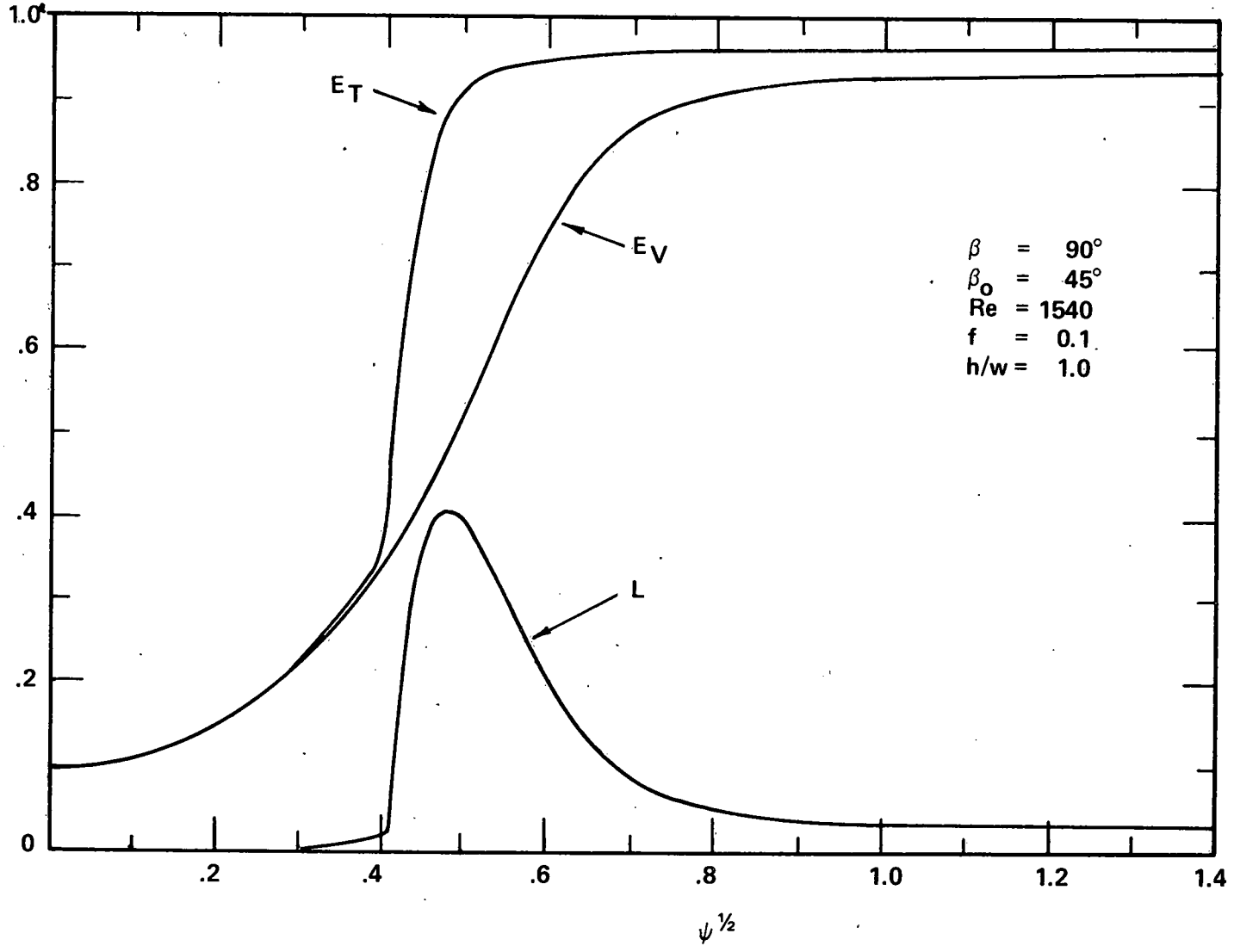

Fig. 19 Particle Efficiency Curves (viscous flow)

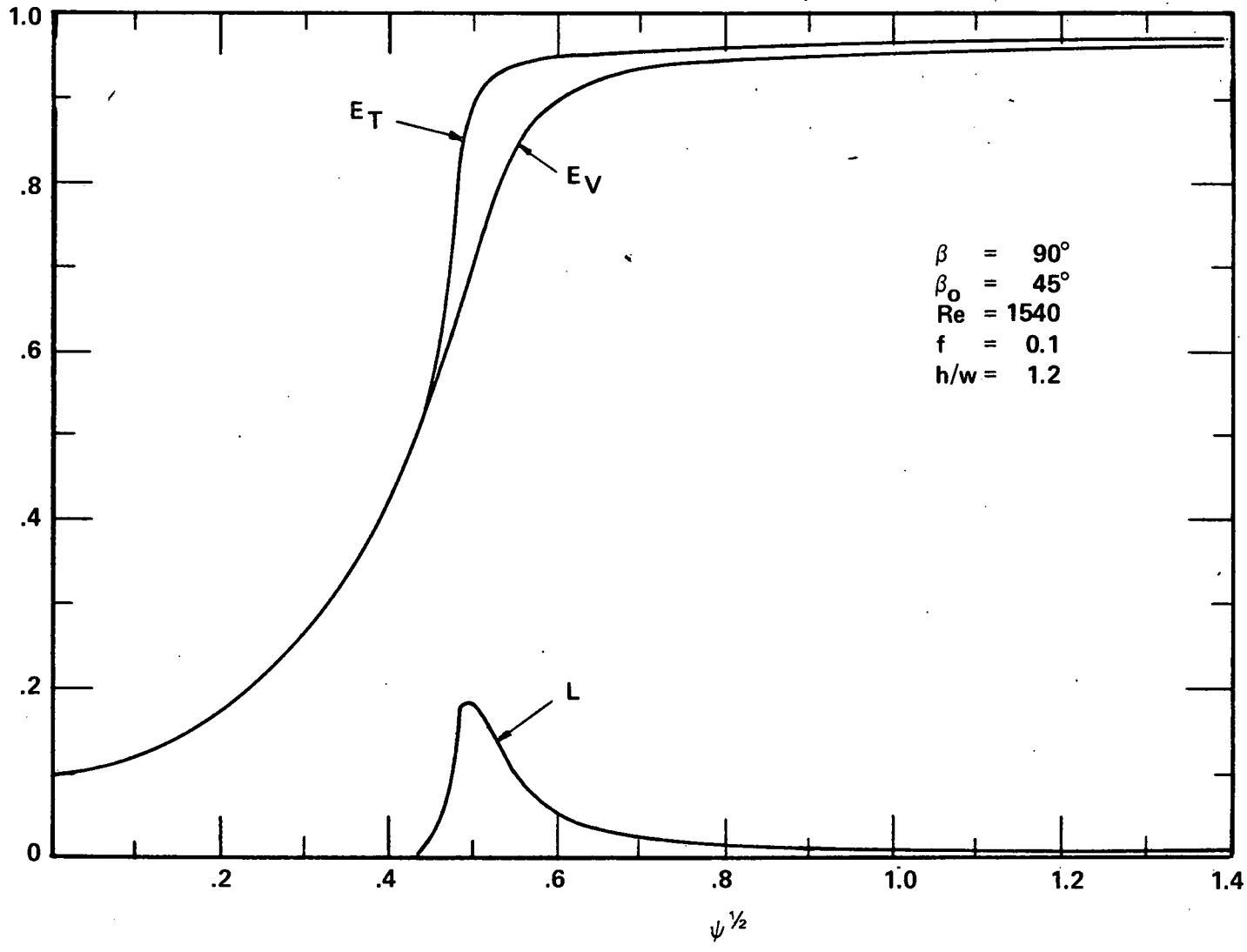

Fig. 20 Particle Efficiency Curves (viscous flow)

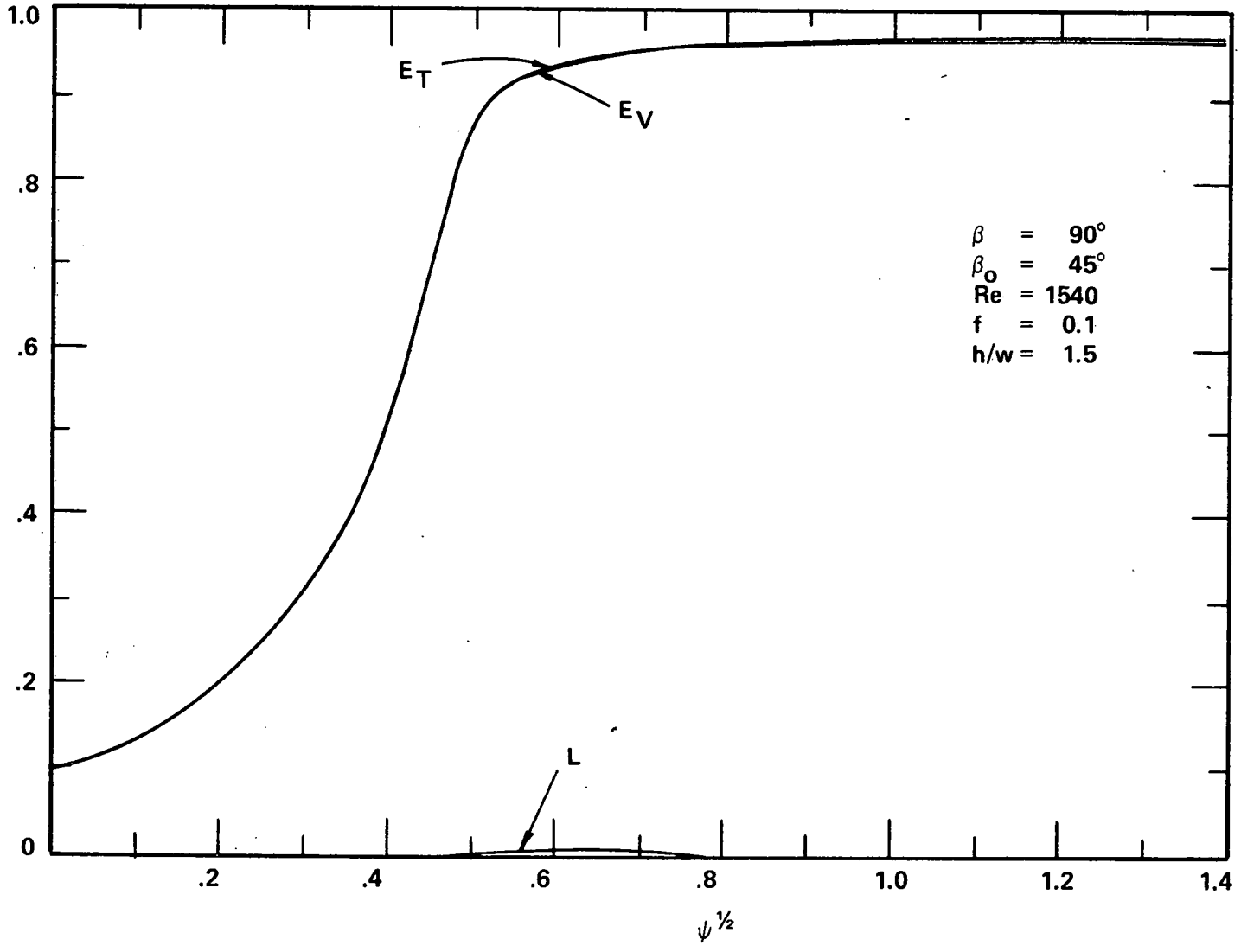

Fig. 21 Particle Efficiency Curves (viscous flow)

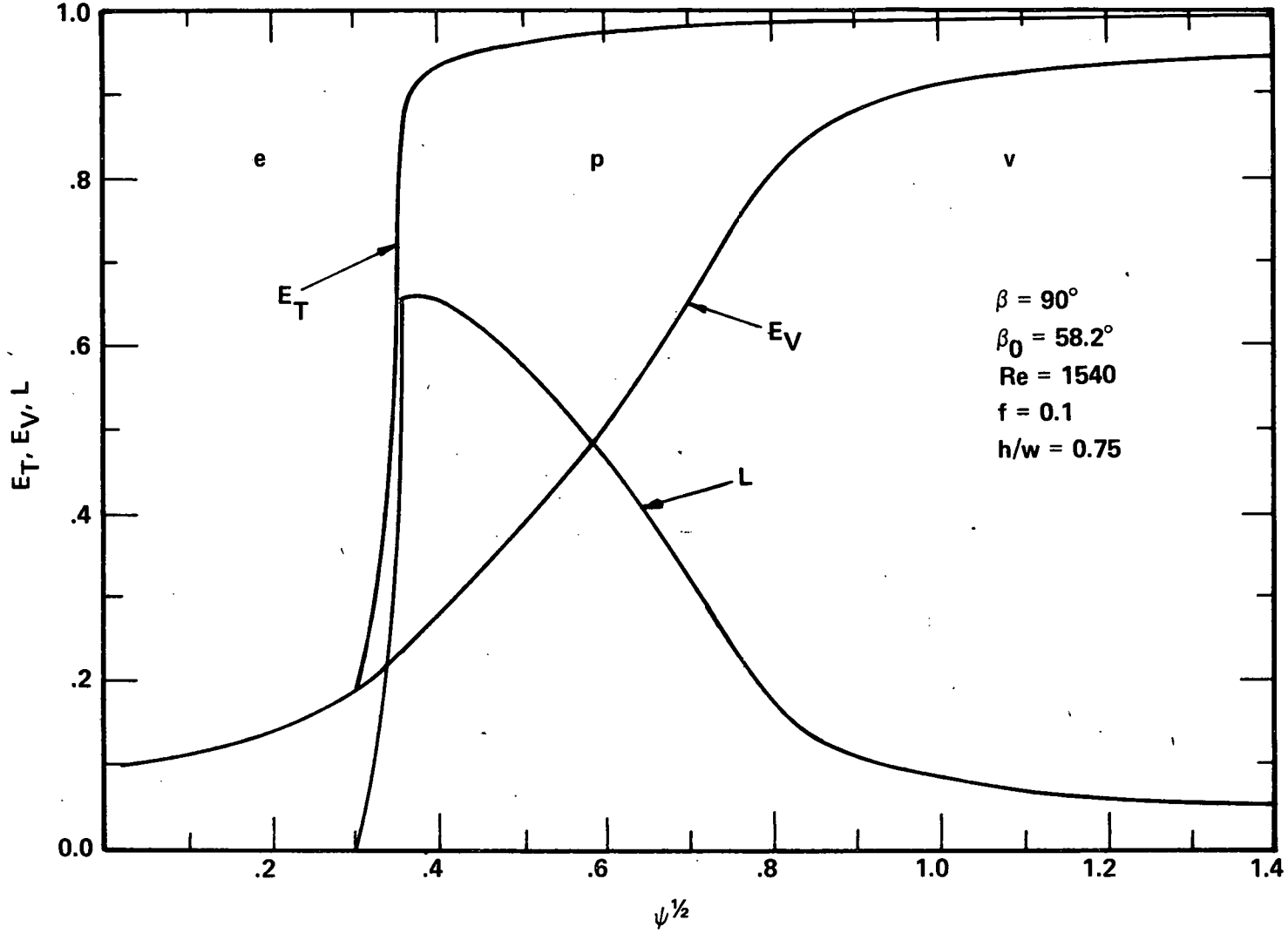

Fig. 22 Particle Efficiency Curves (viscous flow)

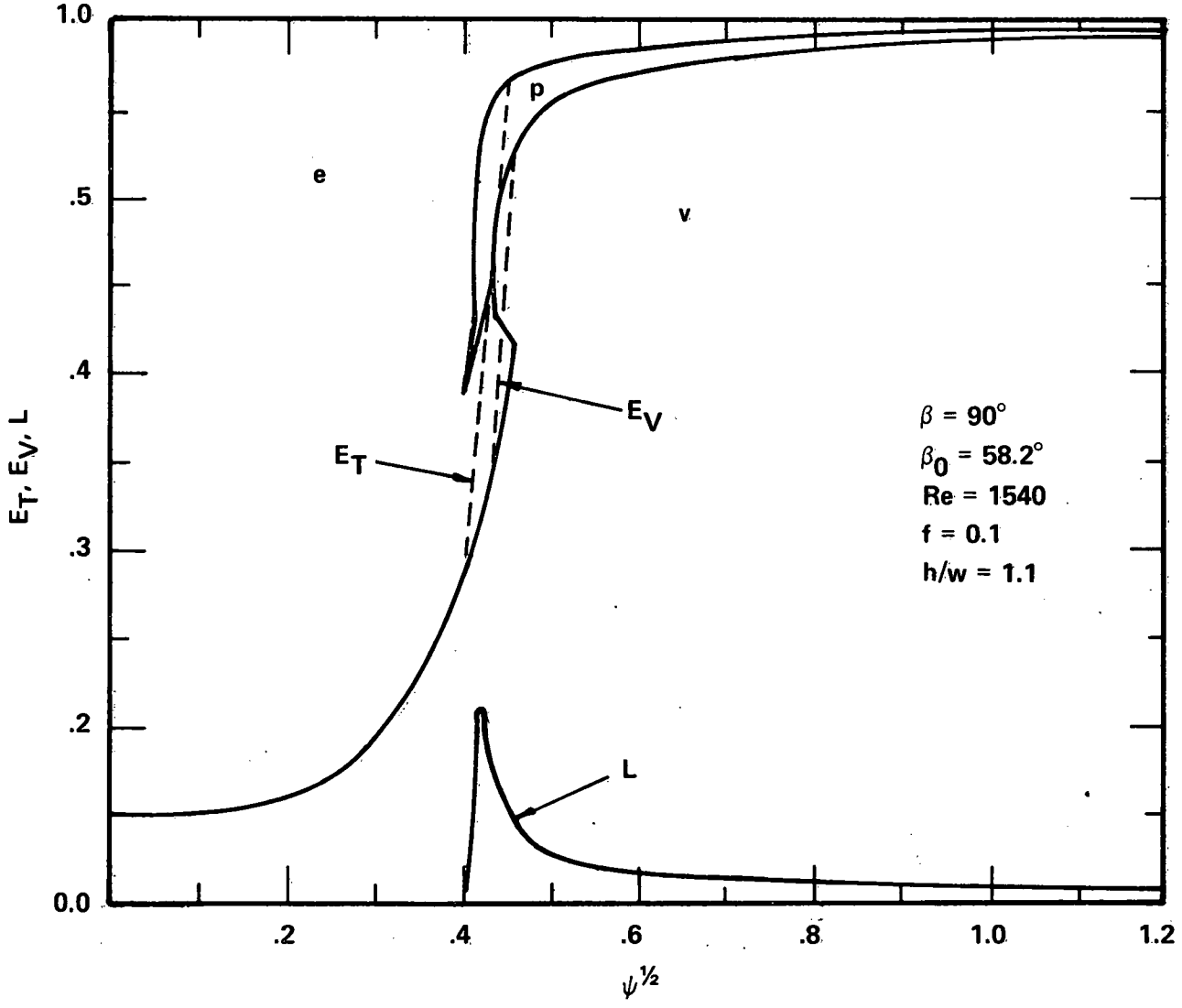

Fig. 23 Particle Efficiency Curves (viscous flow)

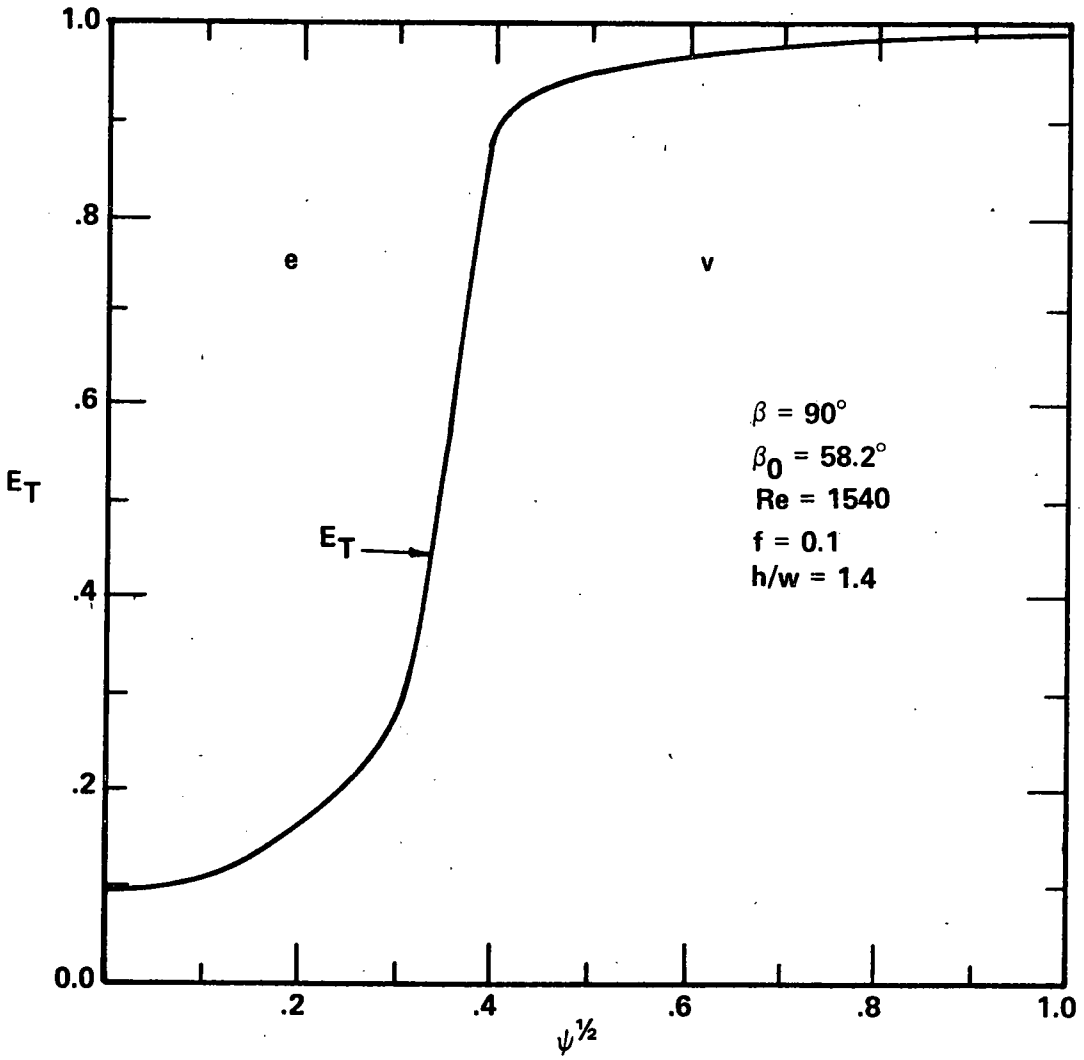

Fig. 24 Particle Efficiency Curves (viscous flow)

III. PROJECT MANAGEMENT

1. PROJECT COMPLIANCE

The objectives of the proposed work have been accomplished. Potential and viscous flow solutions have been developed to predict the particle sizing characteristics of two-dimensional virtual impactors. Tests have been conducted on the prototype device covering a wide range of instrument geometries. The effect on the particle loss spectrum of an excess clean air flow into the void space has been explored. Salient features of the efficiency curves and loss spectrums have been measured and recorded and the results have been correlated with theoretical results.

2. PERSONNEL CONTRIBUTIONS

Name	Level	Period
Dr. L. J. Forney	1/4 time	6/1/77-12/30/80
Dr. D. G. Ravenhall	1/8 time	6/1/77-12/30/80
Mr. D. S. Winn	1/3 time	1/21/77-6/21/77
Mr. S. S. Lee	2/3 time	8/1/77 -8/1/78
Mr. W. M. Langlois	1/4 time	8/1/77-8/1/78
Mr. M. Jazayeri	NSF Fellowship	6/15/77-8/15/77
Mr. A. J. Hubbard	1/3 time	8/1/78-1/1/80
Mr. E. W. Cannon	1/3 time	8/1/78-8/1/79
Ms. Z. Giz	1/4 time	8/1/78-8/1/79
Mr. H. C. Lee	1/2 time	3/1/80-12/30/80

3. PRESENTATIONS

Forney, L. J. and Ravenhall, D. G., "Aerosol Impactors: A Two-Dimensional Jet of Ideal Fluid Impinging upon a Void," Proceedings of the Eighth U.S. National Congress of Applied Mechanics, Los Angeles, CA, June 1978.

Forney, L. J. and Ravenhall, D. G., "Use of Potential Flow to Correlate Virtual Impactor Data," Proceedings of ACS 177th National Meeting, Honolulu, Hawaii, April 1979.

Forney, L. J., "Recent Developments in Aerosol Sizing," Department of Civil Engineering, Georgia Institute of Technology, Atlanta, GA, January 1979.

Forney, L. J., "Recent Developments in Aerosol Sizing," Atmospheric Science Laboratory, University of Illinois, February 1979.

Ravenhall, D. G., "Theoretical Studies of Particle Impactors," Department of Physics, University of Illinois, February 1979.

Forney, L. J. and Ravenhall, D. G., "Experimental and Theoretical Studies of Particle Impactors," 12th Aerosol Technology Meeting, General Motors Research Laboratories, Warren, Michigan, August 1979.

Forney, L. J. and Ravenhall, D. G., "Experimental and Theoretical Study of a Virtual Impactor", 1981 American Industrial Hygiene Conference, Portland, Oregon, May 1981 (abstract submitted).

4. PUBLICATIONS

Forney, L. J., Ravenhall, D. G. and Winn, D. S., "Aerosol Impactors: A Study of a Fluid Jet Impinging upon a Void," Journal of Applied Physics, 49, 2339 (1978).

Ravenhall, D. G., Forney, L. J. and Jazayeri, M., "Aerosol Sizing with a Slotted Virtual Impactor," Journal of Colloid and Interface Science, 64, 108 (1978).

Ravenhall, D. G. and Forney, L. J., "Aerosol Impactors: Calculation of Optimum Geometries," Journal of Physics E., Scientific Instrumentation, 13, 87 (1980).

Winn, D. D., "Flow Studies of an Ideal Fluid Impinging on a Void," M.S. Thesis, Department of Mechanical Engineering, University of Illinois (1977).

Hubbard, A. L., "Theoretical Study of a Two-Dimensional Virtual Impactor," M.S. Thesis, Department of Civil Engineering, University of Illinois (1980).

Forney, L. J. and Ravenhall, D. G., "Development of an Aerosol Size Classifier," Department of Energy Progress Report COO-4319-1, January 1978.

Forney, L. J. and Ravenhall, D. G., "Development of an Aerosol Size Classifier: A Two-Dimensional Self-Similiar Virtual Impactor," Department of Energy Progress Report COO-4319-4, January 1979.

Forney, L. J. and Ravenhall, D. G., "Two-Dimensional Virtual Impactors", Department of Energy Final Report COO-4319-6, December 1980.

Forney, L. J., Ravenhall, D. G. and Lee, S. S., "Experimental and Theoretical Study of a Virtual Impactor," Environmental Science and Technology (submitted for publication, 1980).

Ravenhall, D. G., Forney, L. J. and Hubbard, A. L., "Theoretical Study of a Two-Dimensional Virtual Impactor," Journal of Colloid Interface Science (submitted for publication, 1980).

Forney, L. J. and Giz, Z. G., "Slow Chemical Reactions in Power Plant Plumes: Application to Sulfates," Atmospheric Environment 14, 533 (1980).

Forney, L. J. and Giz, Z. G., "Fast Reversible Reactions in Power Plant Plumes: Application to the Nitrogen Dioxide Photolytic Cycle," Atmospheric Environment, 15 (1981).

Forney, L. J. and Heffner, D. A., "Slow Second Order Reactions in Power Plant Plumes", Environmental Science and Technology (in preparation, 1980).

IV. APPENDIX

1. THESIS

THEORETICAL STUDY OF PARTICLE MOTION IN AN IDEAL FLUID VIRTUAL IMPACTOR WITH SECONDARY FLOW

BY

ALLEN JONES HUBBARD

Sc.B., Brown University, 1978

THESIS

Submitted in partial fulfillment of the requirements
for the degree of Master of Science
in Environmental Engineering in Civil Engineering
in the Graduate College of the
University of Illinois at Urbana-Champaign, 1980

Urbana, Illinois

ACKNOWLEDGMENT

The author would like to thank Professors D.G. Ravenhall and L.J. Forney for their guidance on this thesis. Funding for the work was provided by a Department of Energy grant EE-77-S-02-4319.

PREFACE

Flow properties of parallel-throat virtual particle impactors, assuming an ideal fluid in two dimensions, are derived from conformal mapping techniques. The aerosol impinges on a rectangular void. Fluid deflecting plates are inclined at arbitrary angles to the incoming jet. Numerical simulation of particle trajectories and the inclusion of variable secondary flows into the void augment the scope of the study. Particle sizing capabilities for various theoretically admissible instrument geometries are explored. Useful ranges of normalized void width ratio h/w and normalized jet-to-plate spacing s/w, at fluid deflecting plate angles $\beta = 70°, 90°$, define the geometry. Numerical results demonstrate that internal particle losses are reduced as the void width is increased.

TABLE OF CONTENTS

LIST OF FIGURES

1. INTRODUCTION

The presence of micron size particles in the atmosphere implies a developing technology concerned with understanding the aerodynamic properties of fine suspensions. These small particles, typically on the order of 3 μm in diameter, represent a potential health hazard, as they may penetrate into the innermost regions of the lungs. Also, the light-scattering abilities of small particles cause hazy ambient conditions which reduce visibility.

Commonly, multistage cascade impactors or hi-volume samplers are used to sample airborne particulate matter. Problems associated with these devices have stimulated additional research. Single stage particle impactors are commonly used today. Both virtual and inertial impactors find application in particle sizing. A particle-laden fluid stream approaches a collection surface; a sharp turn draws the fluid away from the region where the heavier particles impact. Small particles also exit the device, so that the impactor may classify aerosols with regard to their aerodynamic particle size. The advantage of the virtual impactor over the solid-plate (i.e., inertial) impactor is the elimination of particle-surface interactions. Large particles cross into a stagnant region below the collecting plate, leaving a void space at the outside of the turning fluid. A secondary flow, drawing a fraction of the incident fluid into the void, also functions to allow large particles to leave the flow field quickly and efficiently.

A fundamental understanding of the nature of the flow field at every point can be derived from solving the Laplace equation of potential fluid flow. Davies and Aylward [1] were the first to involve conformal mapping techniques in deriving these closed-form analytical expressions for ideal fluid flow. Their solution described a two-dimensional jet impinging normally on a solid plate. Ravenhall and Forney ([4], [6], and [7]) have adapted potential flow theory for virtual impactors. The focus of this research is a parallel throat virtual impactor, including secondary flow, with arbitrary geometry. Because the jet Reynolds numbers are typically large ($> 10^3$), an ideal fluid solution presents a good approximation of the flow pattern.

The potential flow theory of Section 2 develops the equations needed to connect the complex planes which map the fluid flow. A discussion of the numerical procedures involved in constructing the figures is contained in Section 3, while Section 4 describes the significance of such curves. Section 5 concludes this work.

2. THEORY

2.1 Ideal Fluid Transformations

The z-plane of Figure 1 is a representation of the desired flow pattern for the impactor. A line of symmetry, on which lies point F, divides the full device into two conceptually convenient halves. In fact, point F represents the bifurcation point of the fluid flowing down the pipe with outer wall AB. The void space is defined by h, the perpendicular distance from the line of symmetry to the leading edge of the deflecting plate, point E. The distance s, perpendicular from the leading edge E to the end of the throat at point B, is the jet-to-plate spacing. The width of the entering jet, the distance w, is the scaling factor for the device geometry. That is, the normalized dimensionless ratios h/w and s/w characterize the system geometry. The fluid deflecting plate, represented by ED and guiding the emerging jet, may be inclined at any angle β relative to the parallel walls of the entering pipe.

A fraction of the incident flow Q is to be bled off into the void space. Thus, in the W-plane, the distance fQ represents the bled fraction of the total incoming flow. Boundary conditions for the outermost portion of the secondary flow are that the fluid starts at the bifurcation point F and continues into the void space, ultimately becoming parallel to the plate ED at the point K. At the leading edge the plate must be infinitely thin, so that the fluid arriving there can separate into two parts,

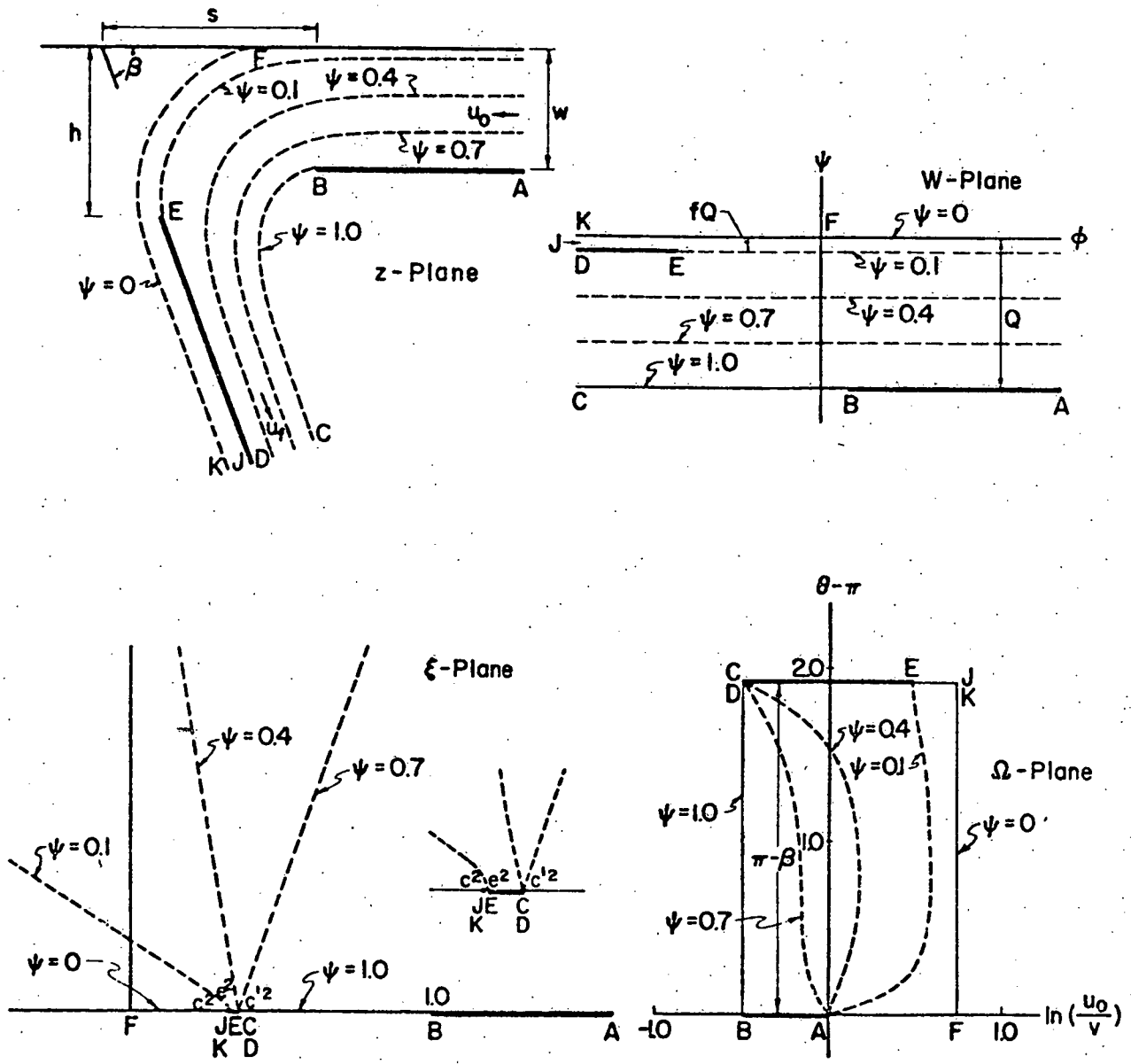

Figure 1. Transformation Planes

one going to J in the bleed flow, and one going to D in the emerging jet. Also, both FK and BC are free streamlines. The entering velocity is u_o, and u_f is the exiting fluid velocity.

The potential flow solution to the problem involves a complex potential W, where

$$\frac{dW}{dz} = V^* \quad , \tag{2.1}$$

and V* is the complex conjugate of the fluid velocity. Because the device is two-dimensional, the analysis depends on the two Cartesian coordinates (x, y). For any analytic function W of the complex argument (x + iy) = z, both the real and imaginary parts satisfy

$$\nabla^2 W = 0 \quad , \tag{2.2}$$

which is Laplace's differential equation. From

$$W(x + iy) = \Phi(x, y) + i\,\psi(x,y) \tag{2.3}$$

it can be shown that

$$\frac{\partial W}{\partial y} = i\,\frac{\partial W}{\partial x} \quad . \tag{2.4}$$

Since

$$\frac{\partial W}{\partial x} = \frac{\partial \Phi}{\partial x} + i\,\frac{\partial \psi}{\partial x} \tag{2.5a}$$

and

$$\frac{\partial W}{\partial y} = \frac{\partial \Phi}{\partial y} + i\,\frac{\partial \psi}{\partial y} \quad , \tag{2.5b}$$

the Cauchy-Riemann equations result:

$$\frac{\partial \Phi}{\partial y} = -\frac{\partial \psi}{\partial x} \tag{2.6a}$$

$$\frac{\partial \Phi}{\partial x} = \frac{\partial \psi}{\partial y} \quad . \tag{2.6b}$$

W(z) is the stream function, with Φ being the potential function. From Equations (2.6),

$$v_x = \frac{\partial \psi}{\partial y} \tag{2.7a}$$

$$v_y = - \frac{\partial \psi}{\partial x} \quad . \tag{2.7b}$$

As a consequence of satisfying the Cauchy-Riemann equations, the curves Φ = constant and ψ = constant are everywhere orthogonal in the flow field. Hence, fluid velocities are perpendicular to the lines of constant potential, implying that ψ = constant is a streamline, upon which velocity is constant. In this way, one may also conceive of ψ as a stream function.

Conformal mapping facilitates solving Laplace's equation in a particular region by transforming that region into the unit circle or an upper half-plane. Once the solution is found in the new location, subsequent transformation back to the original region results in the desired solution.

Referring to Figure 1, the W-plane is an infinite strip of width Q, where Q is the volumetric flow rate. The deflecting plate ED is horizontal, at a distance fQ below the real axis. Therefore, the horizontal plate AB must lie a distance Q below the real axis. Point F is simply chosen as the origin.

Beyond the point B, the emerging jet is bounded by the free streamline BC; similarly, subsequent to point F, the free streamline FK bounds the flow. One can envision another complex

plane in which straight lines represent the boundaries to the flow. The introduction of the Kirchhoff variable $\Omega = \log (u_o \, dz/dW)$ leads to the Ω-plane, wherein $Im\ \Omega = \theta - \pi$, where θ is the change in angle of the fluid velocity. The closed rectangular area in this diagram represents the flow boundaries of the device. The quantity u_o is the velocity of the incident jet, far enough upstream of the throat to be constant across the cross section. The fluid, travelling parallel to AB, does not change angle until it reaches the throat. Thus, AB is on the real axis in the Ω-plane. From B to C the fluid follows a free streamline, whereon the magnitude of velocity is constant, but angle is constantly changing; therefore, BC lies vertically. In a similar fashion, FK is a vertical line, whereas DE and EJ are horizontal lines in the Ω-plane. The distance from B to CD (or JK to F) is determined by the magnitude of β, the angle of the deflecting plate relative to the incoming fluid velocity vector. Although the locations of the sides JK-F and CD-B are not prescribable, they define the magnitude of the fluid velocity at the free streamlines.

A subsidiary variable ξ connects the complex variables W and Ω. The region between the boundaries in the W-plane, as well as the interior of the rectangle in the Ω-plane, are mapped onto the upper half-plane of the ξ-plane by a straightforward application of the Schwartz-Christophel theorem. The transformation includes all of the salient features of the Ω and W planes. Point F is taken to be the origin, and B is chosen to be at 1

on the real axis. The points JK, E, and CD also lie on this axis, at c^2, e^2, and c'^2, respectively. This notation is consistent with earlier work by Ravenhall [3]. These ξ-plane parameters have values which are consistent with the dimensions of the actual device. By inspection, $0 < c^2 < e^2 < c'^2 < 1$.

From the Schwartz-Christophel theorem, the differential relationship between W and ξ is

$$\frac{dW}{d\xi} \propto (\xi - c'^2)^{-1} (\xi - e^2)(\xi - c^2)^{-1} . \tag{2.8}$$

Integration of this expression gives

$$W = \frac{Q}{\pi} \left[\frac{c'^2 - e^2}{c'^2 - c^2} \log \frac{c'^2 - \xi}{c'^2} + \frac{e^2 - c^2}{c'^2 - c^2} \log \frac{c^2 - \xi}{c^2} \right], \tag{2.9}$$

apart from constants which are found from the position of F and the width Q in the W-plane.

To ensure that f describes the bleed fraction of the total incoming flow, consider the flow field in the W-plane. Here, the flow must separate into two parts about the stagnation point E; a fraction f continues to infinity at JK, while the remainder goes to CD at infinity. The ξ-plane reinforces this condition; the points c^2 and c'^2 represent sinks of relative magnitude f and (1 - f), with e^2 as the intermediate stagnation point. It follows that

$$e^2 = fc'^2 + (1 - f)\, c^2 \tag{2.10}$$

or

$$f = \frac{e^2 - c^2}{c'^2 - c^2} . \tag{2.11}$$

Using the latter expression, W and ξ are related by

$$\frac{\pi W}{Q} = f \log \frac{c^2 - \xi}{c^2} + (1 - f) \log \frac{c'^2 - \xi}{c'^2} \quad . \tag{2.12}$$

Clearly, there is no analytical solution for $\xi \neq 0$ in terms of W and constants; hence, numerical inversion must be employed.

A second Schwartz-Christophel transformation links Ω with ξ:

$$\frac{d\Omega}{d\xi} \propto (\xi - 1)^{-\frac{1}{2}} (\xi - c'^2)^{-\frac{1}{2}} (\xi - c^2)^{-\frac{1}{2}} \quad . \tag{2.13}$$

The boundary condition on the flow is that the exit fluid velocity is u_f; integration of the last equation reveals

$$\Omega(\xi) = \log \left(\frac{u_f}{u_o}\right) \{F(\phi \backslash \alpha)/F(\chi \backslash \alpha) - 1\} \quad . \tag{2.14}$$

F represents an incomplete elliptic integral of the first kind. The modular angle α of this function is given by

$$\cos \alpha = \left[\frac{c^2(1 - c'^2)}{(1 - c^2)\, c'^2}\right]^{\frac{1}{2}} \quad , \tag{2.15}$$

the argument χ of the constant factor involving F by

$$\tan \chi = \left[\frac{c'^2}{1 - c'^2}\right]^{\frac{1}{2}} \quad , \tag{2.16}$$

and the ξ dependence of the argument ϕ by

$$\tan \phi = \left[\frac{c'^2}{1 - c'^2} \frac{\xi - 1}{\xi}\right]^{\frac{1}{2}} \quad , \tag{2.17}$$

as shown by Ravenhall [4].

Knowing the height $\pi - \beta$ of the rectangle in the Ω-plane, the ratio $R = u_f/u_o$ can be determined from Equation (2.14):

$$\ln R = (\pi - \beta)\ F(X \setminus \alpha)/K'(\alpha) \ , \tag{2.18}$$

where $K'(\alpha)$ is the complete elliptic integral

$$K'(\alpha) = F([\pi - \beta] \setminus [\pi - \beta - \alpha]) \ . \tag{2.19}$$

Numerical integration relates the $W(\xi)$ and $\Omega(\xi)$ transformations to the z-plane. In this way, assumed values of c^2 and c'^2 determine the shape of the physical device representation. Any prescribable contour in either the W or the ξ plane will theoretically permit computation of distances in the z-plane. From the definition of the Kirchhoff variable,

$$\frac{dz}{dW} = \frac{1}{u_o}\, e^{\Omega} \ . \tag{2.20}$$

Distances in z may be found by either

$$z(P_2) - z(P_1) = \frac{1}{u_o} \int_{W(P_1)}^{W(P_2)} e^{\Omega(\xi[W])}\, dW \tag{2.21}$$

or

$$z(P_2) - z(P_1) = \frac{1}{u_o} \int_{\xi(P_1)}^{\xi(P_2)} e^{\Omega(\xi)}\, \frac{dW}{d\xi}\, d\xi \ . \tag{2.22}$$

Although Equations (2.12) and (2.14) appear to make evaluation of Equation (2.22) easier (since numerical inversion of Equation (2.12) is required for evaluating the other integral), it turns out that the W-plane contours are better suited for numerical integration. In the ξ-plane, the flow pattern converges in the

region of the sinks at c^2 and c'^2 on the real axis. If P_1 and P_2 are in this area, relatively small intervals are needed to perform the integration, an effort that is wasted elsewhere. Such a time-consuming approach was abandoned in favor of a numerical scheme to invert the $W(\xi)$ relation of Equation (2.12). D.G. Ravenhall explains the computational details more fully in a study of a related device contained in Reference [3].

Assuming values for the ξ-plane parameters c^2 and c'^2, the physical dimensions of the device are obtained from judicious choices of P_1 and P_2 in Equation (2.21). The computed distance between B and E leads to determining the void width h, since

$$z(B) - z(E) = (h - w) + i\,d\ , \tag{2.23}$$

for some imaginary distance d. Also, given a value for the plate angle β, the value of s is obtained from

$$s = \frac{h}{\tan\,\beta} + d\ . \tag{2.24}$$

The dimensionless parameters s/w and h/w describe the allowable device geometries. As there is a theoretical limit on the magnitude of h/w, the investigation of flow field properties and device characteristics is only numerically pursued for a range of permissible geometries. A typical set of streamlines is depicted in Figure 2.

2.2 Particle Trajectories

Stokes' Law relates effective particle mass m to fluid velocity $\underline{v}_f$ and the particle's own velocity $\underline{v}$ in the vector

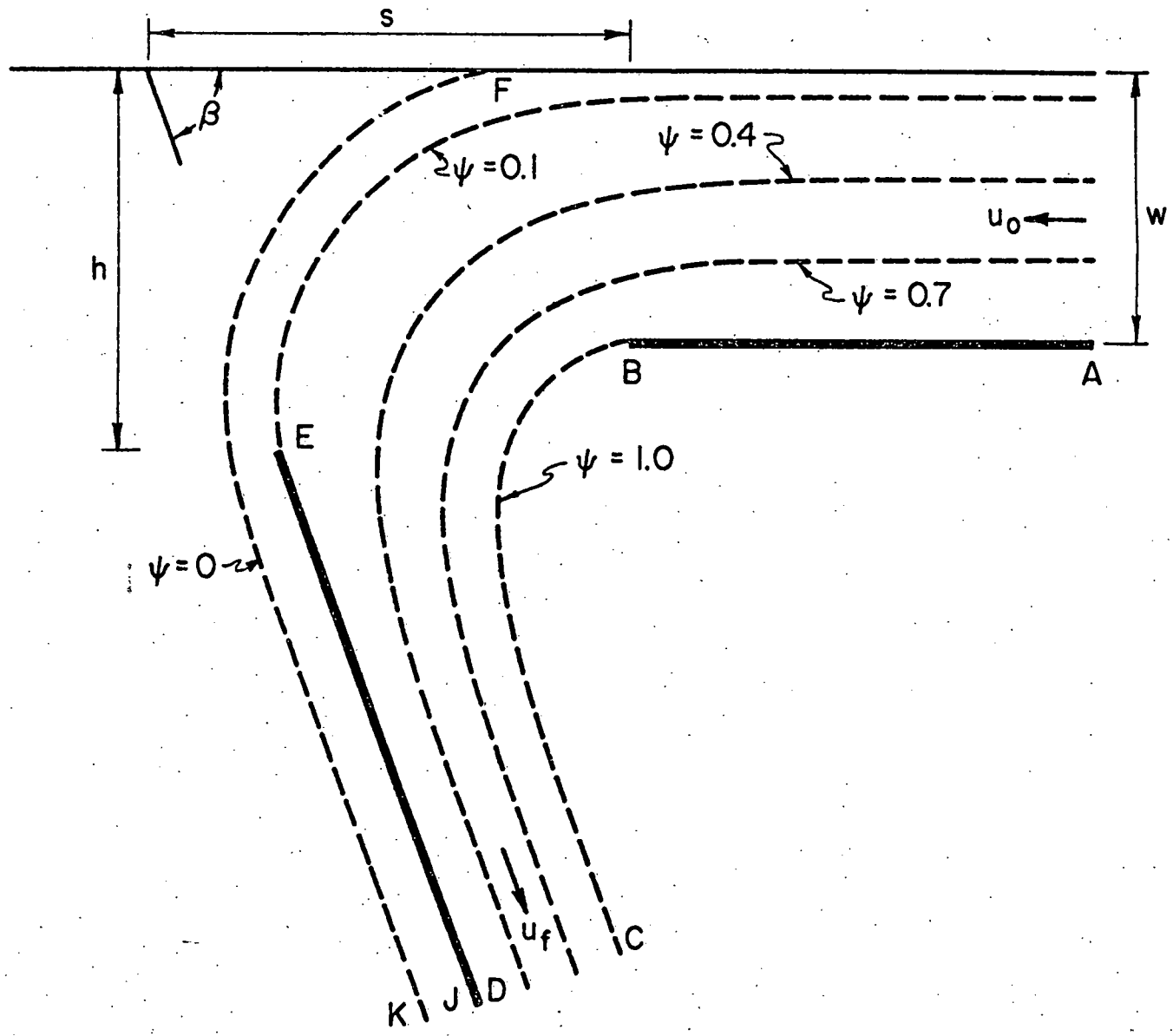

Figure 2. Ideal Fluid Streamlines

differential equation of motion

$$m \frac{d\underline{v}}{dt} = K (\underline{v}_f - \underline{v}) \quad , \tag{2.25}$$

where K is a proportionality constant. This equation governs the motion of a particle initially moving with fluid streamlines in the entering flow. Particle trajectories may extend into the void space, intercept the plate ED, or continue with the exiting jet. Exactly where a particle will go depends on its starting position y_o upstream of point B (in the W-plane, $0 > y_o > -w$), the constants K and m, and the fluid flow pattern. A dimensionless relaxation time τ characterizes particle motion. In the scaling units u_o and w,

$$\tau = \frac{u_o t}{w} \quad , \tag{2.26}$$

so that the normalized equations tracing the particle's trajectory are

$$\frac{d}{d\tau} \left(\frac{\underline{x}}{w} \right) = \frac{\underline{v}}{u_o} \tag{2.27}$$

and

$$\frac{d}{d\tau} \left(\frac{\underline{v}}{u_o} \right) = \left(\frac{wK}{mu_o} \right) \left(\frac{\underline{v}_f}{u_o} - \frac{\underline{v}}{u_o} \right) \quad . \tag{2.28}$$

This last equation clearly demonstrates that the Stokes number $\psi = \frac{mu_o}{wK}$ characterizes particle motion in flow fields. The simplest assumption is that of spherical particles, wherein $m = \frac{4}{3} \pi a^3 \rho$, if ρ is the density and a is the radius. Also, $K = 6\pi\mu a$, where μ is the fluid viscosity. By substitution, the

Stokes number may now be expressed as

$$\psi = \frac{2}{9} a^2 \rho \, u_o / w\mu \quad . \tag{2.29}$$

However, it is more expedient to have a dimensionless parameter proportional to particle radius. Therefore, one defines the quantity

$$\psi^{\frac{1}{2}} = a\left(\frac{2}{9} \rho u_o / w\mu\right)^{\frac{1}{2}} \quad . \tag{2.30}$$

Particle trajectories are determined from the numerical integration of Equation (2.28). The necessary information is obtained from the previously computed fluid properties for a particular device geometry. Interpolation between tabulated velocities yields $\underline{v}_f$ at any point in the flow field. Assumed values of starting position and Stokes number, together with the integration of Equation (2.28), determine particle destinations. Because of its mass (and so its momentum), a particle may not remain on fluid streamlines as the jet turns the corner downstream of point B. Only the small particles will leave with the exiting jet. Thus, it is useful to define two fractionating efficiencies, one for particles plunging into the void, and the other for those particles collected on the surface of the plate ED. E_v is the fraction of particles of a certain size which enter the void, numerically equal to the value of $|y_o|/w$ for which the trajectory hits the leading edge of the plate. All particles passing upstream of point E, then, are collected by the void. Note that any particle starting with $|y_o|/w \leq f$ will surely go into the void, since particles cannot get out of the

bleed flow for any value of $\psi^{1/2}$. Therefore, the vertical axis intercept must be numerically equal to the bleed fraction f.

The fraction of incoming particles which are collected by either the void or the collecting plate is E_T. The numerical value of $|y_o|/w$ for a trajectory which asymptotically intercepts the plate, for a given particle size, is the quantity E_T. This total efficiency manifests the ability of such a device to remove particles of a certain size from a fluid stream.

Implicit in the calculation of efficiencies are the assumptions of a uniform density of particles across a starting section of the incoming jet and of a monotonic and increasing functional relation between y_o and $\psi^{1/2}$. Indeed, each virtual impactor configuration here investigated exhibited this behavior. A further assumption was that the particles began with uniform velocities, so that they would initially all travel with the fluid. This condition necessitated numerical injection of the particles sufficiently upstream of the throat at B to reach a cross section of uniform fluid velocity. Several significant particle trajectories in a typical flow scheme are illustrated in Figure 3. Trajectory T_1 enters the void space, T_2 hits the leading edge of the plate, while T_3 asymptotically intercepts the plate far downstream of the primary impaction region. The three particles are the same size ($\psi^{1/2} = .45$), but their starting positions were chosen to illustrate the variety of impactor particle paths.

A loss factor L, where

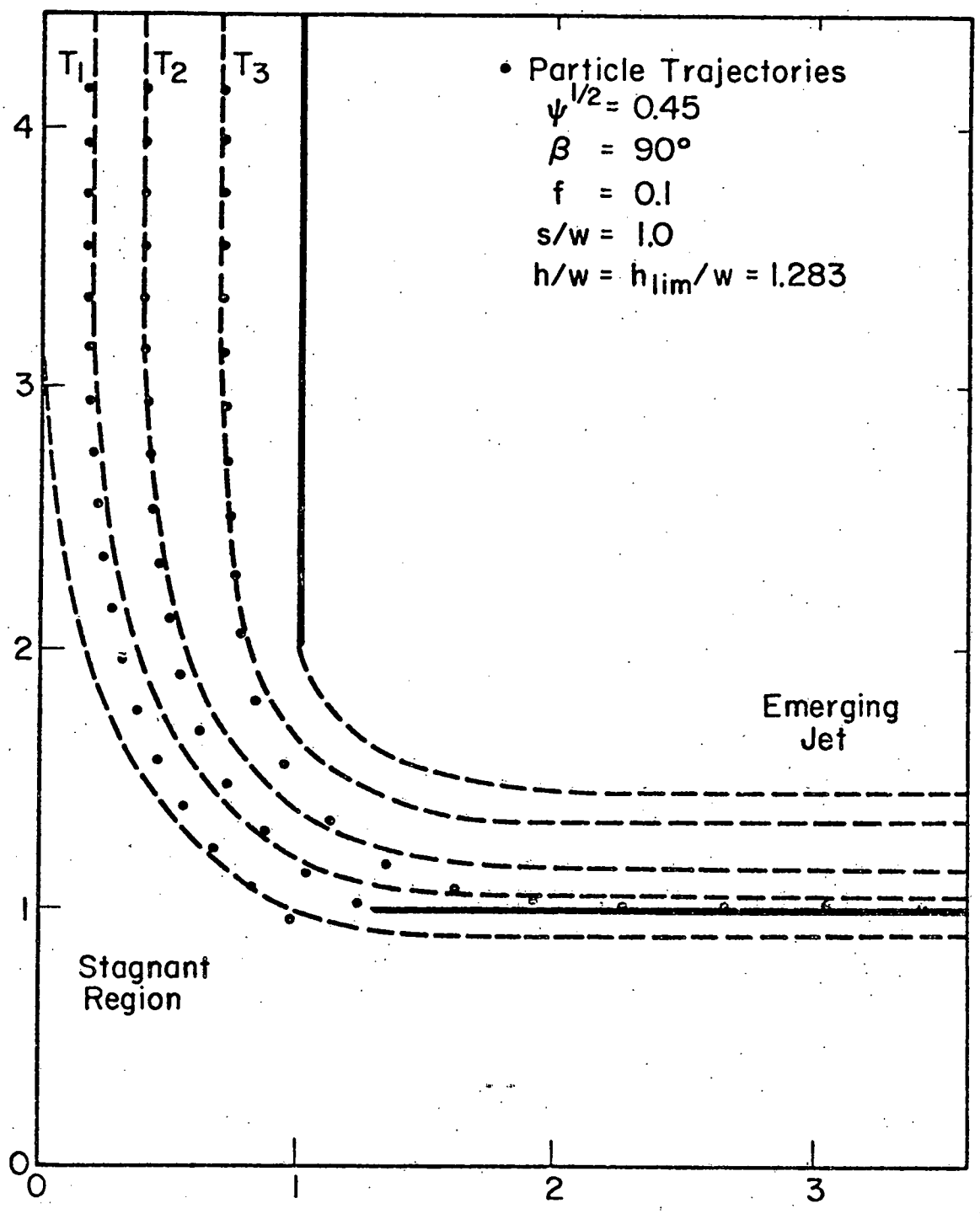

Figure 3. Representative Particle Trajectories

$$L = E_T - E_v \quad , \tag{2.31}$$

represents the fraction of particles of a given size which are collected on the plate. Experimentally, such particles are elusive, and it is difficult to evaluate the performance of the device. The locus of points L evaluated over all $\psi^{\frac{1}{2}}$ is a loss spectrum, the δ-shaped region of the typical efficiencies plot of Figure 4. The maximum efficiency of the device for any size particle is given by the maximum value of this curve, L_m. This loss spectrum maximum is also equivalent to the difference $(E_T - E_v)$, when $E_T = 1.0$.

Another useful quantity is the area under the loss spectrum, A. Integration yields the total number of particles lost to the plate; for a variable $\theta = \psi^{\frac{1}{2}}$,

$$A = \int_0^\infty L(\theta)\, d\theta \quad . \tag{2.32}$$

As the void width increases to its theoretical maximum, the area under the loss spectrum decreases. Figure 5 displays this property of loss spectra.

For an impactor, particle discrimination capabilities may be estimated from a "cutoff" value of $\psi^{\frac{1}{2}}$, proportional to that size particle for which the device has a removal efficiency of .50. That is, $\psi_{50}^{\frac{1}{2}}$ for a particular device implies that larger particles are captured, while smaller particles escape in the exit jet. The accuracy of this last assumption depends on how steep the total efficiency curve is in the region about $\psi_{50}^{\frac{1}{2}}$. So that one may effectively compare efficiency curves for a

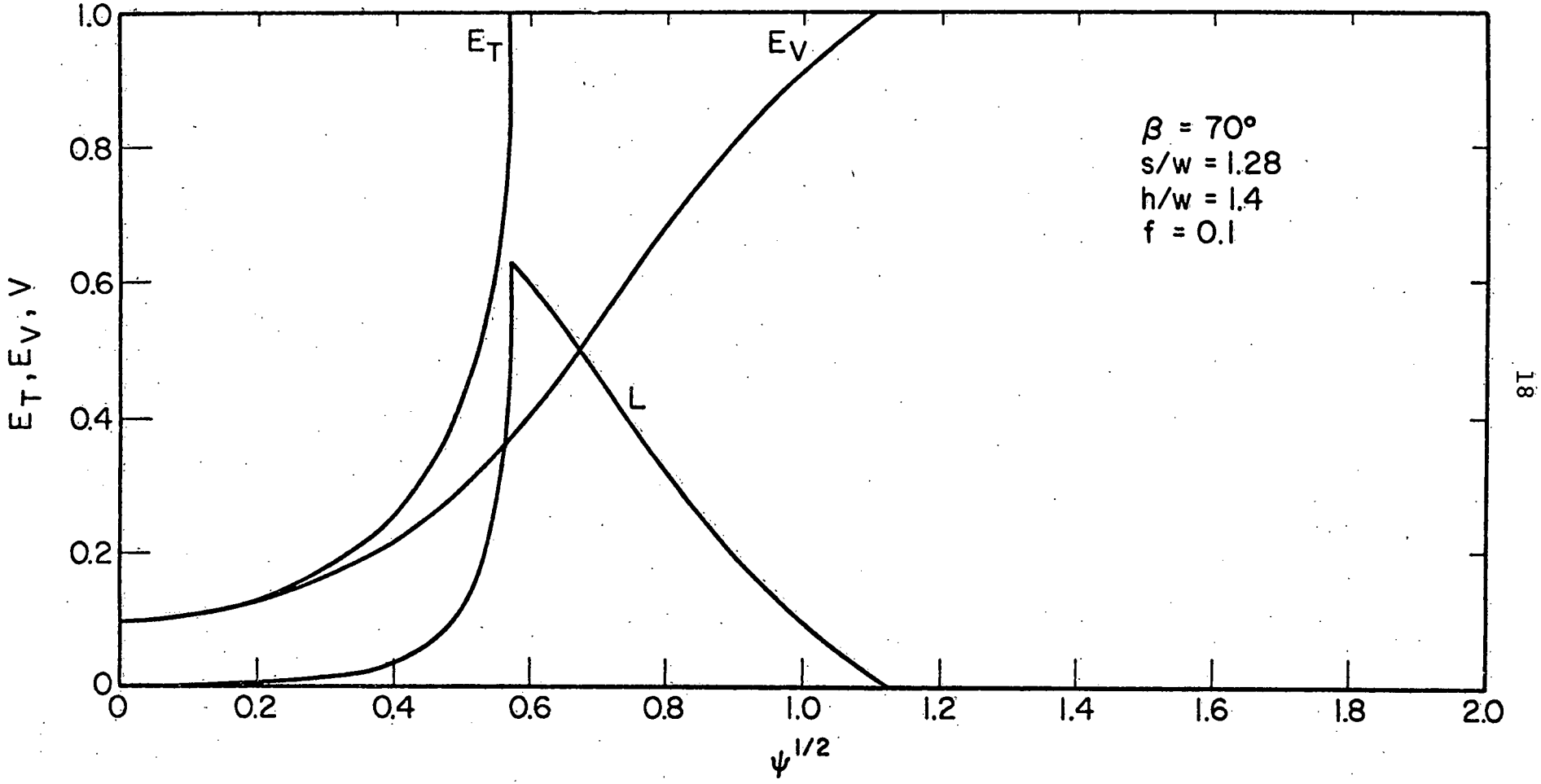

Figure 4. Total and Void Efficiency Curves, Loss Spectrum, A = 0.1808, S = 0.541, L_m = 0.627, $\psi_{50}^{\frac{1}{2}}$ = 0.538

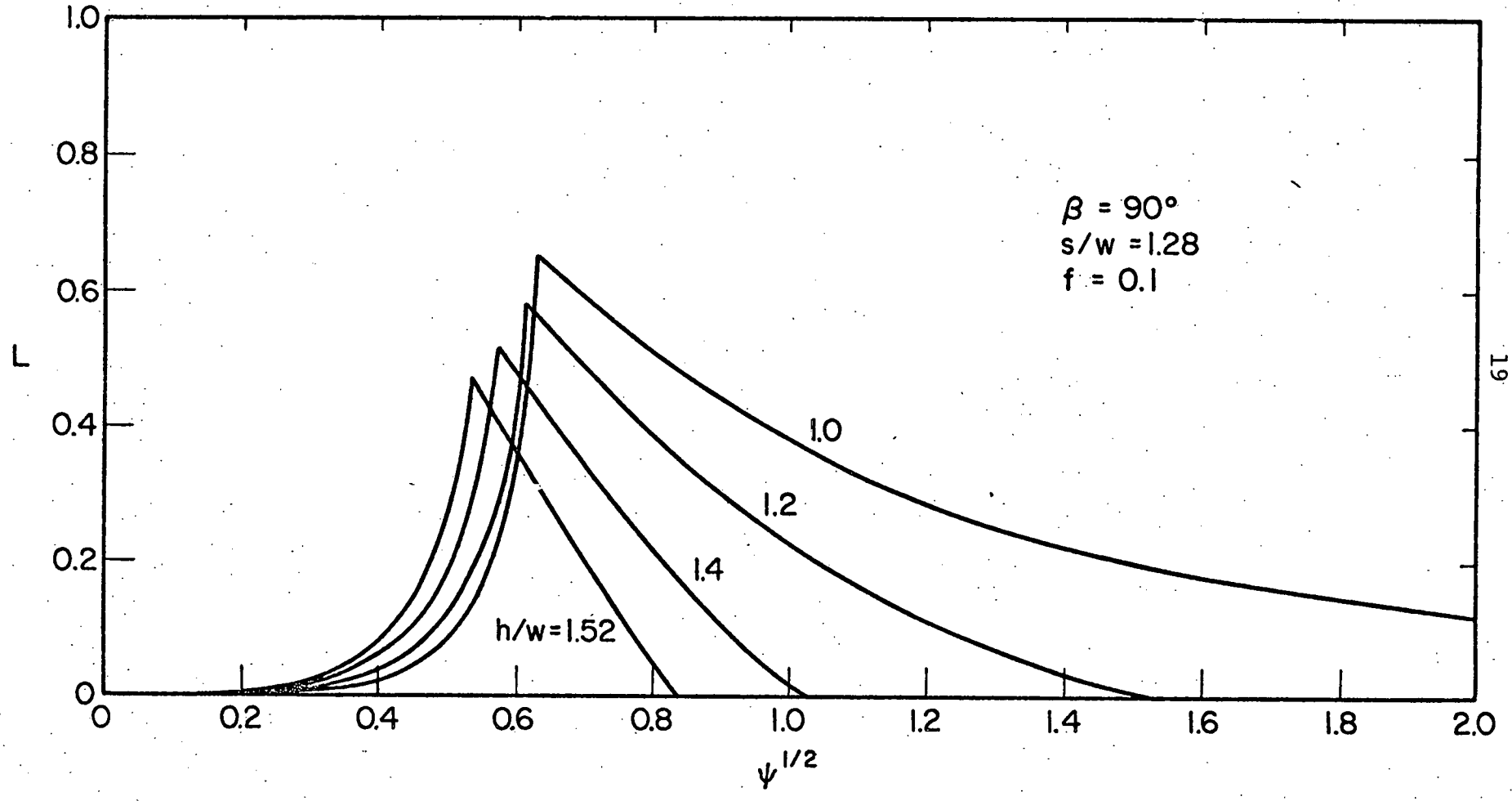

Figure 5. Comparative Loss Spectra

large range of particle diameters, a plot of efficiency as a function of log $\psi^{\frac{1}{2}}$ is required. Such a technique assures a uniformity of shape which would otherwise depend on particle size. Then it is the relative steepness of this type of curve that is significant. The slope is defined as

$$S = \frac{d(\log \psi^{\frac{1}{2}})}{dE} \quad , \tag{2.33}$$

which may be evaluated numerically from

$$S = \frac{\psi^{\frac{1}{2}}(.84)(1 - f) + f \quad - \psi^{\frac{1}{2}}(.16)(1 - f) + f}{(.68)(1 - f)\ \psi^{\frac{1}{2}}(.50)(1 - f) + f} \quad , \tag{2.34}$$

where S is the relative dispersion of Stokes parameters about $\psi_{50}^{\frac{1}{2}}$ for a particular efficiency curve. The fractionating capacity of an impactor is enhanced by maximizing the slope of its efficiency curve in this critical region about the cutoff particle diameter. Therefore, the quantity S must be minimized for optimal performance.

3. NUMERICAL PROCEDURES

The potential flow theory developed in Section 2 allows one to compute flow field properties for a range of device geometries. The jet-to-plate spacing, void opening, bleed fraction, and deflecting plate angle may all be varied, although not independently. To solve for any given quantity, it is necessary to specify two of the other three. For example, to calculate a particular void space, one might specify deflecting plate angle (β) and bleed fraction (f). Once these ratios are specified, it is sufficient to propose the ξ-plane parameters c^2 and c'^2, which imply the additional parameter e^2 of Equation (2.10). Because the point B is always at (1, 0) in ξ, evaluation of Equations (2.20) and (2.21) will now lead to computation of the void opening. The contour of integration is the straight line in W between the two trial points mapped from the ξ-plane to the W-plane. Once the distance from B to E is known, the void width h follows straightforwardly from trigonometry. The jet-to-plate spacing s also results from this latter computation. However, to determine a particular geometry, one must also specify s initially so that an iterative search may ensure that c^2 and c'^2 have the correct values for the desired device dimensions. Besides this latter check within the iterations, there are other means by which the procedure maintains self-consistency. Obviously, the salient features of the mappings must correspond to the physical system. Additionally, the procedure should necessarily yield a device in which the

s/w \ h/w	Min.	Max.
0.62	0.452	0.957
1.00	0.518	1.288
1.28	0.562	1.515

$\beta = 90°$

$f = 0.1$

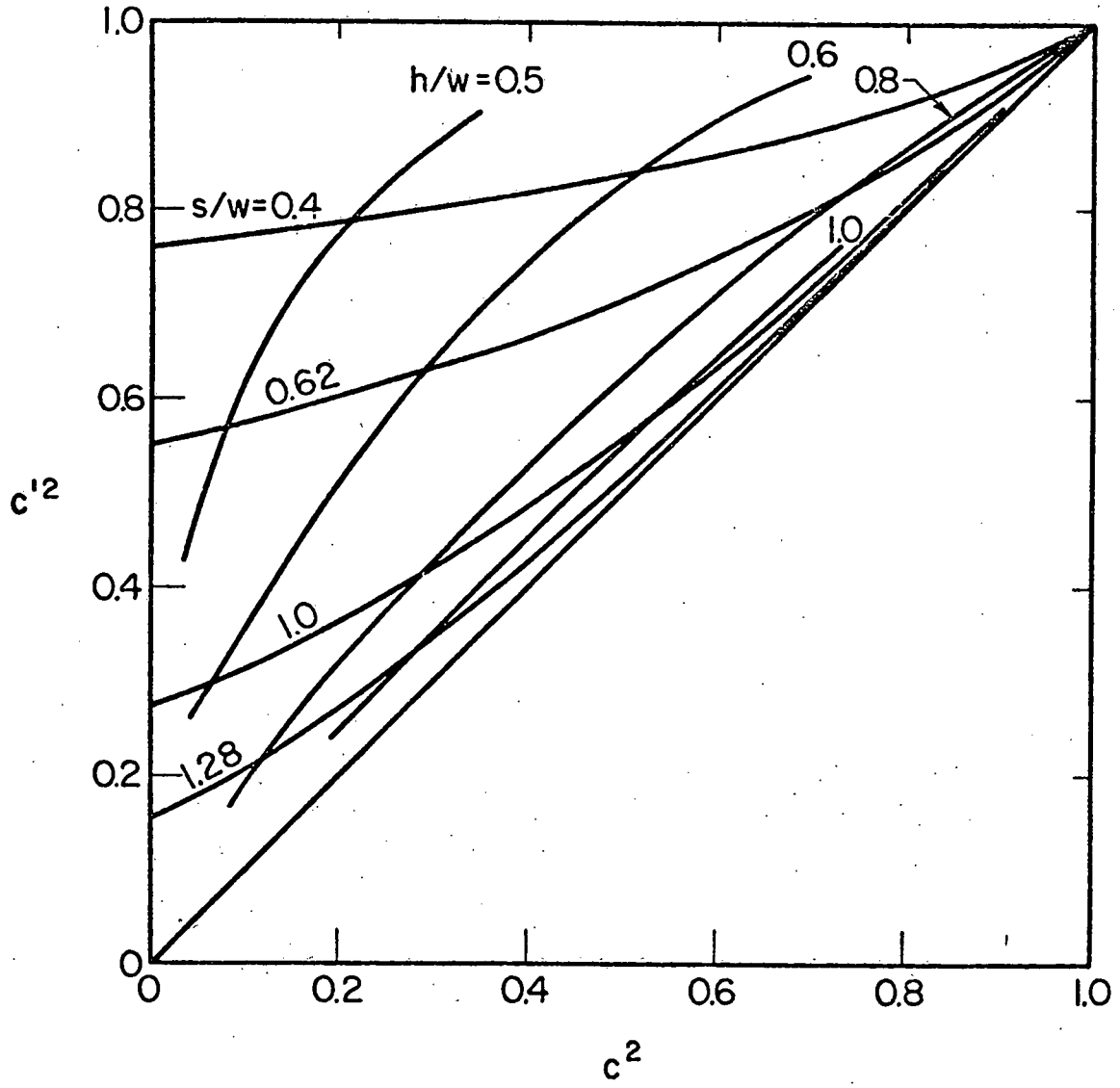

Figure 6. Computational Parameters c^2, c'^2

entrance has a width 1 (in units of w), and in which the emerging jet width (w_{em}) satisfies

$$w_{em} = w \left(\frac{u_o}{u_f} \right) , \tag{3.1}$$

which is required of an incompressible fluid. Ravenhall presents computational details, particularly regarding the evaluation of the elliptic integrals for Equations (2.14) and (2.18), in Reference [4].

As the parameters c^2 and c'^2 tend to 1, the value of h/w approaches a theoretical limit. A perusal of Figure 6 shows the numerical sensitivity of computing a limiting void width. In fact, calculations in this regime necessitate determining h/w and c'^2 from given values of s/w and c^2. The topology of the ξ-plane map requires $0 < c^2 < c'^2 < 1$, which restricts the allowed values of s/w and h/w to the region above $c^2 = c'^2$. Prior work by Forney, Ravenhall, and Winn [4] demonstrates that such a limit is consistent with the assumed mappings. A branch point in the analytical expressions for h/w exists at $c'^2 = 1$, so that larger values of h/w are not allowed. Forney, Ravenhall, and Winn [4] present some physical arguments for an upper bound on void width.

Also inherent in the ξ-plane configuration is a relation between the secondary flow fraction and the location of the sinks. The fraction f of the incoming flow is envisioned to arrive at point E (e^2 in ξ), while the remainder goes to CD

(c'^2 in ξ). The transformation planes of Figure 1, drawn for the case $\beta = 70°$, $s/w = 1.28$, $f = 0.1$, and $h/w = 1.4$, the same geometry for which the efficiency curves were drawn, illustrate a self-consistent set of streamlines. The stream function ψ varies between the values at the boundaries, 0 and 1.0. It is readily apparent that the bleed streamline, $\psi = 0.1$, always sinks at point E. Also, it is clear from the insert of the ξ-plane that

$$f = \frac{e^2 - c^2}{c'^2 - c^2} \quad , \tag{3.2}$$

or that E is f of the way from JK to CD.

The numerical sensitivity encountered as c^2 and c'^2 tended to 1 complicated the determination of h_{lim}/w. Increased numerical precision was required as the parameters approached 1 in the ξ-plane. But to have sufficient computational accuracy when the quantity $(1 - c^2)$ was small would have meant making the calculations in other regions needlessly time-consuming and expensive. As a result, values of h/w as $(1 - c^2)$ went to 0 became large, clearly above the correct limit. Careful observation of the consistent numerical behavior of h/w, plotted as a function of $(1 - c^2)$, revealed a tangential approach to a line intersecting h_{lim}/w on the ordinate. That is, for decreasing values of $(1 - c^2)$, h/w became linear before diverging numerically to approach the vertical axis more gradually as $(1 - c^2) \to 0$. Hence a graphical procedure for determining the limiting void width was adopted to circumvent this problem. Extrapolating a

plot of h/w as a function of $(1 - c^2)$ when the curve becomes linear determines h_{lim}/w. Figure 7 is a sample extrapolation for the case $\beta = 70°$, $s/w = 0.8$, $f = 0.1$. The vertical intercept defines the theoretical upper bound for a device of this geometry as 1.386.

The numerical construction of efficiency curves follows precisely the pattern developed in Section 4; one may either fix particle size and scan efficiencies, or the reverse. Since fluid streamlines are horizontal lines in the W-plane, a judicious choice for beginning trajectories is the right-hand side of this map (see Figure 1). Because the width of the strip is unity, the ordinate of an efficiency curve also represents particle starting position. In this way, one may specify a starting position in W (and so in the entering flow) and scan particle sizes, conceptually more realistic. In order to compute fluid velocities anywhere in the flow field, a systematic grid of information proved useful. Dividing the W-plane into equal strips under the imaginary axis, flow properties were computed along each "streamline" at intervals equal to the vertical increment. This scheme created a square mesh which followed fluid streamlines, so that in the z-plane, the grid actually lay in curvilinear coordinates. A third-order interpolation of information at the four closest mesh points determined the fluid velocity $\underline{v}_f$ for any point in the flow field. Because the particle's initial velocity was assumed to be equal to the local fluid velocity, it was necessary to begin the mesh suitably

ahead of the throat at B, so that the fluid velocities were nearly constant at the initial cross-section. And although the velocities were always within 1% of each other at the mesh origin, particles were inserted at the third grid point to ensure accurate computation of the derivatives in Equations (2.27) and (2.28).

As a means for effective comparison of device characteristics, the loss spectrum areas were normalized with respect to the unit area of an efficiency vs. Stokes' parameter graph. The unit square was a convenient quantity, especially for relating the parallel throat results to prior work on converging throat impactors. An analytical technique for determining areas seemed cumbersome and wasteful, since any numerical scheme would require systematic interpolation of the efficiency curves. Alternatively, a graphical procedure involving the use of a standard planimeter proved adequate for finding the area under the loss spectra.

The numerical procedures conveyed herein are conveniently self-checking. If the mappings (of Figure 1) produce a device representation of the intended configuration, then the solution is valid and meaningful.

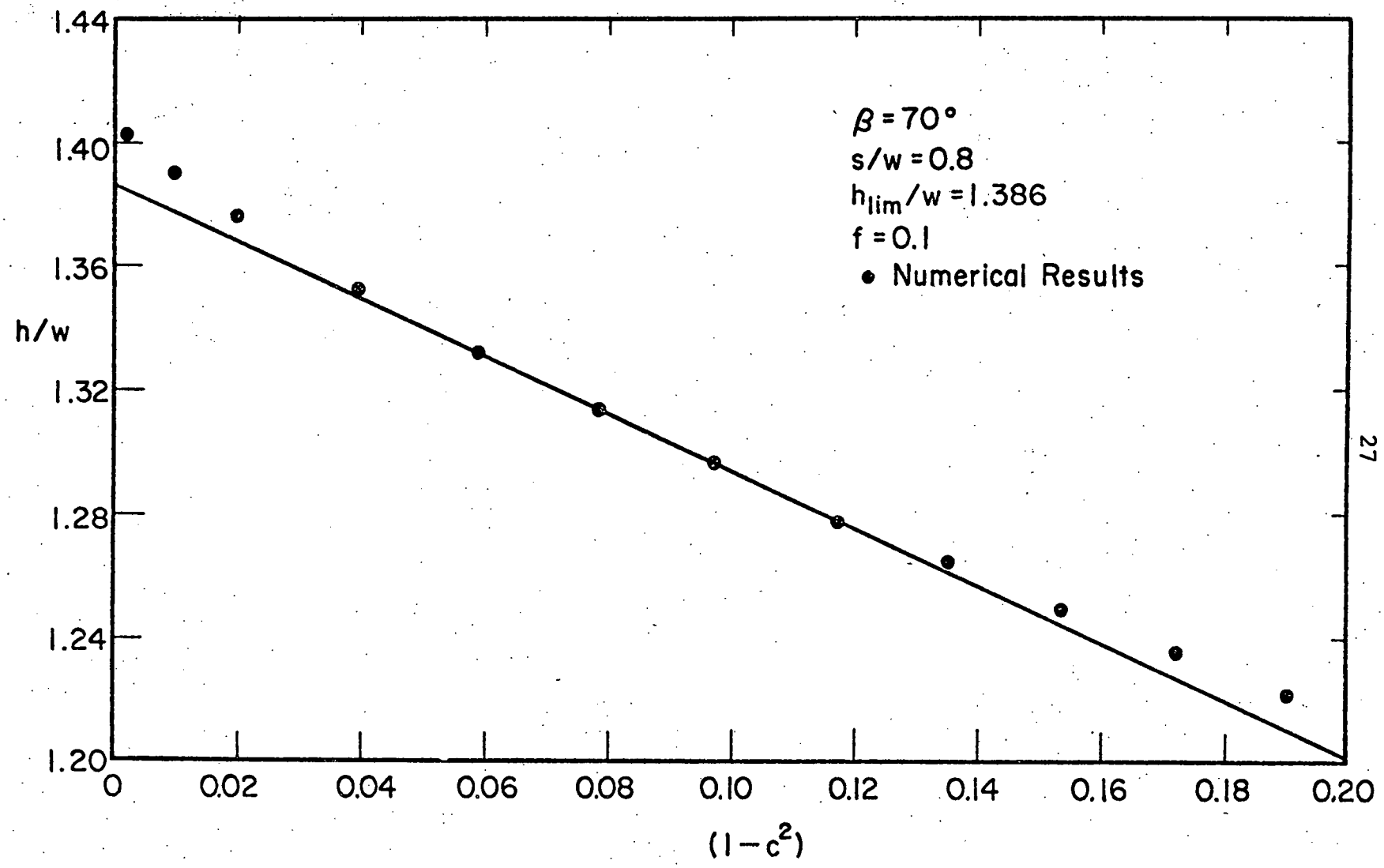

Figure 7. Graphical Procedure for Determining Limiting Void Width

4. DISCUSSION OF RESULTS

Particles of various sizes and starting positions may be numerically injected into a flow pattern and traced as they move according to Stokes' Law. The characteristic efficiencies of a parallel throat virtual impactor are shown in Figure 4. The curve E_v represents the efficiency of the void space for collecting approaching particles. The other curve represents the total efficiency of the device. The sigmoidal nature of E_v reflects the real device property of collecting some large particles in the void space.

There are two ways to interpret the efficiency curves. Each size of particle has certain associated efficiencies, depending on the initial throat position. Also, particles of various sizes may have a given efficiency. From Figure 4, any point above or to the left of E_T represents a particle lost to the main stream exit; any point below or to the right of E_v depicts a particle caught in the void space. Then the region between the curves E_T and E_v accounts for the particles which impact on the deflecting plate. E_T and E_v themselves represent the limits of particle collection on the plate. A point just to the left of E_T exits with the jet, while its neighbor on E_T asymptotically approaches the plate far downstream. Similarly, a point on E_v represents a particle which intercepts the leading edge of the plate, while the next larger particle (i.e., higher $\psi^{\frac{1}{2}}$) continues into the void space. The trajectories T_2 and T_3 of Figure 3 illustrate these limiting cases. Three particles

of $\psi^{\frac{1}{2}} = 0.45$ were placed along a cross section far upstream of the impaction plate, and their representative trajectories demonstrate where particles may go in the device.

The inherent flexibility of the theory of Section 2 allows one to rapidly explore various device configurations for flow field properties. Figures 8, 9, 10, and 11 relate jet-to-plate spacing, plate angle, and bleed fraction to limiting void space. E.W. Cannon experimentally explored s/w and f as functions of h_{lim}/w. Low values of s/w and small bleed flows were troublesome in the laboratory, and the theoretical correlation in these regions is fair. However, over much of the range of interest, agreement is good. The secondary flow data in particular are consistent with the theory. The limiting void width increases with both f and s/w. Figure 10, a plot of h_{lim}/w as a function of β, suggests that the theoretically admissible void space increases with decreasing plate angle, given a particular f and s/w. This figure clearly reiterates that for a given β, the limiting void width increases with increasing s/w.

As demonstrated in Figure 5, the size of the loss spectrum decreases with increasing void width. This reduction in area is also reflected in Figures 12 and 13. On the other hand, Figures 14 and 15 imply that reducing h/w would benefit a design, since a small value of S promotes effective particle sizing. The parameters S and $\psi_{50}^{\frac{1}{2}}$ (the efficiency steepness and particle cutoff value) are both computed from E_T, the total efficiency curve. Optimization of device geometry would involve

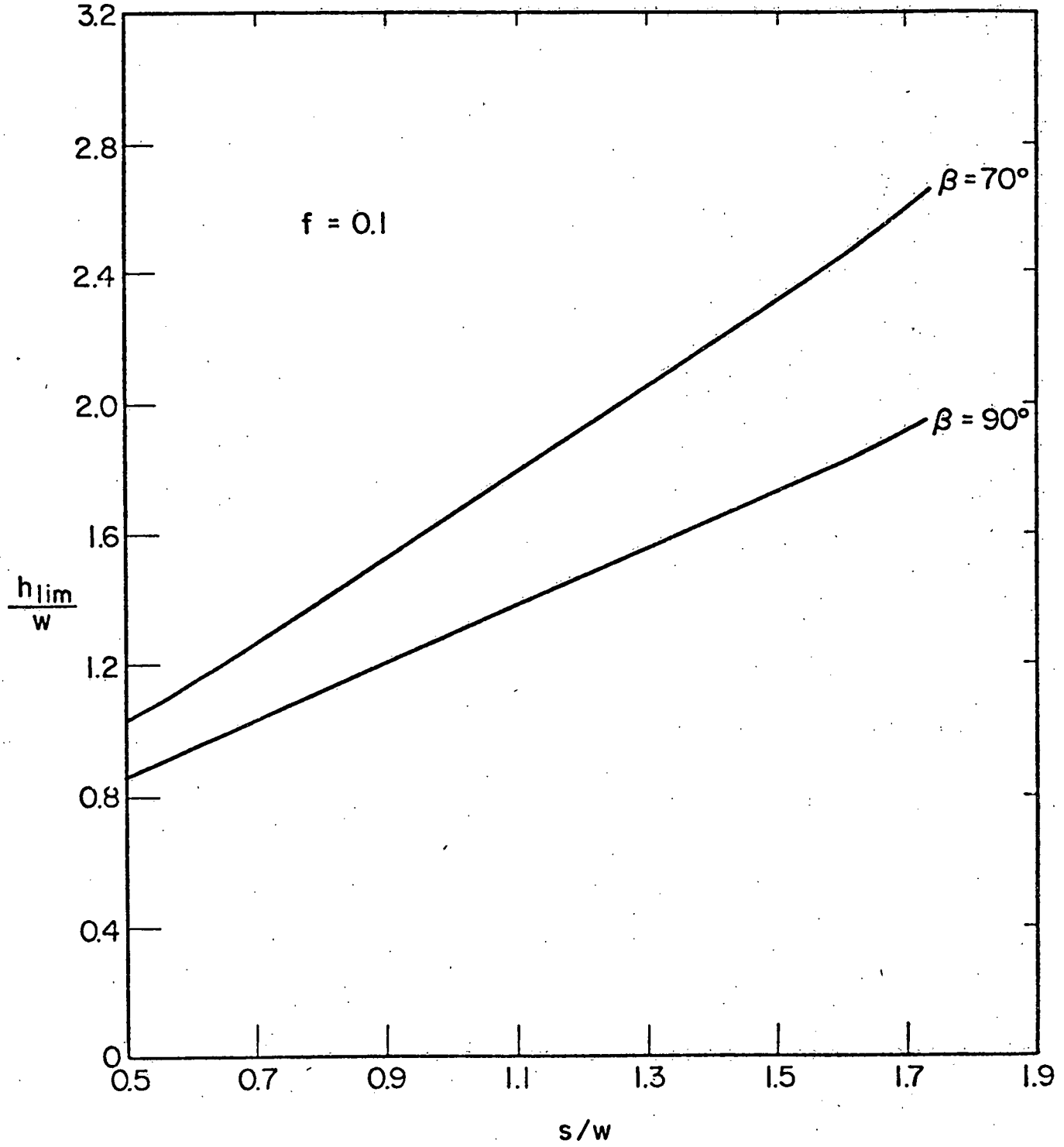

Figure 8. Jet-to-Plate Spacing vs. Limiting Void Width

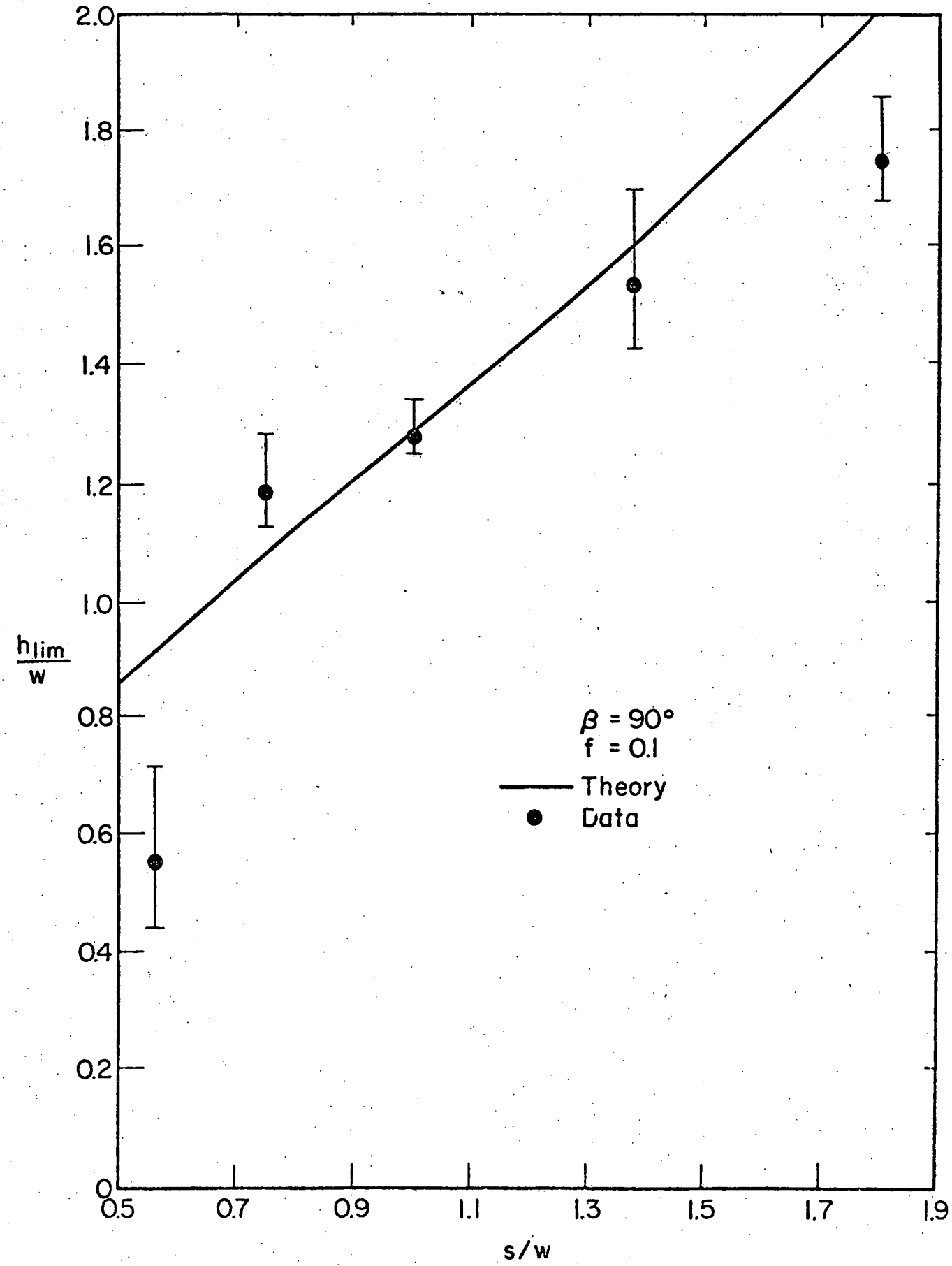

Figure 9. Limiting Void Width vs. s/w, Theory and Experiment

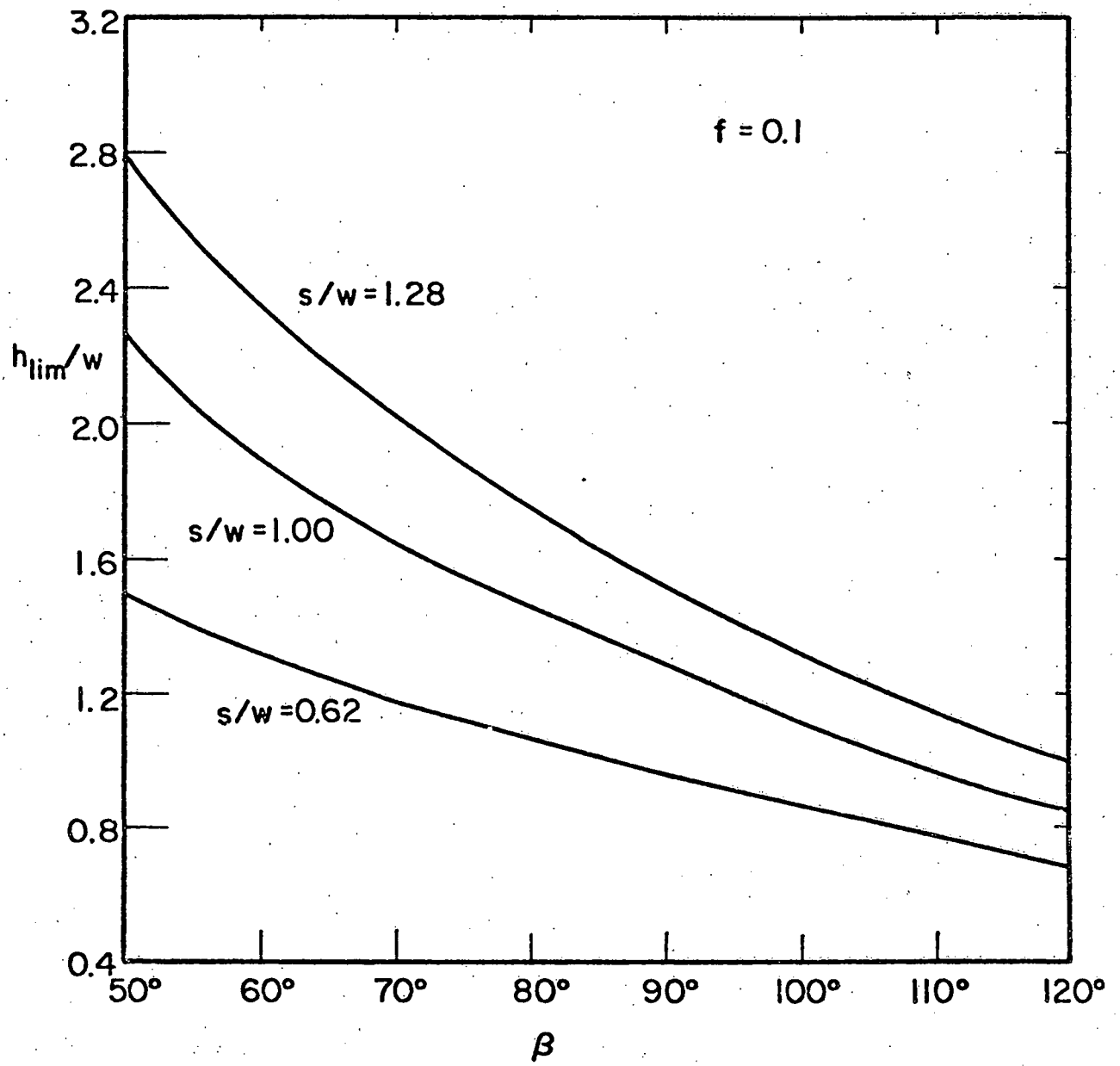

Figure 10. Deflecting Plate Angle vs. Limiting Void Width

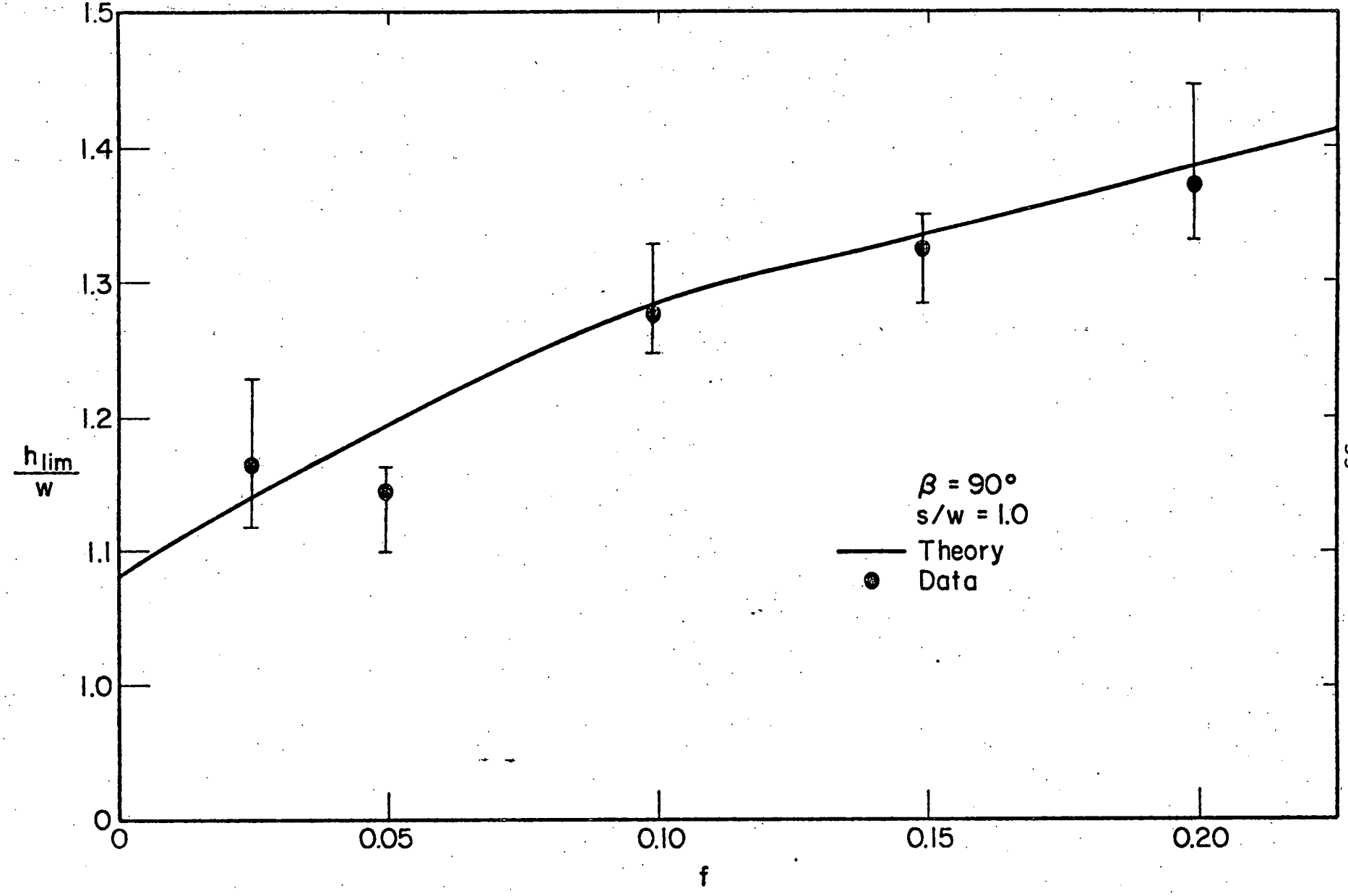

Figure 11. Fraction of Secondary Flow vs. Limiting Void Width

determination of the relative importance of these opposing parameters, which is beyond the scope of this text.

All of the composite curves (Figures 12-19) span a particular range of h/w, from 1.0 to 2.0. As Figures 12 and 13 demonstrate, a lower limit exists for the geometries of interest. If h/w were less than 1.0, any particles starting to the right of the upward projection of point E (refer to Figure 1) could never make it into the void. An efficiency curve (E_v) for such a device would asymptotically approach some limiting efficiency less than 1.0. As it is, a parallel throat impactor with h/w = 1 has an infinitely large loss spectrum. Figure 12 in particular indicates that A decreases more slowly for higher values of h/w. Figures 16 and 17 suggest that the choice of s/w may not be very critical, at least regarding L_m. As shown in Figures 18 and 19, the cutoff Stokes' parameter decreases with increasing h/w. Interestingly, the S curves of Figures 14 and 15 increase first rapidly, then more slowly, before diverging for large h/w. Since the aim is to minimize both S and A, choosing an intermediate h/w might be a good compromise for both curves.

Because these figures are only two-dimensional, and A, S, L_m, and $\psi_{50}^{\frac{1}{2}}$ each vary with β, f, s/w, and h/w, one must fix three parameters for each composite curve. Given β and f, contours of constant s/w span the desired range of h/w. For $\beta = 70°$, three jet-to-plate spacings are chosen to correspond with converging throat angles 38°, 45°, and 58.2° of the

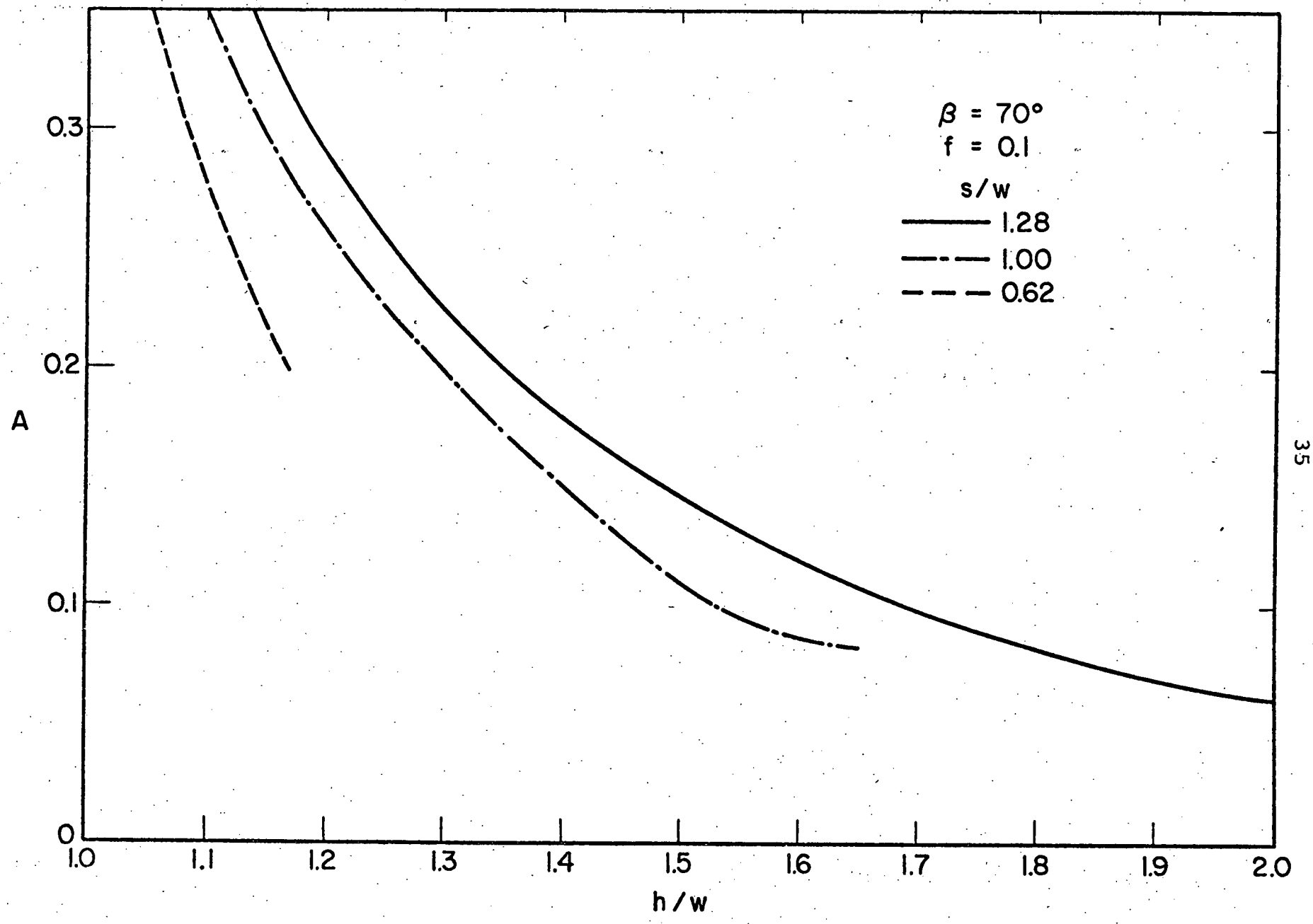

Figure 12. Normalized Areas under Loss Spectrum vs. Void Width

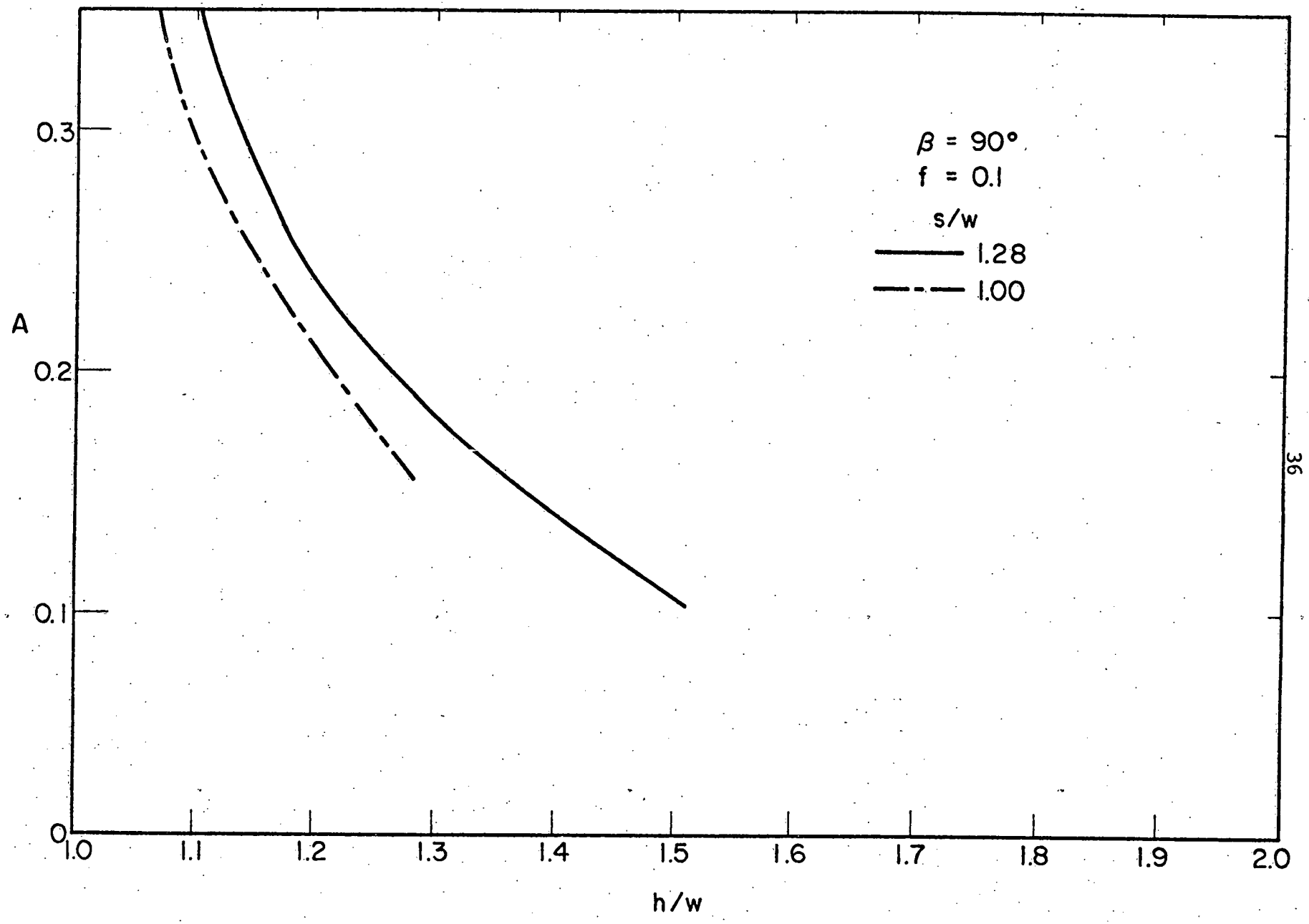

Figure 13. Normalized Areas under Loss Spectrum vs. Void Width

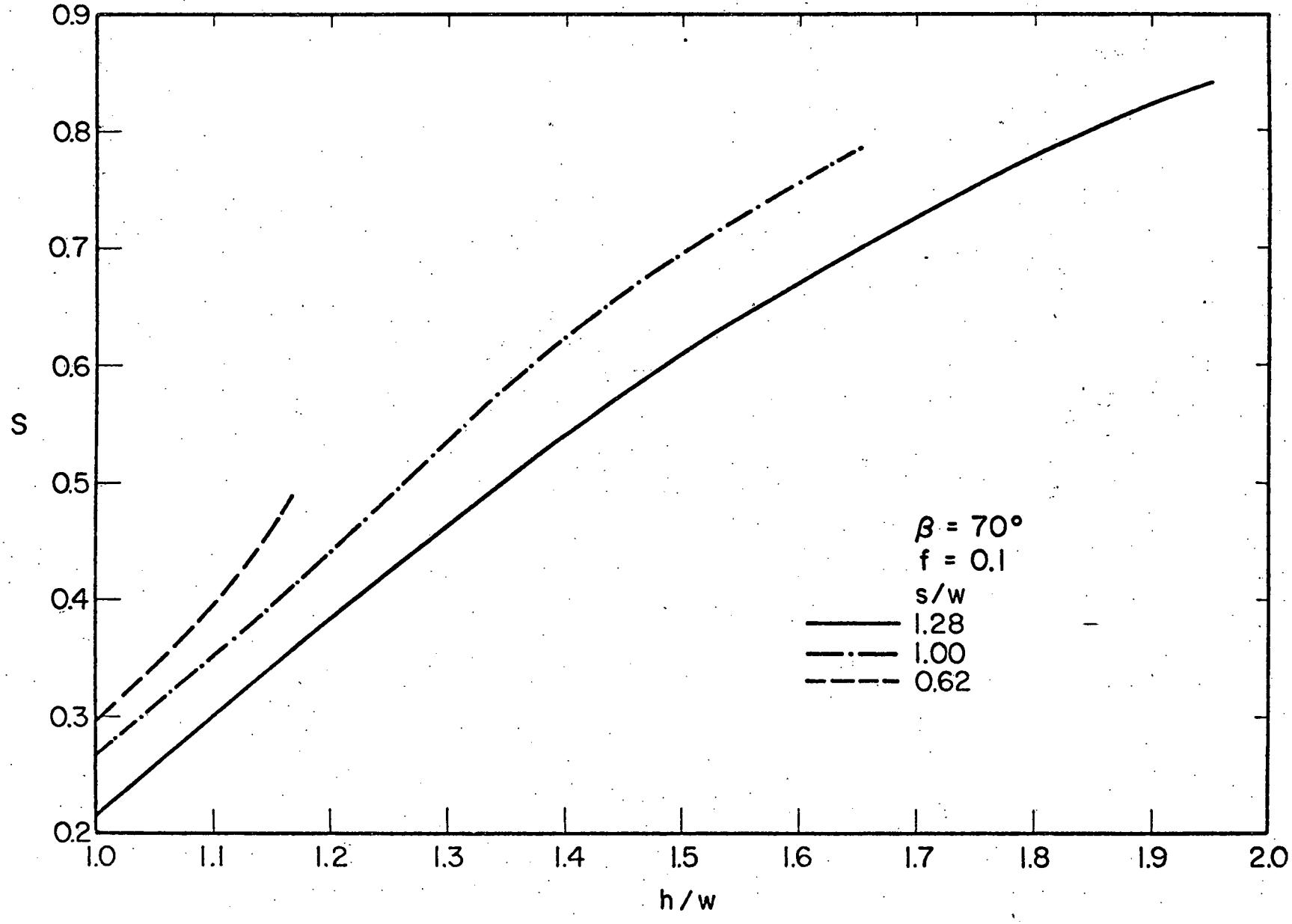

Figure 14. Relative Dispersions of $\psi^{\frac{1}{2}}$ vs. Void Width

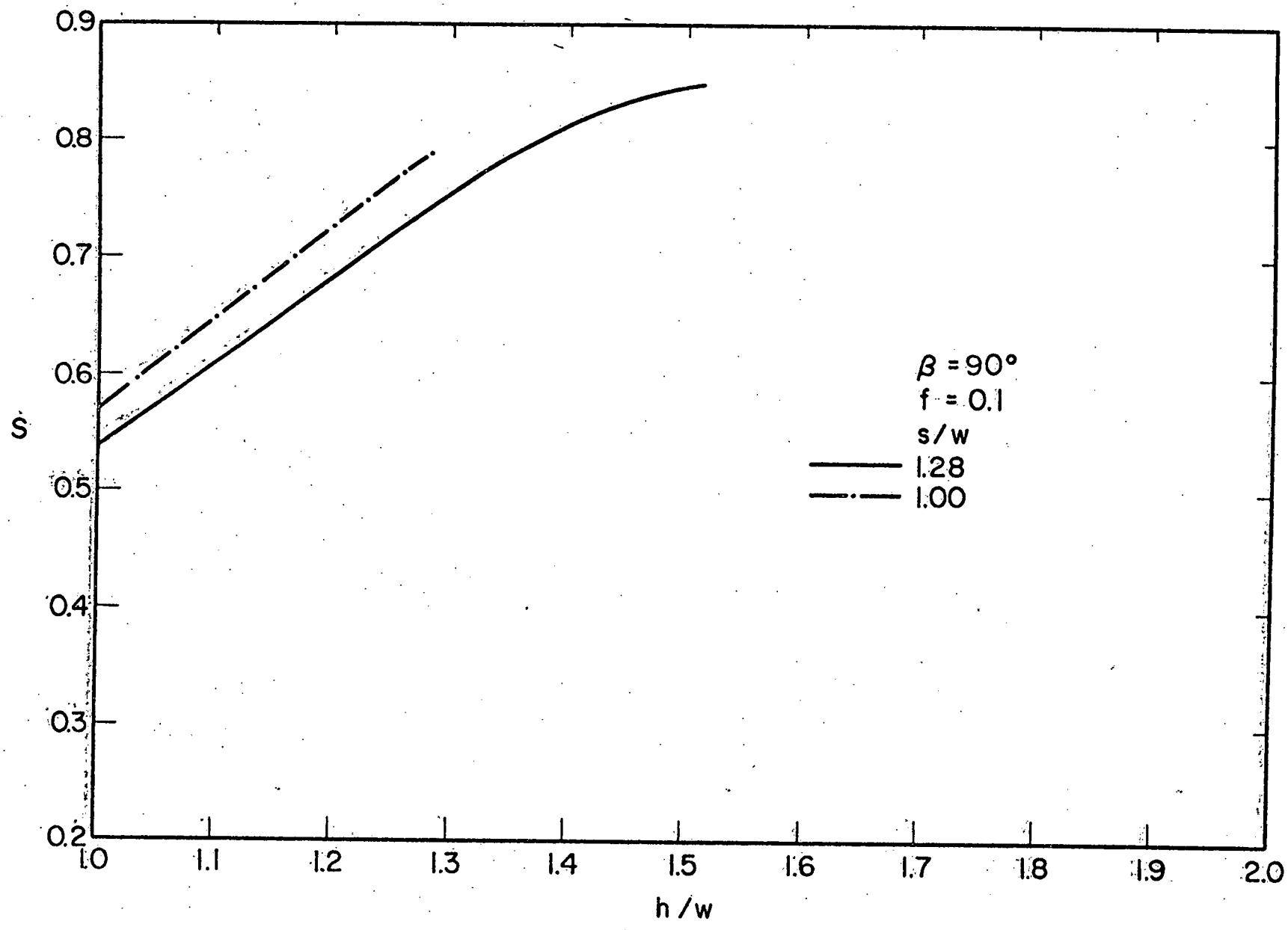

Figure 15. Relative Dispersions of $\psi^{1/2}$ vs. Void Width

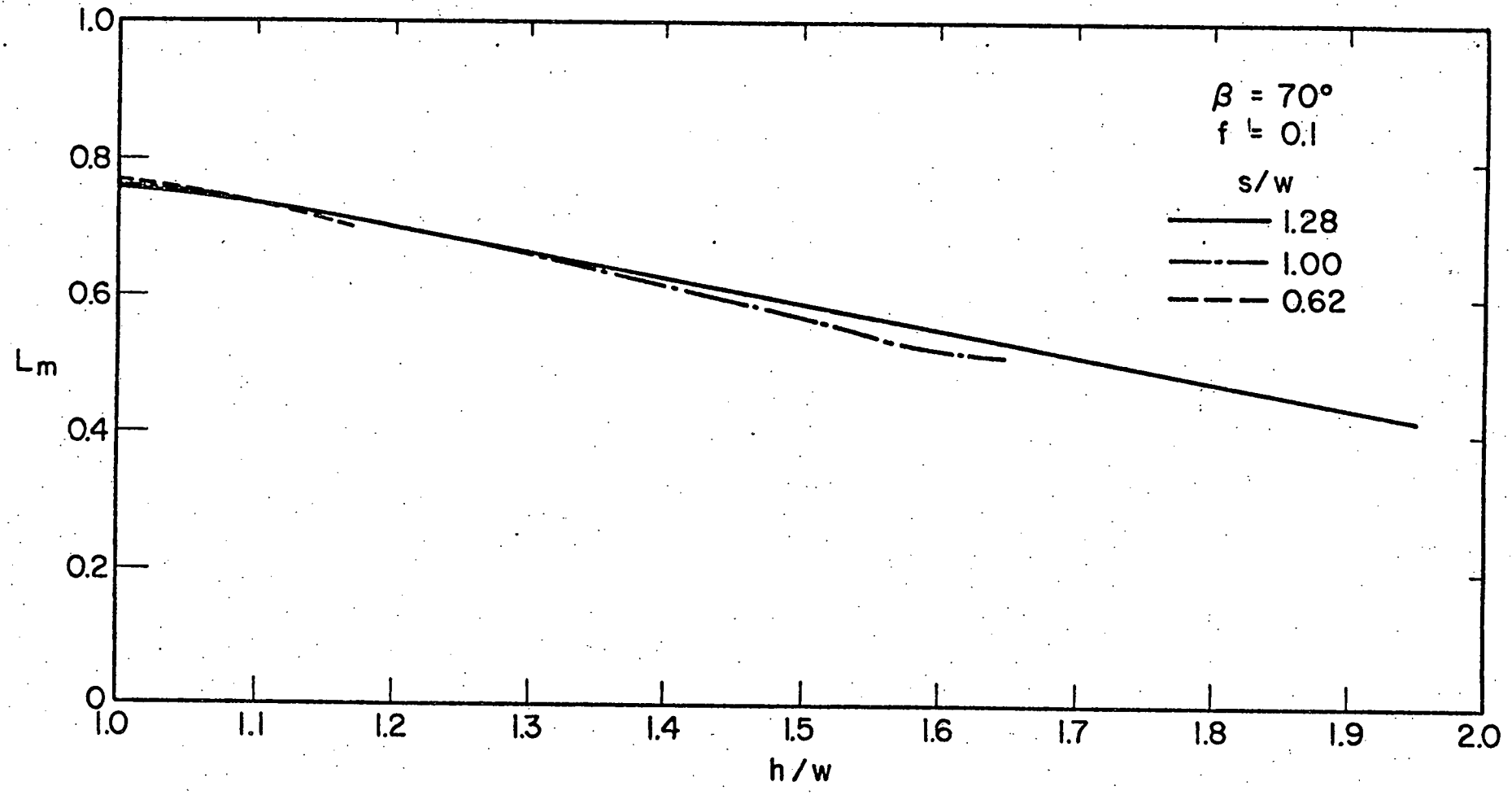

Figure 16. Loss Spectrum Maxima vs. Void Width

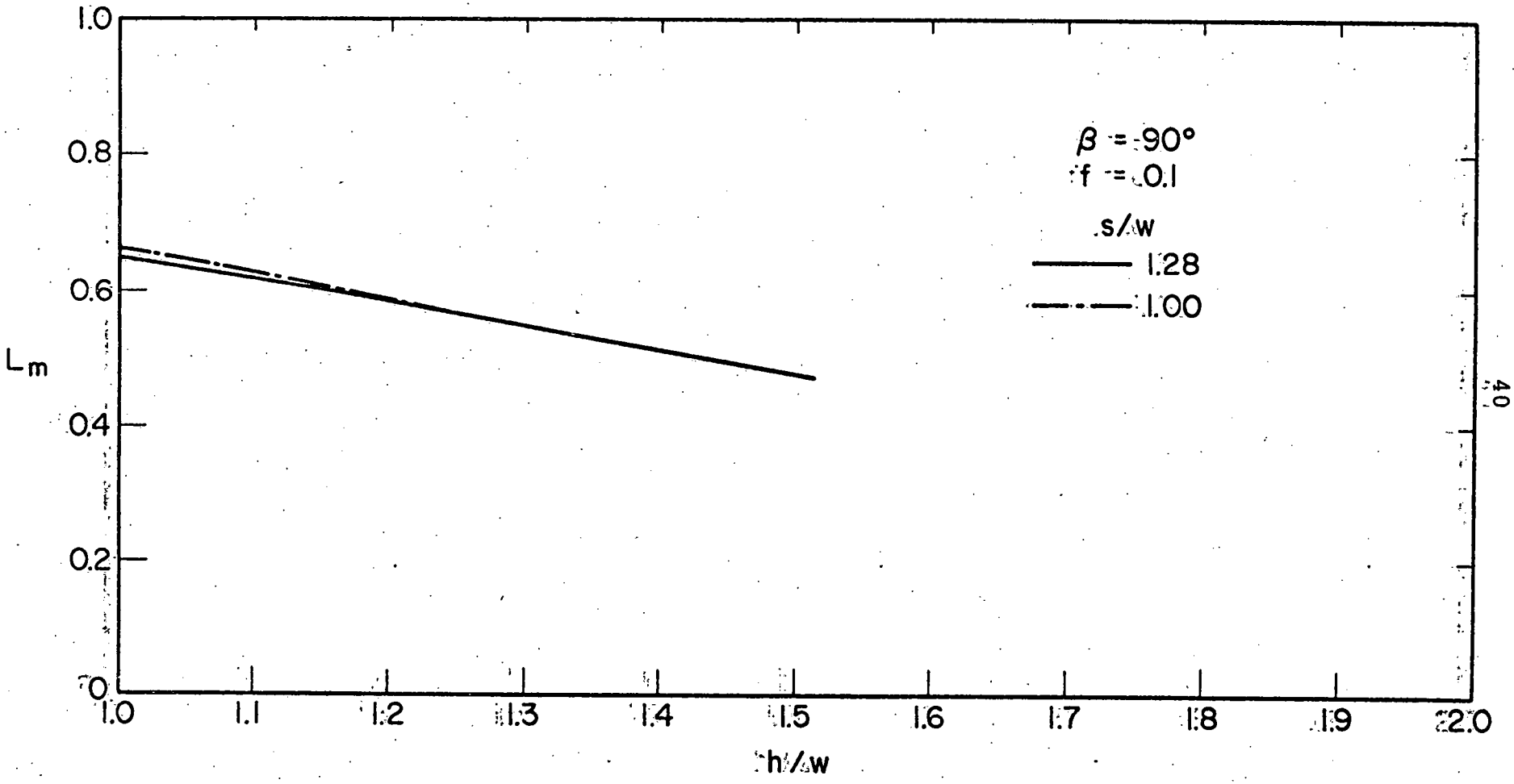

Figure 17. Loss Spectrum Maxima vs. Void Width

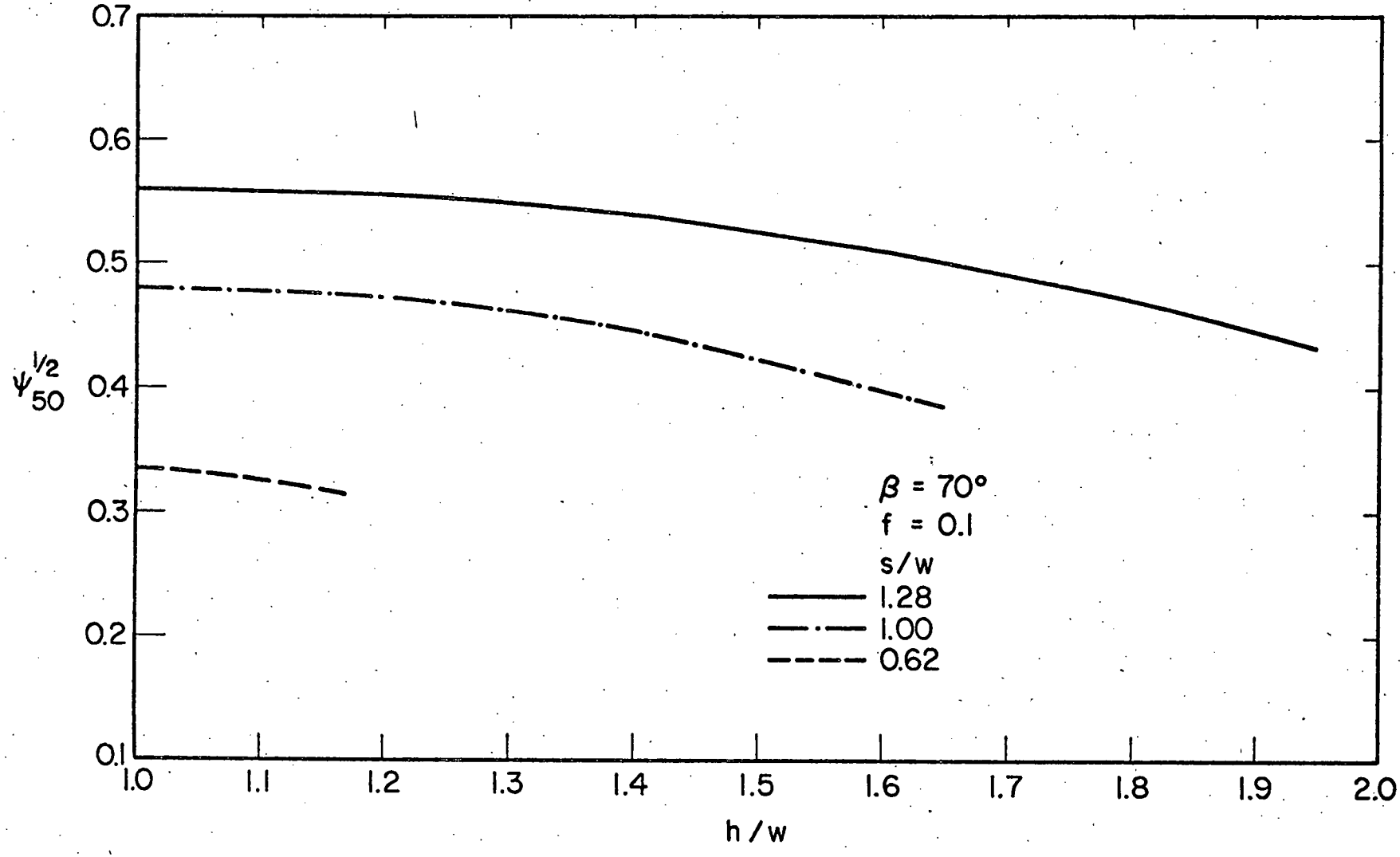

Figure 18. Cutoff Stokes' Parameters vs. Void Width

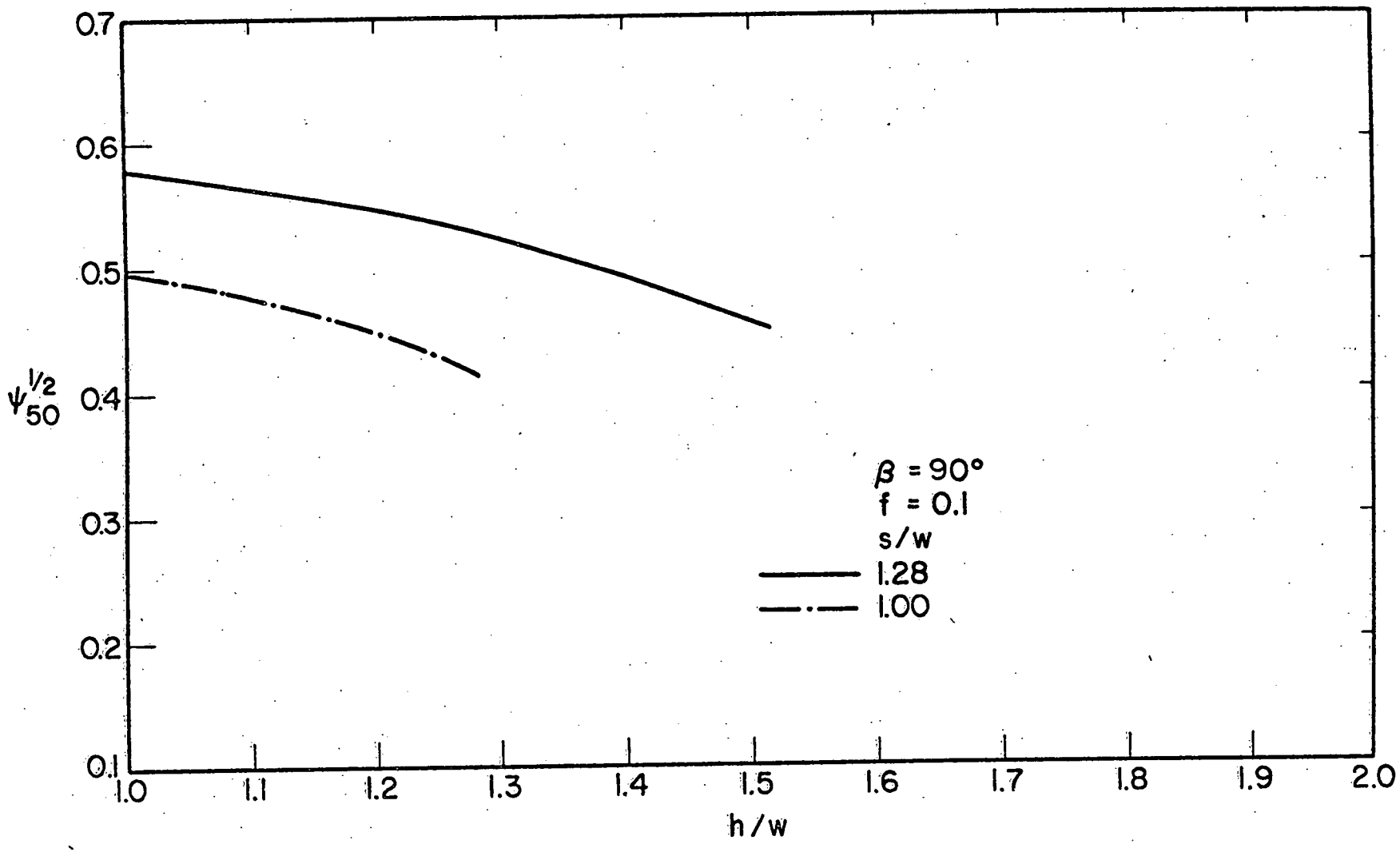

Figure 19. Cutoff Stokes' Parameters vs. Void Width

self-similar virtual impactor of an earlier work [3]. For the converging throat,

$$s/w = \frac{1}{\tan \beta_o} \quad , \tag{4.1}$$

where β_o is the throat angle. When $\beta = 90°$, the limiting void width for $s/w = 0.62$ is only 0.957, below the h/w range of interest. Ten percent bleed flow ($f = 0.1$) and a 90° deflecting plate angle represent a typical virtual impactor arrangement. Variation of the plate angle (e.g., to $\beta = 70°$) allows one to compare different device geometries.

One may evaluate changing the plate angle by comparing each pair of composite curves. While $\beta = 90°$ has consistently smaller areas than $\beta = 70°$, S is always smaller for the smaller plate angle. Also, L_m for $\beta = 70°$ lies just above its corresponding value when $\beta = 90°$. The $\psi_{50}^{\frac{1}{2}}$ curves are too close to ascertain any meaningful trend. Resolution of the conflicting tendencies of smaller A but greater S for $\beta = 90°$ might lead to determination of an optimum plate angle. While Figure 8 shows that h_{lim}/w is a stronger function of s/w for $\beta = 70°$ than for $\beta = 90°$, it is not clear that this is a desirable property. Further investigation of the intended applications for the device may lead to a more rational set of design criteria.

5. CONCLUDING REMARKS

Conformal mapping techniques have produced a potential flow solution to the problem of an ideal fluid impinging on a void. The fluid deflecting plate angle, jet-to-plate spacing, void width, and fraction of secondary flow are varied numerically, allowing rapid exploration of a range of interesting device geometries. Salient features of particle efficiency curves suggest design criteria. In particular, particle losses to the collecting plate should be minimized for ease of operation. Additionally, particle sizing capabilities are enhanced with a sharp device cutoff character. These considerations conflict for void widths of interest. Operating a device at or near its theoretically limiting void width would minimize particle losses, but hinder size-classifying. Optimization of impactor design requires clarification of the relative importance of these contradictory tendencies. The aim of this text was simply to develop a solution scheme for tracing the movement of particles in an ideal fluid, under the influence of Stokes' Law.

REFERENCES

1. C.N. Davies and M. Aylward, Proceedings of the Physical Society (London), B64, 889 (1951).

2. L.J. Forney and D.G. Ravenhall, "Development of an Aerosol Size Classifier", Department of Energy Progress Report C00-4319-1, January 1978.

3. L.J. Forney and D.G. Ravenhall, "Development of an Aerosol Size Classifier: A Two-Dimensional Self-Similar Virtual Impactor", Department of Energy Progress Report COO-4319-4, January 1979.

4. L.J. Forney, D.G. Ravenhall, and D.S. Winn, "Aerosol Impactors: A Study of a Fluid Jet Impinging upon a Void", Journal of Applied Physics, 49, 2339 (1978).

5. L. Prandtl and O.G. Tietjens, Fundamentals of Hydro- and Aeromechanics. New York: Dover Publications, Inc., 1934.

6. D.G. Ravenhall and L.J. Forney, "Aerosol Impactors: Calculation of Optimal Geometries", Journal of Physics E: Scientific Instruments, accepted for publication (1980).

7. D.G. Ravenhall, L.J. Forney, and M. Jazayeri, "Aerosol Sizing with a Slotted Virtual Impactor", Journal of Colloid and Interface Science, 64, 108 (1978).